

**MODELING AND MEASUREMENT OF ELECTROMAGNETIC
RADIATED EMISSION FROM HIGH SPEED INTERCONNECTS
IN DIGITAL CIRCUITS**

JI YUANCHENG

(B.Eng.(Hons.), NUS)

A THESIS SUBMITTED

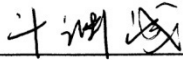
**FOR THE DEGREE OF DOCTOR OF PHILOSOPHY
DEPARTMENT OF ELECTRICAL AND COMPUTER ENGINEERING
NATIONAL UNIVERSITY OF SINGAPORE**

2014

DECLARATION

I hereby declare that the thesis is my original work and it has been written by me in its entirety. I have duly acknowledged all the sources of information which have been used in the thesis.

This thesis has also not been submitted for any degree in any university previously.



Ji Yuancheng

14 August 2014

ACKNOWLEDGEMENTS

Foremost, I would like to express my deepest gratitude to my supervisor, Associate Professor Koenraad Mouthaan for his full support of my research and study. Without his patience and motivation, I could not accomplish my work. He provided me the opportunity to start my research path. His precise and serious-minded working attitude not only influences my research methodology but also my living attitude. As a responsible supervisor, he never begrudged spending time and energy on my research discussion, for which he even sacrificed his lunch time and weekends. I am also thankful to him for seriously reading and commenting on great numbers of reviews of my papers including this thesis.

I am truly grateful to my co-supervisor, Dr. Neelakantam V. Venkatarayalu, for the long discussions every two weeks. He gave me lots of valuable advice in technical details and helped me to gain focus in my ideas. He also spent a lot of time to help me revise my papers.

Thanks to several colleagues from the lab for their generous assistance with my research-related problems, namely Tang Xinyi, Ray Fang Hongzhao and Hu Zijie. I will also remember my other friends in the lab, for their encouragement and assistance over these years.

I sincerely appreciate my lab officers, Mdm. Lee Siew Choo, Mdm. Guo Lin, and Mr. Sing Cheng, for their help in the fabrication and the measurement of printed circuit boards and other lab work.

I would like to devote my warmest thanks to my husband, who always

consoled me when I suffered disappointments in my research process throughout my PhD time.

At last, I want to thank my parents, who brought me into the world and always love me no matter where and when.

TABLE OF CONTENTS

Chapter 1 Introduction.....	1
1.1 Background	1
1.2 EMC overview	2
1.2.1 History of EMC.....	2
1.2.2 EMC standards.....	3
1.3 The modeling methods for electromagnetic radiated emission from interconnects	6
1.3.1 Full wave numerical methods	6
1.3.2 Analytical methods	15
1.3.3 Near-field-far-field (NF-FF) transformation methods	19
1.3.4 Conclusions.....	19
1.4 Motivation, Scope and Thesis Organization	20
1.5 List of Publications.....	24
Chapter 2 Modeling of the radiated emission from a single transmission line	25
2.1 Introduction	25
2.2 The radiation characteristics of a single straight transmission line	25
2.2.1 The impact of transmission line parameters on radiation ..	25
2.2.2 The impact of single straight transmission line discontinuity on radiation	29
2.3 The modeling method for the radiated emission	31
2.3.1 The radiated emission for the Hertzian dipole.....	31

2.3.2 The modeling method for the radiated emission from a single transmission line.....	34
2.4 The application of the modeling method for various transmission lines	40
2.4.1 The application of the modeling method for the transmission lines under different loading conditions	40
2.4.2 The application of the modeling method for the transmission lines with different materials	52
2.4.3 The application of the modeling method for the transmission lines with different geometries	65
2.5 Conclusions and recommendations	71

Chapter 3 Modeling electromagnetic radiated emission from high speed interconnects in digital circuits..... 73

3.1 Introduction	73
3.2 Principle knowledge of IBIS models.....	73
3.2.1 The background of IBIS models	73
3.2.2 The description of IBIS models	77
3.2.3 The simulation tools of IBIS models	80
3.3 The limitation of IBIS models.....	80
3.3.1 The natural discrepancies of IBIS models	80
3.3.2 Limitations of the IBIS model in SSN simulation.....	82
3.3.3 Explanation for the IBIS model limitations in SSN simulation.....	85
3.3.4 Improvement method for IBIS models in SSN simulation	89

3.4 The radiated emission from interconnects with a non-linear dynamic load	93
3.4.1 The radiated emission model	93
3.4.2 The radiated emission from the interconnects loaded with a digital receiver	94
3.5 The influence of various SI improvement techniques on the radiated emission	98
3.5.1 Motivation.....	98
3.5.2 SI improvement techniques.....	99
3.5.3 Radiated emission of SI improvement techniques.....	102
3.6 Conclusions and recommendations	107

Chapter 4 Measurement of radiated emission measurement from high speed interconnects 109

4.1 Introduction	109
4.1.1 The test site for radiated emission measurement	109
4.1.2 The antenna for radiated emission measurement.....	109
4.2 The setup for the radiated emission measurement	110
4.3 Measurement of radiated emission from interconnects in simple RF circuits	113
4.4 Measurement of radiated emission from interconnects in digital circuits	118
4.4.1 Measurement of radiated emission from interconnects placed between a digital signal and a fixed load.....	118
4.4.2 Measurement of radiated emission from the interconnects between digital devices	125

4.5 Conclusions and recommendations	148
Chapter 5 Conclusions and recommendations.....	149
5.1 Modeling the electromagnetic radiated emission from high speed interconnects in digital circuits with IBIS models	150
5.2 The impact of different passive SI improvement techniques on the electromagnetic radiated emission from high speed interconnects in digital circuits	153
Bibliography	155

SUMMARY

With the increasing speed and density of digital integrated circuits (ICs), it has been found that digital devices generate electromagnetic fields that unintentionally can interfere with the normal operation of other devices or their own operations. Therefore, some electromagnetic compatibility (EMC) standards are developed to regulate the electromagnetic emission of digital devices. For achieving good device performance and satisfying these EMC standards, the modeling of electromagnetic radiated emission from interconnects is necessary in the design cycle of digital circuits. This thesis focuses on the modeling and measurement of electromagnetic radiated emission from interconnects in digital circuits. Since the radiated emission is investigated in far field, only the unintended emission interfered with the normal operation of other devices is addressed.

The modeling of the electromagnetic radiated emission starts with the investigation of the radiation characteristics of a single transmission line under different loading conditions and with different geometry parameters. After that, an analytical modeling method for the radiated emission of interconnects is explained in detail. This method is based on a closed-form dyadic Green's function with the use of a circuit simulator. For the interconnects specified in digital circuits, Input/Output Buffer Information Specification (IBIS) models are applied in conjunction with the analytical method to model the dynamic property of digital devices.

This method is further adopted to investigate the impact of passive signal integrity (SI) improvement techniques on the radiated emission from different

interconnects between digital devices. The radiated emission modeling results can help designers to select the appropriate SI improvement technique taking into account EMC requirements. This application is very meaningful for design engineers as the radiated emission can be rapidly estimated with the SI analysis results, i.e., the EMC analysis and SI analysis can be integrated effectively in the design stage. Lastly, the measurement for the radiated emissions from the interconnects under different conditions is performed. Good agreement is observed by comparing the measurement results with the modeling results.

LIST OF TABLES

Table 1.1: Radiated emission limits for Class A digital device in the FCC standards [4].....	4
Table 1.2: Radiated emission limits for Class B digital device in the FCC standards [4].....	5
Table 1.3: Radiated emission limits for Class A ITE equipment at a distance of 10 m in CISPR 22 [4].....	6
Table 1.4: Radiated emission limits for Class B ITE equipment at a distance of 10 m in CISPR 22 [4].....	6
Table 1.5: Main features of the most common numerical techniques [25]	9
Table 2.1: The transmission line geometry parameters	27
Table 2.2: The transmission line geometry parameters when $H = 62$ mil	52
Table 2.3: The transmission line geometry parameters when $\epsilon_r = 2.2$	58
Table 2.4: The differences between the modeling results and the HFSS simulation results for the three different geometries	70
Table 4.1: The antenna factor and cable loss.....	112
Table 5.1: Proposed interconnects for further studies.	152

LIST OF FIGURES

Fig. 1.1: FDTD cell with electromagnetic field components [26].	10
Fig. 1.2: The type of finite elements used in discretization: (a) One-dimensional, (b) two-dimensional, and (c) three-dimensional [27].	12
Fig. 1.3: Quasi-static PEEC model for simple conductor geometry.	15
Fig. 2.1: The circuit structure for the evaluation of radiation from a single straight transmission line.	26
Fig. 2.2: The radiated power for the single straight transmission lines with different ϵ_r and f when $h = 0.635$ mm.	28
Fig. 2.3: The circuit structure for the evaluation of radiation from a single straight transmission line.	29
Fig. 2.4: The radiated power for a single straight transmission line under different loading conditions.	30
Fig. 2.5: A Hertzian dipole in free space.	32
Fig. 2.6: A Hertzian dipole above infinite ground plane.	33
Fig. 2.7: Geometry and equivalent two-port network of the straight transmission line.	37
Fig. 2.8: Geometry and equivalent two-port network of the L-shaped transmission line.	38
Fig. 2.9: The circuit connection of the straight line.	41
Fig. 2.10: The 3D radiation pattern for the straight microstrip line with 50Ω (matched) load.	42
Fig. 2.11: The observation point for 3D radiation pattern plot.	43
Fig. 2.12: The 3D radiation pattern comparison for the straight microstrip line with matched load condition.	44

Fig. 2.13: The 3D radiation pattern comparison for the straight microstrip line with different load conditions.	47
Fig. 2.14: The radiated emissions from the straight microstrip line with different loading conditions.	50
Fig. 2.15: The radiated emission comparison for the straight microstrip line with different loading conditions.	51
Fig. 2.16: The 3D radiation pattern comparison for the transmission lines with different substrate permittivity.	54
Fig. 2.17: The radiated emissions from the straight microstrip line with different substrate permittivity.	56
Fig. 2.18: The radiated emission comparison for the straight microstrip line with different substrate permittivity.	57
Fig. 2.19: The 3D radiation pattern comparison for the transmission lines with different substrate thicknesses.	61
Fig. 2.20: The radiated emissions from the straight microstrip line with different substrate thicknesses.	63
Fig. 2.21: The radiated emission comparisons for the straight microstrip line with different substrate thicknesses.	65
Fig. 2.22: The geometry of the L-shaped microstrip line.	66
Fig. 2.23: The 3D radiation pattern comparison for the L-shaped microstrip line with matched loading condition.	67
Fig. 2.24: The radiated emissions from the L-shaped microstrip line with matched load condition.	67
Fig. 2.25: The geometry of the L-shaped microstrip line.	68

Fig. 2.26: The 3D radiation pattern comparison for the L-shaped microstrip line with matched loading condition.....	69
Fig. 2.27: The radiated emissions from the U-shaped microstrip line with matched load condition.....	70
Fig. 3.1: The work flow of the S2IBIS software [72].....	76
Fig. 3.2: The basic elements in an IBIS model [72].	78
Fig. 3.3: The buffer with four cascaded inverting drivers.	82
Fig. 3.4: The circuit for SSN simulation with four parallel buffers.....	83
Fig. 3.5: The quiet line buffer output response V_{out1} using the SPICE model (solid line) and the IBIS model (dotted line).	84
Fig. 3.6: The SSN response at V_{cc} using the SPICE model (solid line) and the IBIS model (dotted line).	85
Fig. 3.7: The current at the power rail I_{cc} using the SPICE model (solid line) and the IBIS model (dotted line).....	86
Fig. 3.8: The power rail current switching rate dI/dt using the SPICE model (solid line) and the IBIS model (dotted line).	87
Fig. 3.9: The circuit diagram of the CMOS output driver.	87
Fig. 3.10: The diagram of the improved IBIS model circuits.....	91
Fig. 3.11: The V_{cc} difference between the SPICE model and the original IBIS model (dotted line) and the V_{cc} difference between the SPICE model and the improved IBIS model (solid line).	92
Fig. 3.12: The V_{out1} difference between the SPICE model and the original IBIS model (dotted line) and the V_{out1} difference between the SPICE model and the improved IBIS model (solid line).....	92
Fig. 3.13: The circuit diagram for dynamic load condition.	94

Fig. 3.14: The circuit diagram for dynamic load condition.	94
Fig. 3.15: The frequency-dependent load profile.....	95
Fig. 3.16: The radiated emission from the straight interconnect under dynamic loading condition.	96
Fig. 3.17: The radiated emission from the L-shaped interconnect under dynamic loading condition.....	97
Fig. 3.18: The schematic diagram for the original circuit and the four SI improvement techniques considered (a) no SI improvement technique; (b) series termination technique; (c) parallel termination technique; (d) Thévenin termination technique; (e) AC termination technique.	100
Fig. 3.19: The maximum radiated emission from the straight interconnect ..	103
Fig. 3.21: Frequency domain current for the straight interconnect.....	105
Fig. 3.22: The maximum radiated emission from the L-shaped interconnect	106
Fig. 4.1: The measurement setup in the chamber.	111
Fig. 4.2: The instrument connection for the measurement	112
Fig. 4.3: The radiated emission from the straight interconnect made on FR4.	114
Fig. 4.4: The radiated emission from the straight interconnect made on RT5880.	115
Fig. 4.5: The radiated emission from the L-shaped interconnect made on FR4.	116
Fig. 4.6: The radiated emission from the L-shaped interconnect made on RT5880.	117
Fig. 4.7: The circuit diagram for the interconnects placed between a digital pulse input and fixed load.	119

Fig. 4.8: Photo of the fabricated DUT.	120
Fig. 4.9: The radiated emission from the straight interconnect on FR4.	121
Fig. 4.10: The radiated emission from the straight interconnect on RT5880.	122
Fig. 4.11: The radiated emission for the L-shaped interconnect on FR4.....	123
Fig. 4.12: The radiated emission from the L-shaped interconnect on RT5880.	124
Fig. 4.13: The circuit diagram for the interconnects placed between two digital devices.....	125
Fig. 4.14: Photo of the fabricated DUT.	126
Fig. 4.15: The radiated emission from the straight interconnect on FR4 placed between two digital devices without any SI improvement techniques..	127
Fig. 4.16: The radiated emission from the straight interconnect on FR4 placed between two digital devices with series termination technique.....	128
Fig. 4.17: The radiated emission from the straight interconnect on FR4 placed between two digital devices with parallel termination technique.....	129
Fig. 4.18: The radiated emission from the straight interconnect on FR4 placed between two digital devices with Thévenin termination technique.....	130
Fig. 4.19: The radiated emission from the straight interconnect on FR4 placed between two digital devices with AC termination technique.	131
Fig. 4.20: The radiated emission from the straight interconnect on RT5880 placed between two digital devices without any SI improvement techniques.	133
Fig. 4.21: The radiated emission from the straight interconnect on RT5880 placed between two digital devices with series termination technique.	134

Fig. 4.22: The radiated emission comparison from the straight interconnect on RT5880 placed between two digital devices with parallel termination technique.	135
Fig. 4.23: The radiated emission from the straight interconnect on RT5880 placed between two digital devices with Thévenin termination technique.	136
Fig. 4.24: The radiated emission from the straight interconnect on RT5880 placed between two digital devices with AC termination technique.	137
Fig. 4.25: The radiated emission from the L-shaped interconnect on FR4 placed between two digital devices without any SI improvement techniques.	139
Fig. 4.26: The radiated emission from the L-shaped interconnect on FR4 placed between two digital devices with series termination technique.	140
Fig. 4.27: The radiated emission from the L-shaped interconnect on FR4 placed between two digital devices with parallel termination technique.	142
Fig. 4.28: The radiated emission from the L-shaped interconnect on FR4 placed between two digital devices with Thévenin termination technique.	144
Fig. 4.29: The radiated emission from the L-shaped interconnect on FR4 placed between two digital devices with AC termination technique.	146
Fig 5.1: The schematic diagram for the circuit with Schottky-diode termination technique.....	154

LIST OF SYMBOLS

f	frequency in Hz
ω	frequency in rad/s
μ_0	vacuum permeability
ϵ_0	vacuum permittivity
ϵ_r	relative permittivity of the material
$\bar{E}_\theta, \bar{E}_\phi$	the electric field component in spherical- θ field, in spherical- ϕ field
$\bar{E}_\theta^d, \bar{E}_\phi^d$	the direct component of the electric field in spherical- θ field, in spherical- ϕ field
$\bar{E}_\theta^r, \bar{E}_\phi^r$	the reflected component of the electric field in spherical- θ field, in spherical- ϕ field
$\bar{A}_\theta, \bar{A}_\phi$	the vector potential in spherical- θ field, in spherical- ϕ field

LIST OF ABBREVIATIONS

AC	alternating current
ADS	Advanced Design System (software from Agilent)
AF	antenna factor
BJT	bipolar junction transistor
CISPR	International Special Committee on Radio Interference
DUT	device under test
EDA	electronic design
EEA	European Economic Area
EMC	electromagnetic compatibility
EMI	electromagnetic interference
FCC	Federal Communications Commission
FDTD	finite difference time domain
FEM	finite element methods
IBIS	Input /Output Buffer Information Specification
IC	integrated circuit
ICEM	Integrated Circuit Electromagnetic Model
IEC	International Electrotechnical Committee
ITE	Information Technology Equipment
HFSS	High Frequency Structural Simulator (software from ANSYS)
MoM	method of moments
PCB	printed circuit board
PDE	partial differential equation
PEEC	partial element equivalent circuit
RF	radio frequency

SI	signal integrity
SRM	source reconstruction method
SSN	simultaneous switching noise
TWM	travelling wave method
TEM	transverse electromagnetic

Chapter 1

Introduction

1.1 Background

In the past years the emphasis in the design of digital electronics has been to increase the operational speed of circuits, resulting in logic devices becoming faster. Transmission lines are implemented to interconnect high speed circuits. In order to reduce signal reflections and waveform distortion, the interconnects with controlled impedance are required. However, the increases of speed and driver levels lead to the increase of electromagnetic radiated emission from these interconnects. The electromagnetic interference (EMI) from the digital circuits not only influences the functionalities of other circuits but also the radiated circuits themselves. As a result, the Federal Communications Commission (FCC) [1], International Special Committee on Radio Interference (CISPR) [2] and other similar agencies build regulations limiting the levels of electromagnetic radiated emissions for digital devices sold in the respective areas.

The introduction of these regulations requires the design engineers to be concerned not only with device functionality, reliability and product cost, but also with the electromagnetic compatibility (EMC) requirements. However, in order to capture a commercial market, short design cycles are needed. This leads to the elimination of various sub-system tests and re-design stages. Hence, a weak EMC design may not be discovered until final compliance testing begins. At that time the improvement methods are limited unless re-

design takes place. Unfortunately this may seriously affect the product's success in a fast-paced market.

1.2 EMC overview

1.2.1 History of EMC

Electromagnetic compatibility has the definition as [3]: "the ability of an equipment or system to function satisfactorily in its electromagnetic environment without introducing intolerable electromagnetic disturbances to anything in that environment."

The concern of electromagnetic interference problem started from late 1800s with the first spark-gap experiment of Marconi [4]. However, it is around 1920 that a number of electrical and electronic journals published papers on radio interference. In 1930, the radio interference from public electronic equipment appeared to be a major problem.

In World War II, radar, electronic devices, navigation devices and primarily radios are widely used. EMI between different devices began to increase. Since at that time, the applications of the electronics were not as much as they are today, the EMI problems could still be solved easily. However, with the inventions of the bipolar junction transistor (BJT), the integrated circuit (IC) and the microprocessor in 1950s-1970s, EMI became significant because of the higher density and faster transmission speeds.

Towards the end of 1970s, the transition from analog signal process to digital signal processing is speeded up. People tend to implement all the electronic functions digitally for the benefits of high speed and high density of

ICs. As a result, the noise sources are widely spread and significantly all over the world, which makes the EMI problems become serious and cannot be solved easily.

1.2.2 EMC standards

The FCC [1] and CISPR standards [2] are the most widely adopted regulations for commercial digital products around the world. The FCC regulations focuses on the electromagnetic emissions of digital devices sold for the market in the United States [1], while the CISPR standard regulates the electromagnetic emissions of digital devices sold in other countries of the world except the United States.

FCC classifies the digital device products into Class A and Class B [5]. The digital devices applied in a business, industrial or commercial environment are belong to Class A, while the digital devices applied in a residential environment are belong to Class B. The limitation standards for devices in Class A and Class B are different. Generally speaking, the Class B limits are stricter than the Class A limits. There are mainly two reasons. The first reason is that in residential environment, the interference devices are closer to the susceptible devices, so the interference is more significant and hard to be reduced. The second reason is that the owners and users of Class B devices do not have the ability to protect their devices from electromagnetic interference.

The electromagnetic emissions are subdivided into conducted emissions and radiated emissions. By definition [4], “conducted emissions are those currents that are passed out through the unit’s alternating current (AC)

power cord and placed on the common power net, where they may radiate more efficiently because of the much larger expanse of this ‘antenna’ and thus cause interference with other devices”. In contrast, radiated emissions are the electric field, magnetic field and electromagnetic field radiated by circuit conducts, which can inference the operations of other devices. The FCC standards define the range for conducted emissions from 150 kHz to 30 MHz, while for radiated emissions, it typically covers from 30 MHz to 1 GHz, with extensions to 5-40 GHz. The FCC, the CISPR and other regulatory agencies all require the radiated electric field to be measured in dB μ V/m, as in terms of field strength. The value can be converted from $20\log_{10}(E \times 10^6)$, in which E in V/m. Table 1.1 [4] lists radiated emission limits for Class A digital devices in the FCC standards, while Table 1.2 [4] lists the limits for Class B digital devices. It is noted that the measurement distances for the two classes are different.

Table 1.1: Radiated emission limits for Class A digital device in the FCC standards [4].

Frequency (MHz)	Measured at 10 m	
	(μ V/m)	(dB μ V/m)
30-88	90	39
88-216	150	43.5
216-960	210	46.4
>960	300	49.5
>1000	300 (AV); 3000 (PK)	49.5 (AV); 69.5(PK)

Table 1.2: Radiated emission limits for Class B digital device in the FCC standards [4].

Frequency (MHz)	Measured at 3 m	
	($\mu\text{V/m}$)	($\text{dB}\mu\text{V/m}$)
30-88	100	40
88-216	150	43.5
216-960	200	46
>960	500	54
>1000	500 (AV); 5000 (PK)	54 (AV); 74(PK)

The other widely adopted regulations for digital devices are published by the CISPR, which is a committee of the International Electro technical Commission (IEC). Most countries outside US choose the CISPR regulations. Among a number of CISPR recommendations, CISPR 22 [2] is the most widely used. The electromagnetic emission limits of Information Technology Equipment (ITE) are set in CISPR 22, including conducted emissions and radiated emissions. In CISPR 22, the digital devices are also classified to Class A and Class B, which have the same definitions as in the FCC. By analogy with FCC, its conducted emission range also covers from 150 kHz to 30 MHz, while the radiated emission range covers from 30 MHz to 1 GHz. The European Economic Area (EEA) widely adopts CISPR22. All the countries of the European Union are the members of EEA. Table 1.3 [4] lists the radiated emission limits for Class A ITE equipment in CISPR 22, and Table 1.4 [4] lists the radiated emission limits for Class B ITE equipment in CISPR 22.

Table 1.3: Radiated emission limits for Class A ITE equipment at a distance of 10 m in CISPR 22 [4].

Frequency (MHz)	($\mu\text{V/m}$)	($\text{dB}\mu\text{V/m}$)
30-230	100	40
230-1000	224	47

Table 1.4: Radiated emission limits for Class B ITE equipment at a distance of 10 m in CISPR 22 [4].

Frequency (MHz)	($\mu\text{V/m}$)	($\text{dB}\mu\text{V/m}$)
30-230	31.6	30
230-1000	70.8	37

The electromagnetic emission limits in CISPR22 are always set at 10 m, no matter for Class A or Class B digital devices. However, in the FCC regulations, the limits for Class A digital devices are set at 10 m while the limits for Class B digital devices are set at 3 m. Hence, the comparison between the two regulations for Class A digital devices is quite straight forward, while the comparison for Class B digital devices is not. By applying the inverse distance rule, people scale the FCC limits for Class B digital devices at -10.45 dB for comparison with the CISPR22 limits.

1.3 The modeling methods for electromagnetic radiated emission from interconnects

1.3.1 Full wave numerical methods

From the electromagnetic radiated emission point of view, interconnects in digital circuits can be treated as antennas having unexpected electromagnetic emissions. Many approaches have been proposed to model the radiated

emissions from those interconnects. Conventionally, full wave numerical methods are a common approach [6]-[20]. The most popular full wave numerical techniques are:

- Finite difference time domain methods (FDTD) [21]
- Finite element methods (FEM) [22]
- The method of moments (MoM) [23]
- The partial element equivalent circuit (PEEC) method [24]

The full wave numerical techniques used for the evaluation can be classified according to which formulation of Maxwell's equations are solved numerically. (1.1)-(1.4) are Maxwell's equation in differential form and (1.5)-(1.8) are Maxwell's equation in integral form. (1.9)-(1.11) are three medium-dependent equations.

$$\nabla \times \mathbf{H} = \mathbf{J} + \frac{\partial \mathbf{D}}{\partial t} \quad (1.1)$$

$$\nabla \times \mathbf{E} = -\frac{\partial \mathbf{B}}{\partial t} \quad (1.2)$$

$$\nabla \cdot \mathbf{D} = \rho_v \quad (1.3)$$

$$\nabla \cdot \mathbf{B} = 0 \quad (1.4)$$

$$\oint_L \mathbf{H} \cdot d\mathbf{l} = \int_S (\mathbf{J} + \frac{\partial \mathbf{D}}{\partial t}) \cdot d\mathbf{S} \quad (1.5)$$

$$\oint_L \mathbf{E} \cdot d\mathbf{l} = -\int_S \frac{\partial \mathbf{B}}{\partial t} \cdot d\mathbf{S} \quad (1.6)$$

$$\oint_S \mathbf{D} \cdot d\mathbf{S} = \int_v \rho_v dv \quad (1.7)$$

$$\oint_S \mathbf{B} \cdot d\mathbf{S} = 0 \quad (1.8)$$

$$\mathbf{D} = \epsilon \mathbf{E} \quad (1.9)$$

$$\mathbf{B} = \mu \mathbf{H} \quad (1.10)$$

$$\mathbf{J} = \sigma \mathbf{E} \quad (1.11)$$

The main differences between the two kinds of full wave numerical techniques are [25]:

1. The variation of the discretization methodology. For the techniques based on the differential form of Maxwell's equation, the whole space, which includes the complete structure and the surrounding air, needs to be discretized. For the techniques based on the integral form of Maxwell's equation, the discretization region is the structure only, not including the air. Hence, for the previous one, more discretized cells are needed, which leads to more computation storage and time.
2. The variation of the solution variables. For the techniques based on the differential form of Maxwell's equation, the predominant solutions are \mathbf{E} and \mathbf{H} , which are field variables. In contrast, for the techniques based on the integral form of Maxwell's equation, the predominant solutions are current and voltage, which are circuit variables. It implies that the previous one can be used to solve electromagnetic field excited structures, antenna near field radiation patterns and scattering problems. The later one is applicable for PCB and EMI analysis. Anyway, the field variables and the circuit variables can be transformed to each other through post-processing.

Table 1.5: Main features of the most common numerical techniques [25]

Method	FDTD	FEM	MoM	PEEC
Formulation	Differential	Differential	Integral	Integral
Solution variables	Field	Field	Circuit	Circuit
Solution domain	TD or FD	TD or FD	TD or FD	TD and FD

These full wave numerical methods are widely adopted in commercial microwave software. Ansoft HFSS, the first commercial 3D EM simulation software in the world, adopts the FEM method. It can be used to simulate the S parameters and the EM fields for any arbitrary passive structures. Other softwares such as ADS, Sonnet and Microwave Office adopt the MoM method, while EMPIRE and XFDTD adopt the FDTD method.

For better explaining these full wave numerical techniques, detailed descriptions for each full wave numerical technique are followed.

A. Finite difference time domain method, FDTD

The discretion of FDTD method should take consider of the complete structure and the interested frequency range. The dimension of the discretized cells should be applied to the whole structure including the thinnest section and should not exceed to one tenth of the shortest wavelength in the frequency range.

The discretized cell, which is defined as Yee cell [26], is illustrated in Fig. 1.1.

The electromagnetic field components, H_x , H_y , H_z , E_x , E_y , E_z , are defined as below.

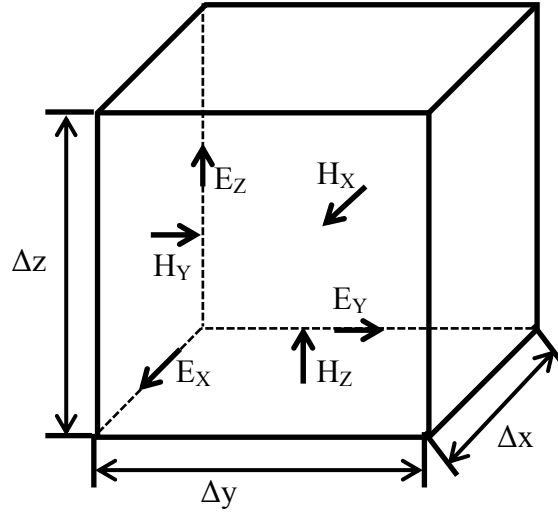


Fig. 1.1: FDTD cell with electromagnetic field components [26].

(1.12) and (1.13) are the Yee cell expressions in a rectangular coordinate system [21].

$$\begin{pmatrix} \frac{\partial H_Z}{\partial y} & \frac{\partial H_Y}{\partial z} \\ \frac{\partial H_X}{\partial z} & \frac{\partial H_Z}{\partial x} \\ \frac{\partial H_Y}{\partial x} & \frac{\partial H_X}{\partial y} \end{pmatrix} = \begin{pmatrix} \epsilon \frac{\partial E_X}{\partial t} \\ \epsilon \frac{\partial E_Y}{\partial t} \\ \epsilon \frac{\partial E_Z}{\partial t} \end{pmatrix} + \begin{pmatrix} J_X \\ J_Y \\ J_Z \end{pmatrix} \quad (1.12)$$

$$\begin{pmatrix} \frac{\partial E_Z}{\partial y} & \frac{\partial E_Y}{\partial z} \\ \frac{\partial E_X}{\partial z} & \frac{\partial E_Z}{\partial x} \\ \frac{\partial E_Y}{\partial x} & \frac{\partial E_X}{\partial y} \end{pmatrix} = \begin{pmatrix} -\mu \frac{\partial H_X}{\partial t} \\ -\mu \frac{\partial H_Y}{\partial t} \\ -\mu \frac{\partial H_Z}{\partial t} \end{pmatrix} \quad (1.13)$$

The basic FDTD equations can be derived by substituting time and spatial partial derivatives with finite difference expressions [21].

The equations are then solved by:

1. Computing the electric field components throughout the whole structure.
2. Reduce the time step by $\Delta t/2$, in which Δt refers to the electromagnetic wave propagation time between the nodes.

3. According to the electric field components obtained in 1, compute the magnetic field components throughout the whole structure.
4. Advance time by $\Delta t/2$ and repeat the procedure from 1.

B. Finite element method, FEM

To explain the FEM method, a partial differential equation (PDE) described by the function u is considered first as (1.14) [22]:

$$Lu = f \quad (1.14)$$

where L is a PDE operator and f is the excitation function. In order to formulate the function, the investigated structure should be discretized into finite elements. Each finite element can be expressed as a sum of known basis functions u_{ei} , with unknown coefficients α_i . Hence, the function F_e for each FEM element can be written as (1.15):

$$F_e = \sum_{\forall i} \alpha_i u_{ei} \quad (1.15)$$

where the value of i is decided by the type of finite elements, as shown in Fig. 1.2 [27]. For example, for the two-dimensional rectangular elements, $i = 4$.

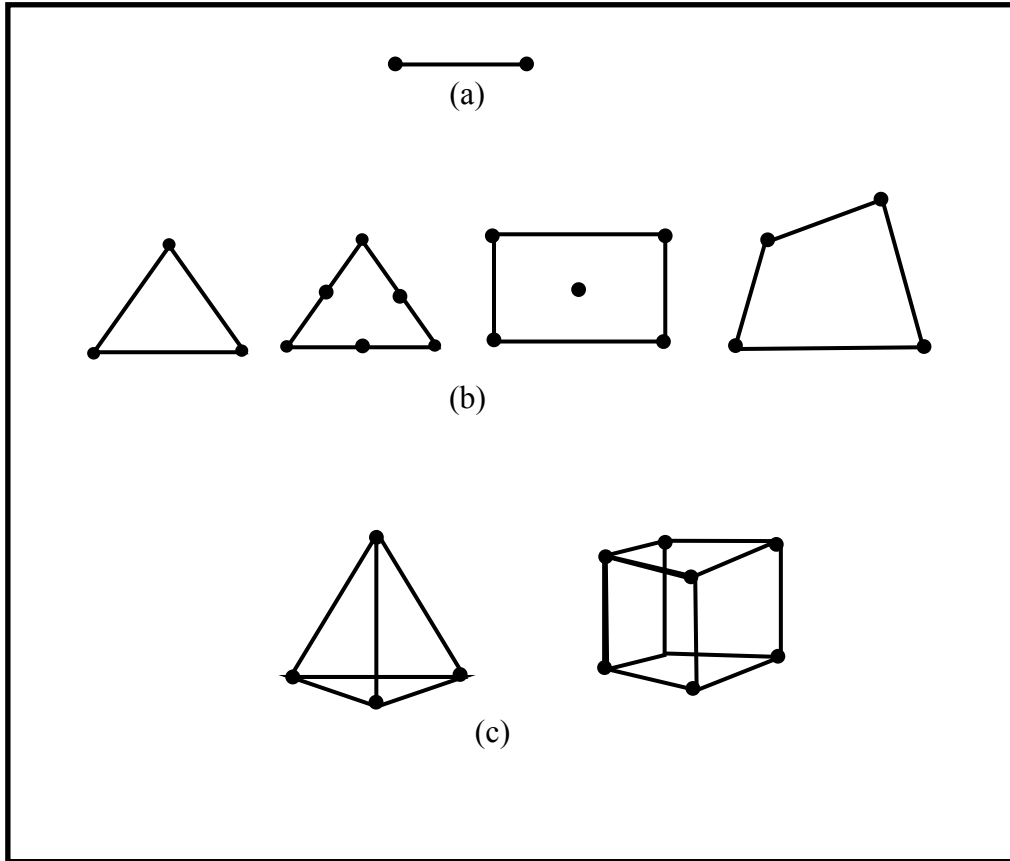


Fig. 1.2: The type of finite elements used in discretization: (a) One-dimensional, (b) two-dimensional, and (c) three-dimensional [27].

Therefore, the total function F in FEM method can be expressed as the sum of the function F_e for each FEM element as in (1.16)

$$F = \sum_{\forall e} F_e \quad (1.16)$$

where e is the number of finite elements in the discretized structure.

At last, the function has to be minimized for the entire region and solved for the unknown value α_i .

Compared with FDTD method, FEM method can be used to handle more complex geometries and more complex loading conditions.

C. Method of moments, MoM

The theoretical derivation [23] of MoM method should be initiated by the proper Green's function G applied to an unknown function I with a linear operator L as shown in (1.17):

$$LI=f \quad (1.17)$$

where f is the known excitation function for the system.

In the next step, the function I can be expanded as a series of functions u_i with unknown parameters I_i , as in (1.18):

$$I = \sum_{i=1}^n I_i u_i \quad (1.18)$$

where u_i are known functions, called basis functions. Since the values of I_i are unknown, we need to combine (1.17) and (1.18) to derive n equations [27].

This will lead the final expression for the problem to be in matrix form as (1.19)

$$[Z][I] = [V] \quad (1.19)$$

where $[V]$ refers to voltage matrix, $[Z]$ refers to generalized impedance matrix and $[I]$ refers to current matrix.

D. Partial element equivalent circuit method, PEEC

In order to derive the theoretical expression for PEEC method, the total electric field \mathbf{E} at observation point \mathbf{r} is firstly expressed as in (1.20) [25]

$$\mathbf{E}(\mathbf{r}, \omega) = -j\omega\mathbf{A}(\mathbf{r}, \omega) - \nabla\Phi(\mathbf{r}, \omega) \quad (1.20)$$

where Φ refers to the scalar electric potential and \mathbf{A} refers to the vector magnetic potential which can be expressed by (1.21)[28]

$$\mathbf{A}(\mathbf{r}, \omega) = \mu \int_{v'} G(\mathbf{r}, \mathbf{r}') \mathbf{J}(\mathbf{r}', \omega) dv' \quad (1.21)$$

where v' is the volume of the conductor, G is the free-space Green's function and \mathbf{J} is the volume current density at a source point \mathbf{r}' .

The expression of Φ can be derived by (1.22) [28]

$$\Phi(\mathbf{r}, \omega) = \frac{1}{\epsilon} \int_{v'} G(\mathbf{r}, \mathbf{r}') q(\mathbf{r}', \omega) dv' \quad (1.22)$$

where q is the charge density at the conductor.

The full expression for the total electric field \mathbf{E} at observation point \mathbf{r} can be obtained by substituting the expressions of \mathbf{A} and Φ into (1.20), as shown below

$$\mathbf{E}(\mathbf{r}, \omega) = -j\omega\mu \int_{v'} G(\mathbf{r}, \mathbf{r}') \mathbf{J}(\mathbf{r}', \omega) dv' - \frac{\nabla}{\epsilon} \int_{v'} G(\mathbf{r}, \mathbf{r}') q(\mathbf{r}', \omega) dv' \quad (1.23)$$

For solving (1.23), a group of pulse basis functions with unknown parameters can be used to substitute the unknown variables \mathbf{J} and q [25]. Weighting functions are applied in those pulse functions as the method introduced in [27]. The geometry is discretized as shown in Fig. 1.3 [25].

According to this discretization strategy, every item in (1.23) can be equivalent to circuit elements [25]. The first item in the right hand side is the sum of the voltage drop over the self-partial inductance between the nodes and the mutual partial inductance between the volume cells. The second item in the right hand side is the sum of the potential difference over the self-partial capacitance between the nodes and the mutual partial capacitance between the surface cells. And the item in the left hand side is the voltage drop over a volume cell.

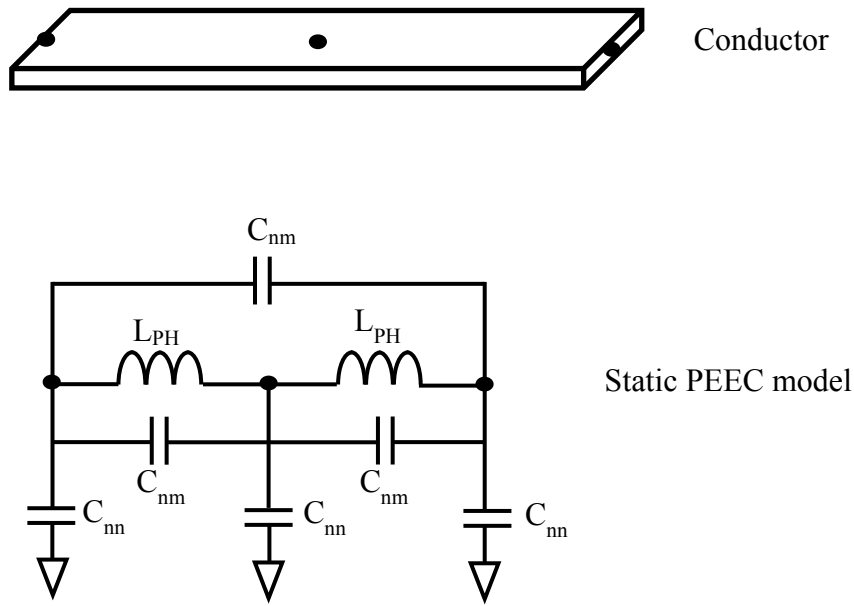


Fig. 1.3: Quasi-static PEEC model for simple conductor geometry [25].

The direct results of the PEEC method are circuit variables. For field variables, post-processing work is needed.

1.3.2 Analytical methods

Analytical methods are another approach for the modeling of radiated emission from interconnects. The basic mechanism to calculate the radiated emission from interconnects can be expressed as (1.24) [5]:

$$\mathbf{E}(f) = \mathbf{T}_E(f)\mathbf{I}(f) \tag{1.24}$$

where $\mathbf{E}(f)$ is the electric field, $\mathbf{T}_E(f)$ is the electric transfer function and $\mathbf{I}(f)$ is the spectrum of the current at a generic point of the interconnect. Hence, finding proper way to compute the current $\mathbf{I}(f)$ and express $\mathbf{T}_E(f)$ is the main work.

Since most radiating interconnects can be easily modeled by transmission lines or wire antennas, calculating the interconnect current by transmission line theory and deriving the closed-form transfer function by the small dipole theory are adopted in many papers [29]-[32]. The main concept is to segment an interconnect into many short Hertzian dipoles. The electromagnetic field radiated by this line is then the combination of all electromagnetic field from each constituent dipole.

The detailed procedure is:

1. Divide the investigated interconnect into a number of electrically short segments with length dl sufficiently shorter than the wavelength of the interest frequency.
2. Calculate the distributed current along the interconnect by transmission line theory.
3. Derive the electric field for each segment by treating it as a small dipole, which indicates that the transfer function is derived based on dyadic Green's function.
4. Compute the total electric field by summing the electric field contributions for all segments including the contribution of the image current.

By adopting this analytical method, closed form expressions can be derived not only for the radiated emission from the interconnects, but also for the radiated emission from the cables attached to printed circuit boards (PCBs) and the small apertures [29]. The method is further used for the validation of some EMI design guidelines for interconnects [29], [33]. In addition, a closed

form expression for the total radiated power of a microstrip transmission line can be derived based on this method [30].

It is noted that the transmission line theory can only be used to calculate the distributed current in straight interconnects. In reality, other interconnect structures are common. Different methods are proposed in [34]-[37] to calculate the distributed current in L-shaped interconnects based on the small dipole theory. [34] obtains the distributed current by MoM technique, while [35], [36] obtains the distributed current by another numerical method called travelling wave method (TWM). And [37] obtains the distributed current through the lumped circuit equivalent model using programs based on equivalent circuit methods and full wave EM techniques. Although these methods can provide accurate results, the implementation of numerical methods leads to the time consuming problem.

For the interconnects in digital circuits, the load might be a non-linear dynamic digital device. In this condition, the distributed current cannot be simply derived by transmission line theory. In [38] and [39], it is suggested to derive the distributed current in a circuit simulator with the use of proper capacitors to model digital receivers. Hence, the radiated emissions from the interconnects connecting to operating digital devices can be easily modeled.

In EMC problems, the maximum radiated emission is the most critical value. Hence, the early papers [29]-[39] focus the investigation of radiated emission on the maximum radiated emission direction only. In order to reduce the calculate complexity, they purposely choose the case which has the maximum radiated emission along the propagation direction. In this condition, the general dyadic Green's function can be deduced to a simplified expression.

Later papers [40]-[45] consider more general cases, i.e., the radiated emissions of the investigated PCBs in 3-D direction. The closed form of dyadic Green's function is derived in far field by saddle-point method [46]-[48] or by reciprocity application [49]. Based on the closed form dyadic Green's function, in [43] [44] another method is presented to treat the L-shaped interconnect, by using a lumped model to model the bent corner in the circuit simulation process. Compared with [34]-[37], this method is much easier and faster, so it is also adopted in the thesis for L-shaped interconnects. Although almost all the papers adopting this method declare that the agreements between the measurement results and the evaluation results are good, the real comparison plots do not show that in the case of the interconnects in digital circuits. The "agreement" between the measurement results and the evaluation results for the radiated emission from interconnects in digital circuits is only in envelope level with difference varied from 5-20 dB along the maximum radiated emission direction.

It is noted that the analytical method only works in quasi-TEM mode, in which the cross-sectional dimensions of the interconnects are much smaller than the wavelength of interest frequency. The valid frequency range for the quasi-TEM propagation can be calculated as [40]

$$f_{g,stat} \approx \frac{21.3[GHz]}{(w[mm]+2h[mm])\sqrt{\epsilon_r+1}} \quad (1.25)$$

In which w represents the trace width, h represents the dielectric thickness and ϵ_r represents the relative permittivity. In addition, this method is based on the assumption of infinite ground so for the interconnects with very small ground plane, the accuracy of the prediction results will be influenced.

1.3.3 Near-field-far-field (NF-FF) transformation methods

Recently, a popular strategy for modeling the radiated emission from a device under test (DUT) is to perform a transformation from near field scanning results for the field [40]-[62]. The main concept is to reconstruct an equivalent source from the near field scanning firstly, and then derive the far field radiated emission from the reconstructed source by numerical methods. There are many articles introducing the source reconstruction method (SRM) [55], [56], [62]-[65]. The calculated equivalent sources are either electric/magnetic dipoles [50]-[56] or electric/magnetic current sources [57]-[65].

The main advantage of the method is the simplicity and efficiency compared with the traditional full wave numerical methods, as this method does not need to mesh the real PCB with complicated circuit structure.

However, the inverse process tends to produce various solutions, which makes it difficult to find a reliable equivalent model. And it is difficult to balance the resolution of dipoles or current sources with the computation time. The most serious drawback is that for a dynamic signal circuit, which is the case for digital circuits, there is still no way to reconstruct the equivalent source model. Hence, this method is not suitable for the investigation of the interconnect in digital circuits.

1.3.4 Conclusions

Three major kinds of approaches for the modeling of radiated emission from interconnects are introduced. The full wave numerical method is accurate and can be applied for the high frequency range. However, it has the drawback of

significant storage and time computing requirements. The analytical method is the fastest and most convenient method, and good at storage saving. However, the frequency limitation because of the quasi-TEM mode requirement and the infinite ground assumption need to be noted in application. The near-field-far-field (NF-FF) transformation method is faster and easier than the full wave numerical method but slower and more complex than the analytical method. And its drawback for digital circuits makes it not suitable for the investigations in this thesis.

Therefore, the modeling of electromagnetic radiated emission from interconnects is accomplished in this thesis by adopting the improved analytical method with the use of digital behavior models, which are popular in the industry nowadays. Compared with the past work, this thesis not only considers dynamic load conditions, but also the dynamic driver condition for the interconnects.

1.4 Motivation, Scope and Thesis Organization

With the increasing of clock frequencies in digital devices, the electromagnetic emission from interconnects in digital circuits also increases. When the electromagnetic emission reaches a certain level, it may lead to complex EMI problems among digital circuits, which severely influence the performance of digital circuits. Therefore, a stable and reliable digital device with limited electromagnetic emission should be designed. Two regulations restrict the electromagnetic emissions from digital products. One is published

by the FCC in the United States, and the other is published by CISPR. The second one is more adopted in Europe.

Usually, design engineers of digital products tend to separate the SI analysis and EMC analysis, as the SI analysis involves the circuit simulation and the EMC analysis involves full wave electromagnetic simulations. Thus, the design cycle is quite long because of the significant computing time and memory requirements in EMC analysis. To address these problems, this thesis focuses on the modeling of far field radiated emission from the interconnects in digital circuits based on circuit simulation results, which is a practical solution to shorten the design cycle. The research in this thesis focuses on far field effects only and does not include near field effects. Therefore, this thesis does not address possible near field interconnections within a device.

The main contributions of the thesis include:

1. Adopt IBIS models to improve the accuracy of the analytical modeling method for the far field radiated emission from interconnects in digital circuits. Traditionally, IBIS models are only applied in signal integrity analysis and are nowadays widely used in the industry because they provide significant reductions in simulation time and propriety information protection. Compared with past investigations using macro models or lumped models to model digital devices, the largest difference between the measurement results and modeling results can be reduced from 20dB to 10dB. In addition, this modeling method enables the designers to determine the radiated emission from interconnects directly during the SI analysis.

2. Accurately model the far field radiated emission from the interconnects placed between two non-linear dynamic digital devices, i.e., a dynamic source and a dynamic load. The past investigations mainly focus on the interconnects with dynamic load so ignore the influence of the dynamic source on the radiated emission.
3. Investigate the impact of different passive signal integrity improvement techniques on the electromagnetic radiated emission from interconnects in digital devices. This is very useful work for digital circuit design. According to the demonstration, digital designers can quickly estimate the change in the radiated emission when doing SI improvements in the design phase.

The thesis is divided into five chapters. The first chapter gives an overview of the EMC problems and to provide a literature review for the existing modeling methods for the radiated emission from interconnects.

The second chapter starts with the radiation characteristic introduction for a single straight transmission line. The influence of the different transmission line parameters and load impedances on radiated power can be observed from the corresponding comparison plots. The radiated emission modeling method used in the thesis is introduced in the following section in detail. In order to validate the method, it is used to model the radiated emission from different interconnects with different loading conditions, different substrate permittivity, different substrate thickness, different lengths and different geometries. The full wave simulation results obtained by ANSYS HFSS are used as benchmark to validate those modeling results.

In the third chapter, the modeling of radiated emission from the interconnects in digital circuits is investigated. The investigation starts from the introduction of Input/Output Buffer Information Specification (IBIS) models, which are widely used behavioral models for digital devices. The advantages and disadvantages of IBIS models are discussed in the section by comparing with traditional SPICE models. After that, we use IBIS models to model radiated emission from the interconnects in digital circuits with the use of a circuit simulator. In the following section, we extend the application of the method to the digital circuits with different passive SI improvement techniques. This is a meaningful work as the designers can use the demonstrated method to estimate the impact of different SI improvement techniques on the radiated emission.

In the fourth chapter, the radiated emission measurement work is presented. Firstly, the measurement setup is introduced. Then the measurement results for the different interconnects in simple RF circuits are plotted. The measurement results are compared with the radiated emission modeling results which are derived from circuit simulation results by the analytical method. After that, the measurement results for the radiated emission from different interconnects in digital circuits are plotted and compared with the corresponding modeling results. The radiated emission from the interconnects in digital circuits with different passive SI improvement techniques are also measured and compared with the modeling results.

In the last chapter, conclusions are given and future work and recommendations are discussed subsequently.

1.5 List of Publications

- Y. Ji, K. Mouthaan, N. V. Venkatarayalu, “Evaluation of IBIS Modelling Techniques for Signal Integrity Simulations without and with Package Parasitics”, *IEEE Electrical Design of Advanced Packaging & Systems Symposium*, 2010, pp. 1-4.
- Y. Ji, K. Mouthaan, N. V. Venkatarayalu, “Analysis of IBIS Model Performance in Simulation of Simultaneous Switching Noise”, *Asia-Pacific Microwave Conference Proceedings*, 2011, pp. 1007-1010.
- Y. Ji, K. Mouthaan, N. V. Venkatarayalu, “Analysis of Radiated Emission Performance of Various Passive Signal Integrity Improvement Techniques”, *International Symposium on Electromagnetic Compatibility*, Tokyo, 2014, 15A1-B2.

Chapter 2

Modeling of the radiated emission from a single transmission line

2.1 Introduction

In this chapter the radiation characteristic of a single transmission line is investigated. Then an analytical method for the evaluation of radiated emission is introduced. This method is applied for a number of different transmission lines. The modeling results by the analytical method are compared with full wave 3D simulation results which are used as benchmarks here and obtained by commercial software ANSYS HFSS based on the FEM method.

2.2 The radiation characteristics of a single straight transmission line

2.2.1 The impact of transmission line parameters on radiation

In order to investigate the impact of various transmission line parameters (characteristic impedance Z_0 , frequency f , substrate permittivity ϵ_r and substrate thickness h) on the radiation, a group of lossless single straight transmission lines with different parameters are simulated with ANSYS HFSS, a commercial full wave simulator mentioned in chapter 1 as shown in Fig. 2.1. The investigated radiation parameter is the radiated power P_{rad} . Since the

circuit is set for a totally matched condition, the incident power P_{in} is set as 1W with the source impedance Z_S equal to Z_0 , and the load impedance Z_L is also set equal to Z_0 . Z_0 is equal to 50Ω . The length of all the transmission lines is kept equal to a quarter wavelength at 8 GHz, no matter how the other transmission line parameters change.

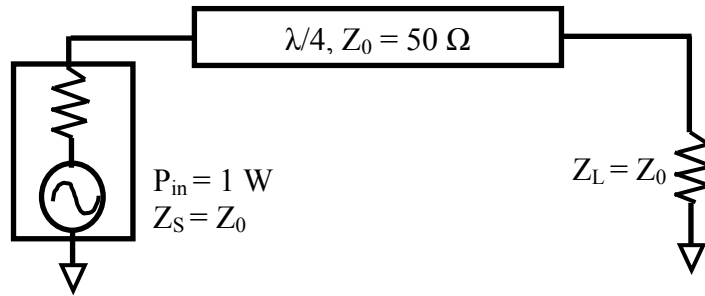


Fig. 2.1: The circuit structure for the evaluation of radiation from a single straight transmission line.

The radiated power can be obtained by simulation directly. For the lossless transmission lines in such condition, it is equal to the value calculated by

$$P_{rad} = P_{in}(1 - |S_{11}|^2 - |S_{21}|^2) \quad (2.1)$$

It should be noted that in real PCBs, conductor loss and dielectric loss also exist. Both of them are related to the PCB material used and they increase with frequency. For a typical 50 Ohm transmission line fabricated on FR4 with 60 mil substrate thickness with a loss tangent of 0.018 and 0.50 oz/ft² copper foil, the conductor loss can reach -0.0002 dB/mm at 1 GHz and -0.00067 dB/mm at 10 GHz. Dielectric loss for such typical transmission line can reach -0.003 dB/mm at 1 GHz and up to -0.029 dB/mm at 10 GHz.

In the thesis, in order to focus the investigation on the radiation property, the conductor loss and dielectric loss are purposely eliminated in the experiment by setting the TL conductor material as perfect conductor and the dielectric material with $\tan\delta=0$. Hence, only in such condition is Equation (2.1) valid.

In the investigation, we keep the substrate thickness same for all the transmission lines as $h = 0.635$ mm, but vary the substrate permittivity ϵ_r . The corresponding transmission line dimension data, i.e. width (W) and length (L), are derived as shown in Table 2.1. The variances of width and length are used to ensure the same Z_0 (50Ω) and electrical length ($\lambda/4$) for the TLs with different substrate permittivity as indicated in Fig.2.1. Hence, no matter how the substrate permittivity changes, the characteristic impedance and electrical length are kept the same by adjusting the TL width and length. The frequency range for the simulation is 4-6 GHz.

Table 2.1: The transmission line geometry parameters

$\epsilon_r = 2.2$		$\epsilon_r = 6.15$		$\epsilon_r = 10.2$	
Width (mm)	Length (mm)	Width (mm)	Length (mm)	Width (mm)	Length (mm)
1.91	6.82	0.90	4.45	0.57	3.59

The radiated power for the single straight transmission line with different ϵ_r and f are plotted in Fig. 2.2, by keeping $h = 0.635$ mm. According to these results, it is observed that:

1. For the same substrate, the radiated power increases when f increases.
2. For the same frequency and substrate thickness, the radiated power increases with decreasing ϵ_r .

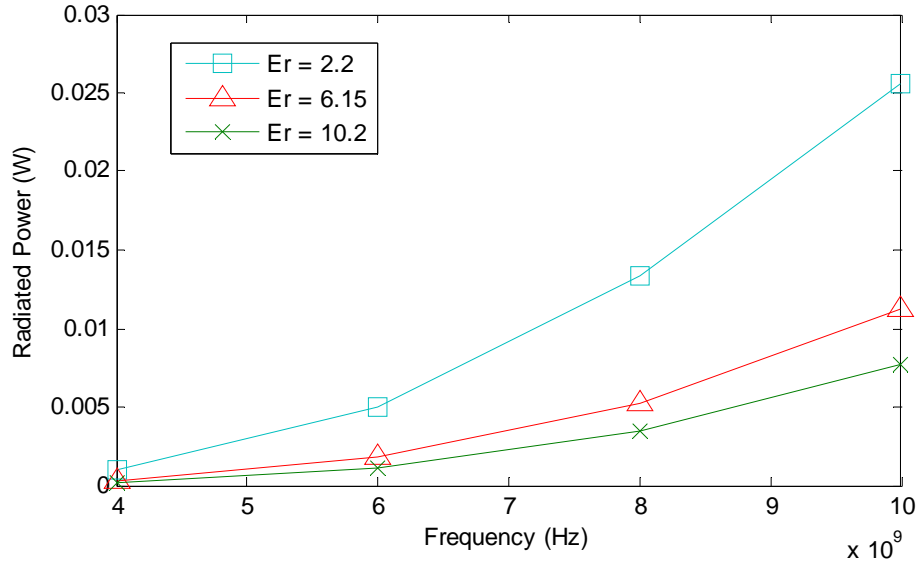


Fig. 2.2: The radiated power for the single straight transmission lines with different ϵ_r and f when $h = 0.635$ mm.

In order to explain the second observation, a microstrip transmission line can be considered as a patch antenna. When h keeps constant, decreasing ϵ_r makes the fringing fields at the edges of the patch antenna become more bowed, i.e., the fringing fields can extend further away, so the radiation is strengthened [66].

In addition, the radiation of a microstrip line is also inversely proportional to W/h ratio when the trace current keeps constant and other geometry values are unchanged. It is because the width of the current spread in the return path is inversely proportional to W/h ratio. And the wider the current spread, the lower the inductance of the return path is, which further leads to the lower noise voltage and hence the lower radiation levels. Since the radiation from the return path is opposite to the radiation from the trace, the total radiation of the microstrip line is increased with the decrease of the

radiation from the return path. Hence, the radiation of the microstrip line is increased with the decrease of W/h ratio.

In conclusion, radiation increases with decreasing substrate permittivity ϵ_r , increasing frequency f and decreasing W/h ratio.

2.2.2 The impact of single straight transmission line discontinuity on radiation

The impact of lossless single straight transmission line discontinuity on the radiated power is investigated in this section. The transmission line is defined as $W = 1.9$ mm, $L = 6.8$ mm, $\epsilon_r = 2.2$, and $h = 0.635$ mm. The circuit setup is shown in Fig. 2.3. The input power is set as 1 W with 50Ω source impedance. The discontinuity is modeled by different load impedance Z_L which is in the range of $[0, 1000] + j*[-1000, 1000] \Omega$.

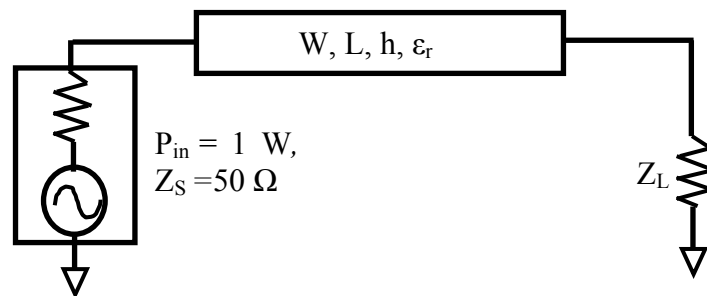


Fig. 2.3: The circuit structure for the evaluation of radiation from a single straight transmission line.

Fig. 2.4 presents the radiated power of the single straight transmission line under different loading conditions at 4 GHz and 8 GHz. The radiated power is directly obtained by ANYS HFSS simulation. It can be observed that the radiated power varies a lot with the load impedance change. It is because

the current along the transmission lines varies with the different load impedance. At 4 GHz, the electrical length of the transmission line is around one eighth of the wavelength, so the peak of the radiated power happens at $Z_L = 0$ because of the maximum current at this load condition. At 8 GHz, the electrical length of the transmission line is around one quarter of the wavelength, so the valley of the radiated power occurs at around $Z_L = 0$ because of the minimum current at this load condition. Furthermore, it is found that the radiated power at higher frequency (8 GHz) is always much higher than the radiated power at lower frequency (4 GHz), which is consistent with the conclusion in the previous section.

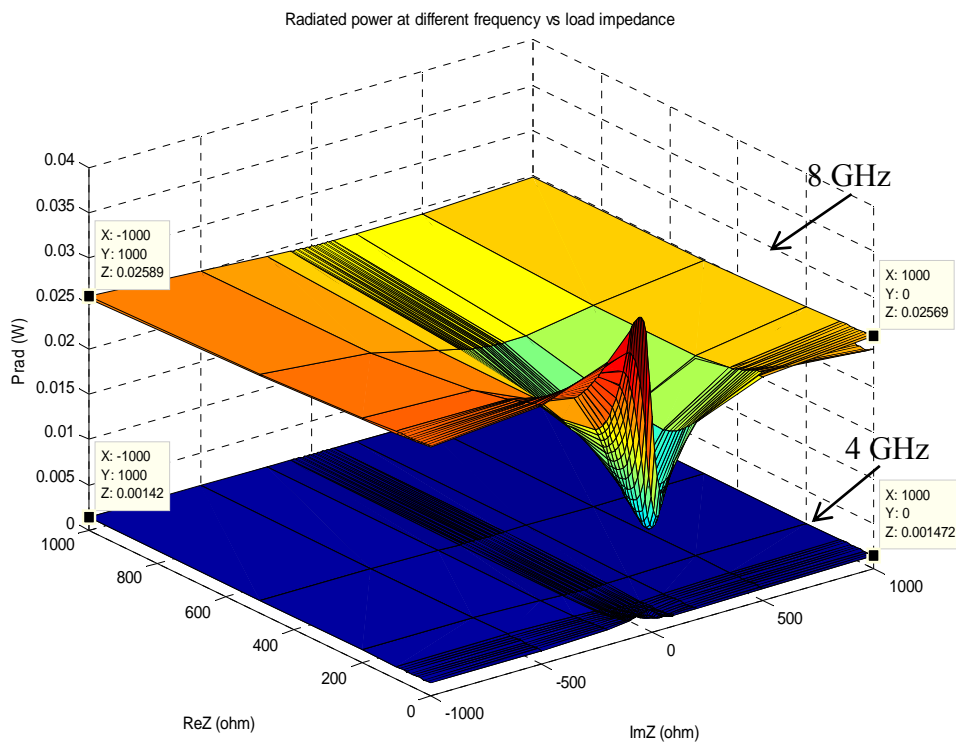


Fig. 2.4: The radiated power for a single straight transmission line under different loading conditions.

The radiated power can also be predicted by using ADS circuit simulation. The first step is to simulate the lossless transmission line in HFSS

to obtain its S parameters by full wave simulation. In ADS, we can directly connect the S parameter dataset block with different loads and use the circuit simulator to obtain the voltages and currents at the input and output ports, which makes the input and output power available. Then the radiated power can be derived as the difference between the input power and the output power. The results agree well with the HFSS results. The main advantage of the method is the reduction in computation time by comparing with the full wave simulation when loads are varied.

2.3 The modeling method for the radiated emission

2.3.1 The radiated emission for the Hertzian dipole

Since the analytical method adopted in the thesis is based on the dipole theory, a good understanding for the radiation characteristic for the Hertzian dipole is necessary.

The Hertzian dipole is defined as an infinitesimal current segment with a phasor current I kept the same along the segment length [67]. Assume the dipole is placed along the y-axis with length dl as shown in Fig. 2.5.

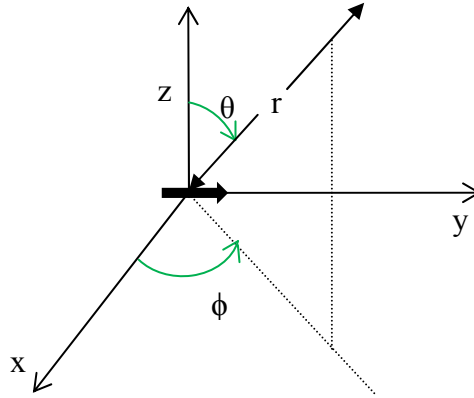


Fig. 2.5: A Hertzian dipole in free space.

For the far field region, the total electric field expression is

$$\bar{E}_\theta = -j\omega\bar{A}_\theta = -j\eta_0\beta_0 \frac{I dl e^{-j\beta_0 r}}{4\pi r} \cos\theta \sin\phi \hat{e}_\theta \quad (2.2)$$

$$\bar{E}_\phi = -j\omega\bar{A}_\phi = -j\eta_0\beta_0 \frac{I dl e^{-j\beta_0 r}}{4\pi r} \cos\phi \hat{e}_\phi \quad (2.3)$$

in which we have

$$\beta_0 = \frac{2\pi}{\lambda_0} = \omega\sqrt{\mu_0\epsilon_0} \text{ and } \eta_0 = \sqrt{\mu_0/\epsilon_0} \quad (2.4)$$

If the dipole is placed above an infinite perfect ground as shown in Fig. 2.6, the total electric field can be derived by using the image theory.

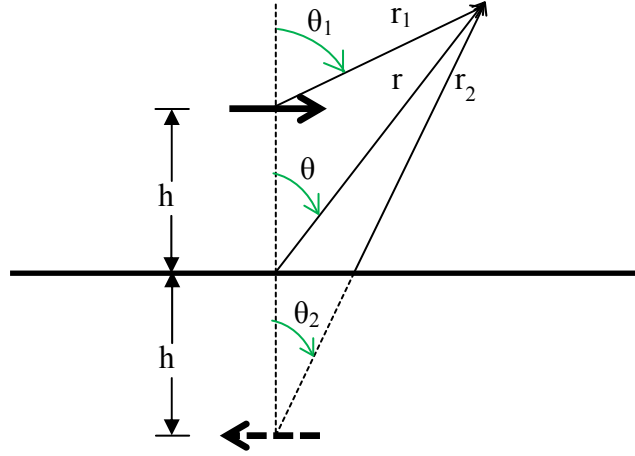


Fig. 2.6: A Hertzian dipole above infinite ground plane.

Since for far-field observations, $\theta_1 \cong \theta \cong \theta_2$, then

$$\text{for phase variations: } \begin{cases} r_1 \cong r - h \cos \theta \\ r_2 \cong r + h \cos \theta \end{cases}$$

$$\text{for amplitude variations: } r_1 \cong r_2 \cong r.$$

Hence, we can derive that

$$\bar{E}_\theta^d = -j\eta_0\beta_0 \frac{I dl e^{-j\beta_0(r-h\cos\theta)}}{4\pi r} \cos \theta \sin \phi \hat{e}_\theta \quad (2.5)$$

$$\bar{E}_\phi^d = -j\eta_0\beta_0 \frac{I dl e^{-j\beta_0(r-h\cos\theta)}}{4\pi r} \cos \phi \hat{e}_\phi \quad (2.6)$$

$$\bar{E}_\theta^r = j\eta_0\beta_0 \frac{I dl e^{-j\beta_0(r+h\cos\theta)}}{4\pi r} \cos \theta \sin \phi \hat{e}_\theta \quad (2.7)$$

$$\bar{E}_\phi^r = j\eta_0\beta_0 \frac{I dl e^{-j\beta_0(r+h\cos\theta)}}{4\pi r} \cos \phi \hat{e}_\phi \quad (2.8)$$

By Euler's formula, we can easily deduce the total electric field of the dipole as

$$\bar{E}_\theta = \bar{E}_\theta^d + \bar{E}_\theta^r = -j\omega\mu_0 \frac{I dl}{4\pi r} e^{-j\beta_0 r} \cos \theta \sin \phi [2j \sin(\beta_0 h \cos \theta)] \hat{e}_\theta \quad (2.9)$$

$$\bar{E}_\phi = \bar{E}_\phi^d + \bar{E}_\phi^r = -j\omega\mu_0 \frac{I dl}{4\pi r} e^{-j\beta_0 r} \cos \phi [2j \sin(\beta_0 h \cos \theta)] \hat{e}_\phi \quad (2.10)$$

2.3.2 The modeling method for the radiated emission from a single transmission line

Nowadays, the widely used modeling methods for the radiated emission from transmission lines include the full wave numerical methods [6]-[20], the analytical method [29]-[43] and the near-field-far field transformation method [50]-[62]. As discussed in section 1.3, the numerical method has the advantage of high accuracy and wide frequency range, but the disadvantage of storage and time consumption. The analytical method is storage and time saving, and can be applied conveniently, but the main trade off is the frequency range limit and the influence of the infinite ground assumption made in the method. The near-field-far field transformation method cannot be applied for time variant circuit, so it is not considered here for the interconnects in digital circuits.

The modeling method adopted here is based on the analytical method. The main concept of the method is to treat the current in the transmission lines as the sum of a number of infinitesimal current segments. The current of each segment, which is the distributed current along the transmission line, can be obtained by transmission line theory and the radiated emission of each segment can be obtained by Green's function. The total radiated emission is the superposition of each segment. Many papers using the analytical method are based on the simplified dyadic Green's function [29]-[34]. The applications are ranged from straight interconnects to bend interconnects, from single layered circuit structure to multi-layered circuit structure. However, compared with the improved analytical method based on full dyadic Green's function [40]-[43], those results are only for the radiation perpendicular to the PCB plane. Therefore, in this thesis, the improved analytical method based on

full dyadic Green's function is adopted for modeling the radiated emission of straight and bend interconnects. Different from [34]-[37], which make use of numerical method for the bend corner modeling, a simple lumped model is used for modeling the bend corner in the thesis, as suggested in [43].

The detailed description of the adopted method is divided into two parts: the distributed current calculation and the field modeling by dyadic Green's function based on the current.

A. The distributed current

When the dimension of a microstrip transmission line cross section is significantly smaller than the signal wavelength, a quasi-TEM mode can be used to describe the wave propagation along the line. In the quasi-TEM mode, signal can be transmitted with small distortion. When the frequency is over the quasi-TEM mode frequency range, the inhomogeneous air/dielectric medium arises the longitudinal field components and degrades the signal integrity (SI) significantly because of the onset of multimodal signal-propagation, intensive radiation, excitation of surface waves, etc. [37]

The frequency range of the quasi-TEM mode can be calculated by (1.13). In this frequency range, the distributed current along the trace can be calculated by transmission-line theory [63]. By assuming the trace along the x-axis, it can be written as

$$I(x) = \frac{V_S}{Z_S + Z_0} \frac{1}{1 - \rho_S \rho_L e^{-j\beta 2l}} (e^{-j\beta x} - \rho_L e^{-j\beta 2l} e^{j\beta x}) \quad (2.11)$$

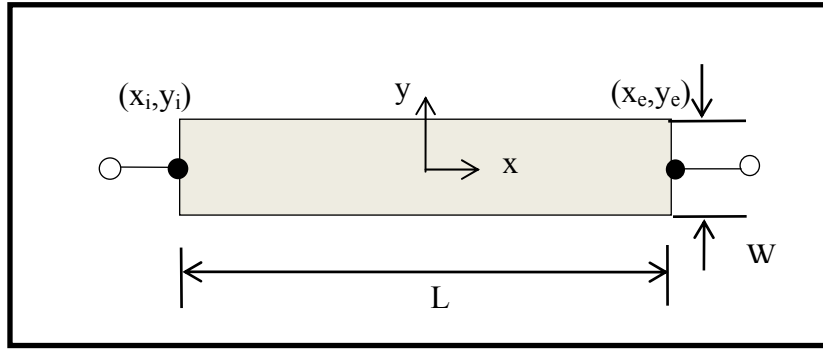
where ρ_S and ρ_L represent the source and load reflection coefficients respectively. In addition, the characteristic impedance Z_0 and the phase constant β are real values, which indicate that the material losses and radiation

losses are neglected. This is a reasonable approximation, as those losses are relatively small for the considered traces.

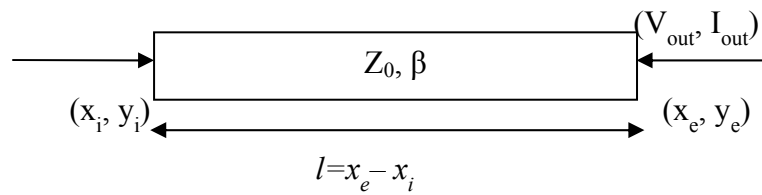
The distributed current can also be obtained with the cooperation of a circuit simulator, which can be widely applied for more complicated circuit structures and interconnect shapes. In the first step, we build a digital circuit in the circuit simulator. The source and load are modeled by the corresponding elements and the interconnects are modeled by the transmission line models. Then the voltage and current at the two-port of the investigated interconnects are simulated. The distributed current along the transmission lines can be derived from the two-port voltages and currents, which are Fourier transformed from the time domain. Fig. 2.7 represents the geometries of a straight transmission line, whose trace direction is assumed along x -axis. The distributed current $I_x(x)$ for the straight transmission line at any position x along the trace can be calculated by transmission line theory and ABCD parameters [39] as:

$$I_x(x) = \frac{1}{2j} \left[\sin(\beta l) \times (I_{out} e^{-j\beta x} + I_{in} e^{-j\beta(x-l)} - I_{out} e^{j\beta x} - I_{in} e^{j\beta(x-l)}) + \right. \\ \left. j \cos(\beta l) \times \left(\frac{V_{in}}{Z_0} e^{j\beta(l-x)} - I_{out} e^{-j\beta x} - I_{out} e^{j\beta x} - \frac{V_{in}}{Z_0} e^{-j\beta(l-x)} \right) \right] \quad (2.12)$$

where $l = x_e - x_i$.



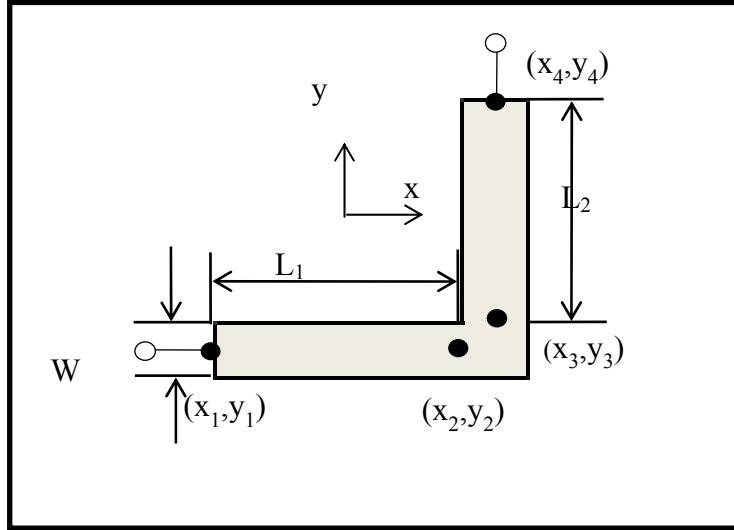
(a)



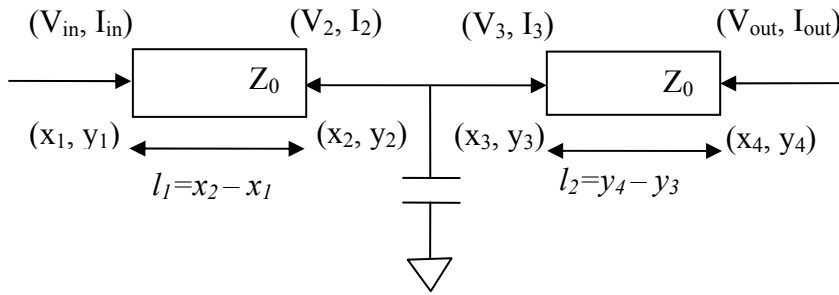
(b)

Fig. 2.7: Geometry and equivalent two-port network of the straight transmission line.

For the transmission line in bend structure, such as L-shaped structure, the second method which is worked with a circuit simulator is applied. A lumped model is used to model the corner effect for simplicity, as shown in Fig. 2.8. The two-port currents and voltages $(V_{in}, I_{in}, V_2, I_2)$ and $(V_3, I_3, V_{out}, I_{out})$ can be easily extracted by circuit simulation. By replacing $(V_{in}, I_{in}, V_{out}, I_{out}, l)$ with $(V_{in}, I_{in}, V_2, I_2, l_1)$ or $(V_3, I_3, V_{out}, I_{out}, l_2)$ in the straight interconnect case, we can obtain the distributed current $I_x(x)$ and $I_y(y)$ in the L-shaped transmission line.



(a)



(b)

Fig. 2.8: Geometry and equivalent two-port network of the L-shaped transmission line.

The capacitance used to model the corner effect can be calculated by the formula as [69]:

for $W/h < 1$

$$\frac{C_{Bend}}{W} = \frac{(14\epsilon_r + 12.5)W - (1.83\epsilon_r - 2.25)}{h\sqrt{W/h}} \text{ pF/m} \quad (2.13)$$

for $W/h > 1$

$$\frac{C_{Bend}}{W} = \frac{(9.5\varepsilon_r + 1.25)W}{h} + 5.2\varepsilon_r + 7.0 \text{ pF/m} \quad (2.14)$$

B. Dyadic Green's function

The radiated emission can be directly computed from the distributed current with the dyadic Green's function. For the straight microstrip transmission line, the radiated emission can be contributed by the x -directed current $I_x(x)$ along the trace in x -direction and the z -directed current $I_x(x_i, y_i)$ and $I_x(x_e, y_e)$ through the via holes at the source and load points respectively, so the total radiated emission $\bar{E}_{str}(\bar{r})$ can be expressed as [39]

$$\begin{aligned} \bar{E}_{str}(\bar{r}) = & \int I_x(x') \bar{G}_x(\bar{r}, \bar{r}') e^{jk_0 \bar{r}' \cdot \hat{e}_r} dx' + \int I_x(x_i, y_i) \bar{G}_z(\bar{r}, \bar{r}') e^{jk_0 \bar{r}' \cdot \hat{e}_r} dz' - \\ & \int I_x(x_e, y_e) \bar{G}_z(\bar{r}, \bar{r}') e^{jk_0 \bar{r}' \cdot \hat{e}_r} dz' \end{aligned} \quad (2.15)$$

where

$$\bar{r}' \cdot \hat{e}_r = x' \sin\theta \cos\phi + y' \sin\theta \sin\phi + z' \cos\theta \quad (2.16)$$

$$\bar{G}_x = \frac{j\omega\mu_0}{4\pi} \left(\frac{e^{-jk_0 r}}{r} \right) \bar{A}_x(\theta, \phi) \quad (2.17)$$

$$\bar{G}_y = \frac{j\omega\mu_0}{4\pi} \left(\frac{e^{-jk_0 r}}{r} \right) \bar{A}_y(\theta, \phi) \quad (2.18)$$

$$\bar{G}_z = \frac{j\omega\mu_0}{4\pi} \left(\frac{e^{-jk_0 r}}{r} \right) \bar{A}_z(\theta, \phi) \quad (2.19)$$

$$\bar{A}_x(\theta, \phi) = (R_v - 1) \cos\theta \cos\phi \cdot \hat{e}_\theta + (R_h + 1) \sin\phi \cdot \hat{e}_\phi \quad (2.20)$$

$$\bar{A}_y(\theta, \phi) = (R_v - 1) \cos\theta \sin\phi \cdot \hat{e}_\theta - (R_h + 1) \cos\phi \cdot \hat{e}_\phi \quad (2.21)$$

$$\bar{A}_z(\theta, \phi) = \frac{(R_v + 1) \sin\theta}{\varepsilon_r \cos(k_0 v h)} \hat{e}_\theta \quad (2.22)$$

$$R_v = \frac{1 - j \left(\frac{v}{\varepsilon_r \cos\theta} \right) \tan(k_0 v h)}{1 + j \left(\frac{v}{\varepsilon_r \cos\theta} \right) \tan(k_0 v h)} \quad (2.23)$$

$$R_h = \frac{1 + j \left(\frac{v}{\cos\theta} \right) \cot(k_0 v h)}{1 - j \left(\frac{v}{\cos\theta} \right) \cot(k_0 v h)} \quad (2.24)$$

$$v = \sqrt{\varepsilon_r - \sin^2\theta} \quad (2.25)$$

For the L-shaped microstrip transmission line, the total radiated emission is the superposition of the radiated emission from the trace part in x direction and the radiated emission from the trace part in y direction. The radiated emission of the trace part in x direction $\bar{E}_x(\bar{r})$ is composed of the x -directed current $I_x(x)$ along the trace in x -direction and the z -directed current $I_x(x_l, y_l)$ through the via hole at the source end. The radiated emission of the trace part in y direction $\bar{E}_y(\bar{r})$ is composed of the y -directed current $I_y(y)$ along the trace in y -direction and the z -directed current $I_y(x_d, y_d)$ through the via hole at the load end. The expressions are shown as below:

$$\bar{E}_x(\bar{r}) = \int I_x(x') \bar{G}_x(\bar{r}, \bar{r}') e^{jk_0 \bar{r}' \cdot \hat{e}_r} dx' + \int I_x(x_1, y_1) \bar{G}_z(\bar{r}, \bar{r}') e^{jk_0 \bar{r}' \cdot \hat{e}_r} dz' \quad (2.26)$$

$$\bar{E}_y(\bar{r}) = \int I_y(y') \bar{G}_y(\bar{r}, \bar{r}') e^{jk_0 \bar{r}' \cdot \hat{e}_r} dy' - \int I_y(x_4, y_4) \bar{G}_z(\bar{r}, \bar{r}') e^{jk_0 \bar{r}' \cdot \hat{e}_r} dz' \quad (2.27)$$

2.4 The application of the modeling method for various transmission lines

2.4.1 The application of the modeling method for the transmission lines under different loading conditions

The analytical method based on dyadic Green's function is adopted to model the radiated emission from a microstrip transmission line in different loading conditions. The modeling results are compared with the results obtained by the HFSS simulations, while the later one is used as a benchmark.

The straight microstrip line is designed as in Fig. 2.9 for the implementation of the method. The substrate has $\epsilon_r = 2.2$, $\tan\delta = 0.001$, $h = 1.6$ mm = 62 mil. The trace dimension is $L = 150$ mm, $W = 4.9$ mm ($Z_0 = 50 \Omega$). The input excitation is set as 1 volt with 50Ω source impedance.

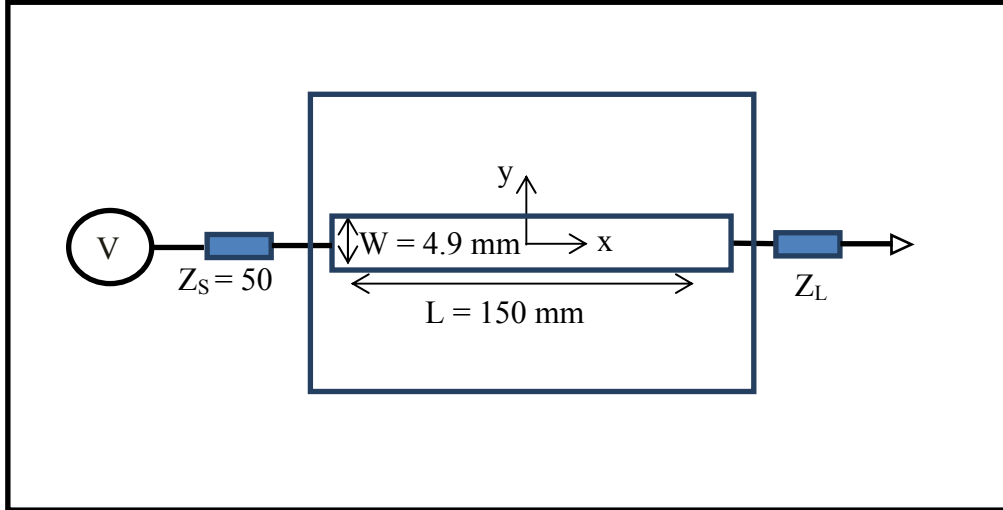
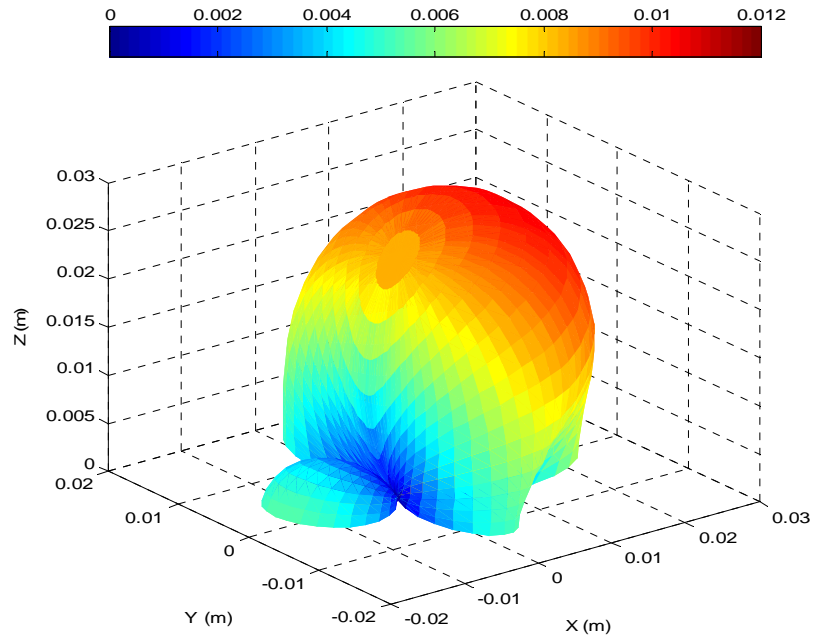
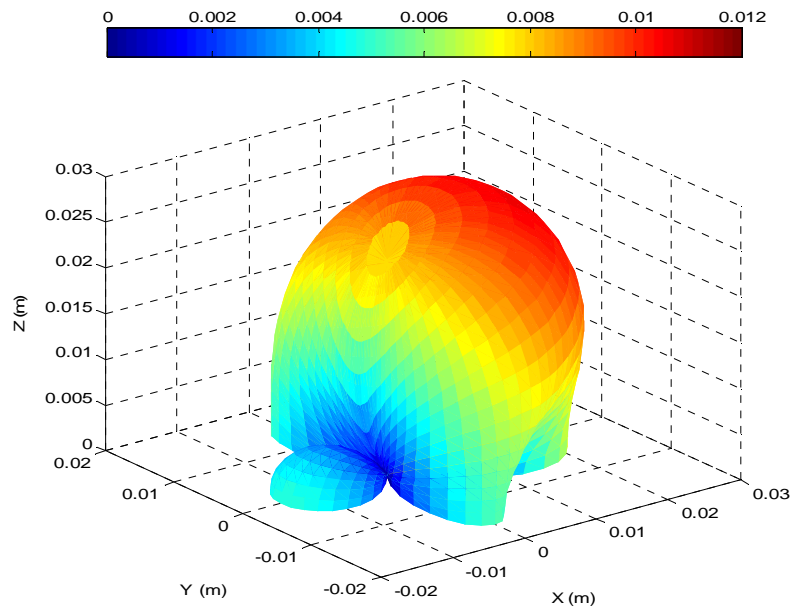


Fig. 2.9: The circuit connection of the straight line.

When the load impedance of the transmission line is set as 50Ω for the matched load condition, the 3D radiation patterns can be obtained by the analytical method based on dyadic Green's function as described in the previous section. Two 3D radiation patterns for the transmission line at 1 GHz are shown in Fig. 2.10, in which (a) represents the HFSS result and (b) represents the modeling result based on Dyadic Green's function. The observation point is 3 meters from the center of the trace in the range of $0 \leq \theta \leq \frac{\pi}{2}$, $0 \leq \phi \leq 2\pi$, as defined in Fig. 2.11.



(a) HFSS simulation results



(b) modeling results based on dyadic Green's function

Fig. 2.10: The 3D radiation pattern for the straight microstrip line with 50Ω (matched) load

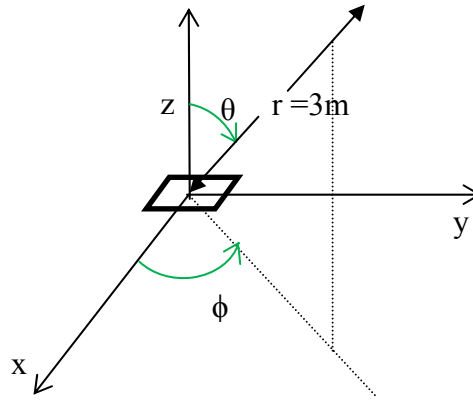


Fig. 2.11: The observation point for 3D radiation pattern plot

The 3D radiated pattern is in the unit of V/m. And since the infinite ground condition is assumed for the method, the results are only shown in upper hemisphere.

It can be easily found that the radiation pattern based on the modeling results by dyadic Green's function is very similar to the radiation pattern by HFSS simulation. The difference between the 3D modeling results by dyadic Green's function and the 3D results by HFSS full wave simulation is further calculated in dB unit and plotted in Fig. 2.12. It can be found that for most of the location points, the two results are agreed well with around 0-0.2 dB differences. At few locations, the differences are large and sometimes close to 10 dB. Those locations are corresponding to the places where the radiated emissions are extremely small and close to 0 dBuV/m, which can be read correspondingly from Fig. 2.10, so the results are very sensitive. The difference for those locations is actually at the same level as the difference in other locations in magnitude. The situation is like two groups of data: (a) 10 vs 9.95 (b) 0.1 vs 0.05. Although the absolute difference for both case is the same (0.05), in dB, the difference for case (a) is 0.044 dB and for case (b) is 6.02dB.

And since the radiation values are already in the unit of dBuV/m, those extremely small values are typically lower than the sensitivity of the radiated emission measurement system. Those small radiated emission values are not the main concern when people consider EM problems. Therefore, it can be concluded that the 3D radiation pattern based on the modeling results by dyadic Green's function agrees well with the HFSS 3D radiation pattern.

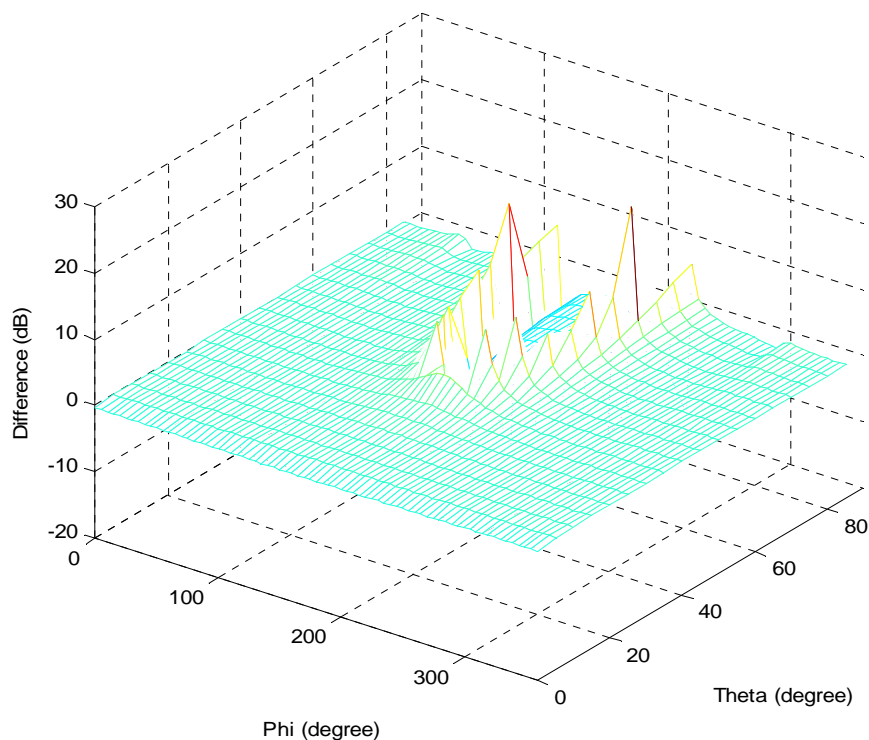
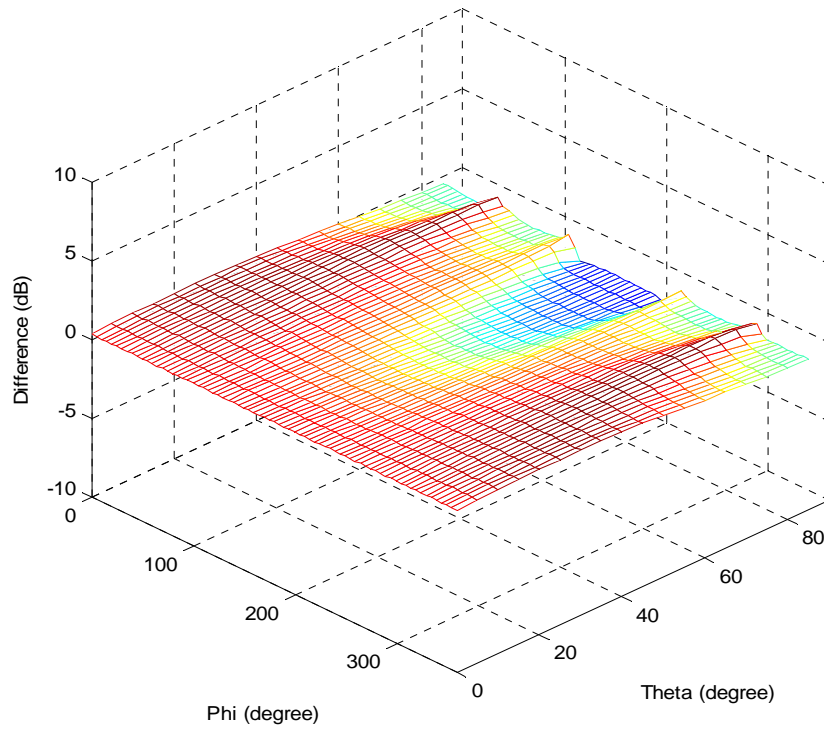


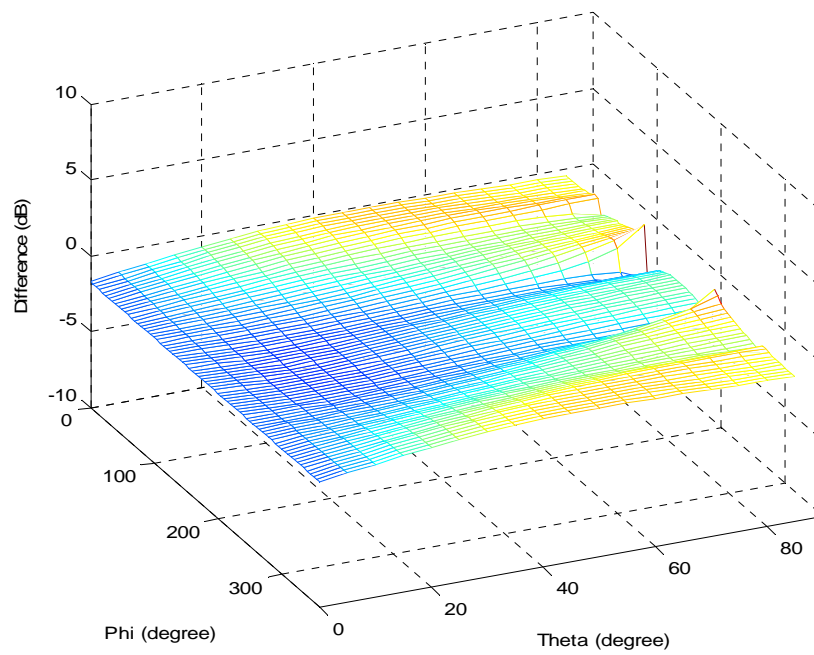
Fig. 2.12: The 3D radiation pattern comparison for the straight microstrip line with matched load condition.

Same investigations are implemented for the straight transmission line with more difference loading conditions. Fig. 2.13 shows the 3D radiation pattern comparisons between the analytical method results and HFSS simulation results for the straight microstrip line when the load impedance is set as (a) $50 \text{ T}\Omega$ for the open end condition, (b) 0Ω for the short end condition, (c) 50 pF for the negative reactance end condition and (d) 50 nH for the

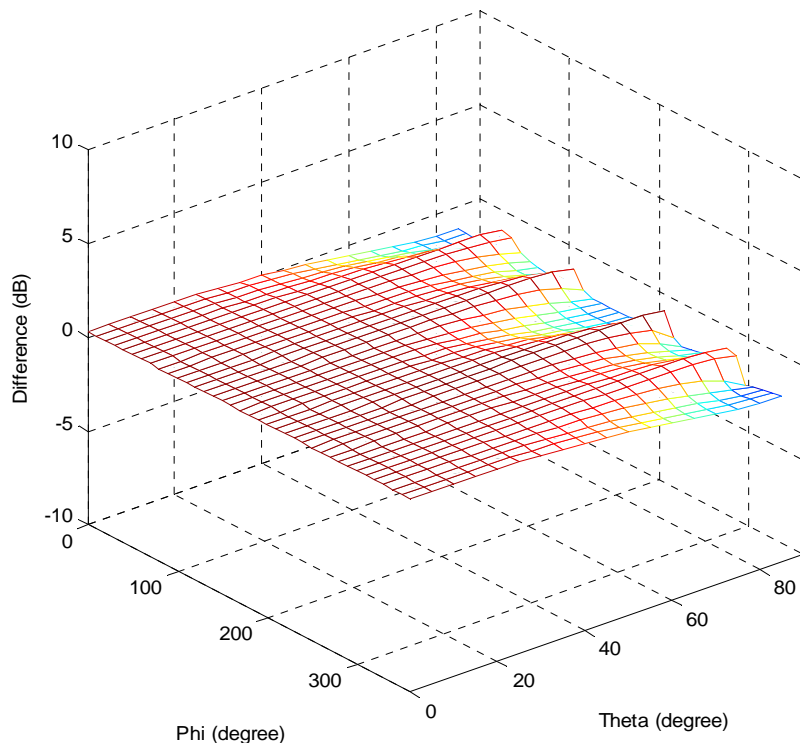
positive reactance end condition. Excellent agreement is presented between the modeling results by dyadic Green's function and the simulation results by HFSS. For a few locations, the difference reaches 3 dB. It is because at those locations the magnitude of the radiated emission is very small. Therefore, in magnitude, the modeling results by dyadic Green's function are still close to the simulation results by HFSS at those locations.



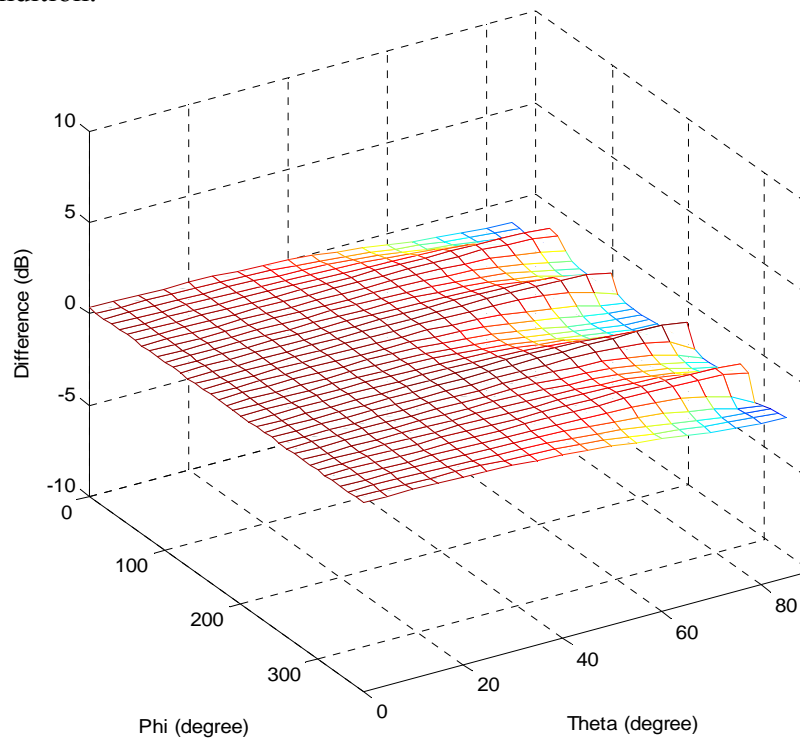
(a) The 3D radiation pattern comparison for the open end condition.



(b) The 3D radiation pattern comparison for the short end condition.



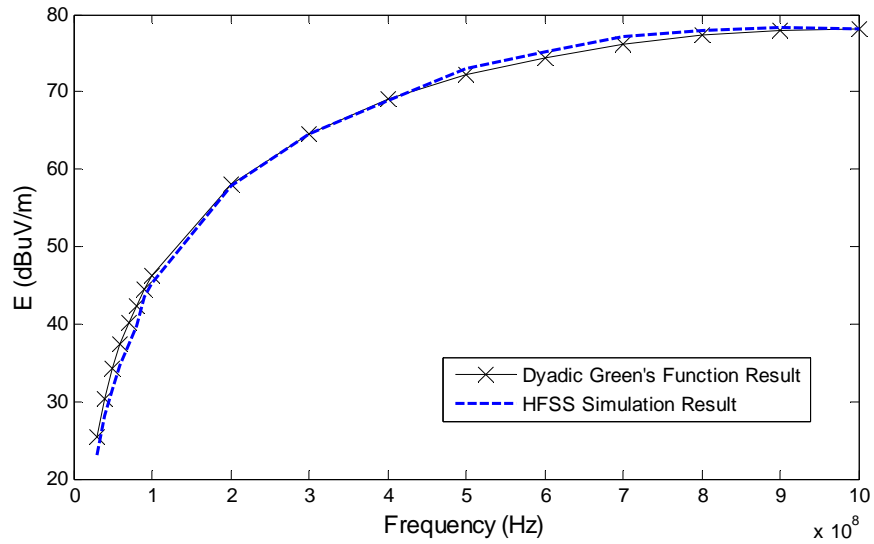
(c) The 3D radiation pattern comparison for the negative reactance load condition.



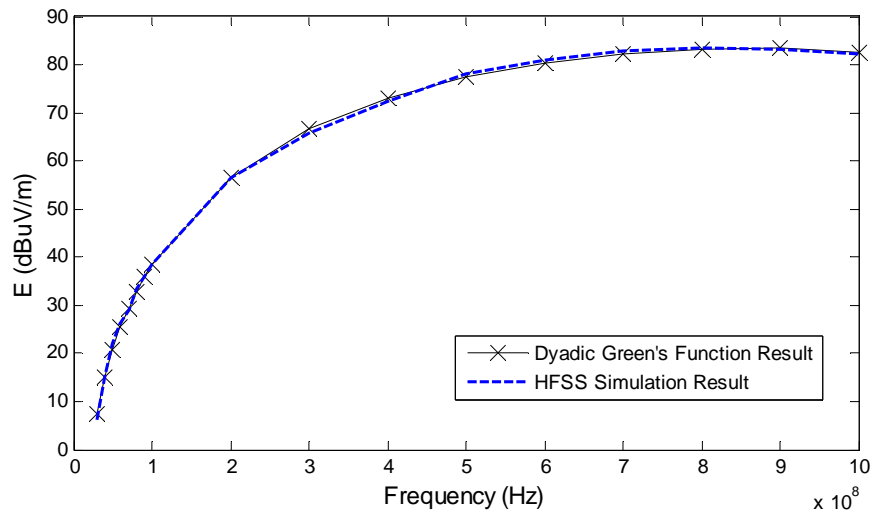
(d) The 3D radiation pattern comparison for the positive reactance load condition.

Fig. 2.13: The 3D radiation pattern comparison for the straight microstrip line with different load conditions.

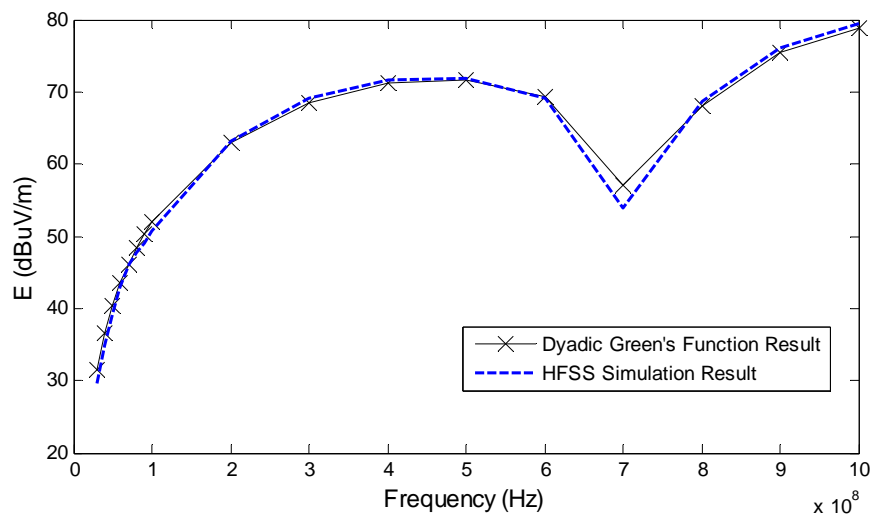
We also simulated the radiated emission for this microstrip line with frequency variance. Fig.2.14 presents the radiated emission from the microstrip line with five different loading conditions at the location of 3 meter from the center of the trace and $\theta = 0^\circ$. The frequency is varied from 30 MHz to 1 GHz. In Fig. 2.14, (a) is the radiated emission for the matched load condition by setting load impedance equals to 50Ω , (b) is the radiated emission for the open end condition by setting load impedance equals to $50 T\Omega$, (c) is the radiated emission for the short end condition by setting load impedance equals to 0Ω , (d) is the radiated emission for the negative reactance end condition by setting load impedance equals to 50 pF and (e) is the radiated emission for the positive reactance end condition by setting load impedance equals to 50 nH . The HFSS simulation result and the modeling result based on dyadic Green's function are shown together and compared. By taking the HFSS result as a benchmark, it can be observed that the results based on analytical modeling method agree very well with the HFSS result through the whole frequency range with the difference less than 1 dB for straight transmission lines.



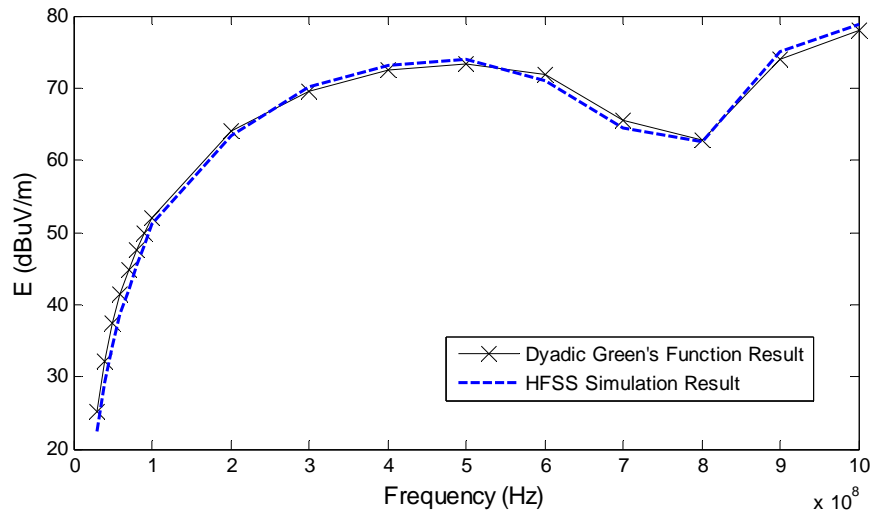
(a) The radiated emission for the matched end condition



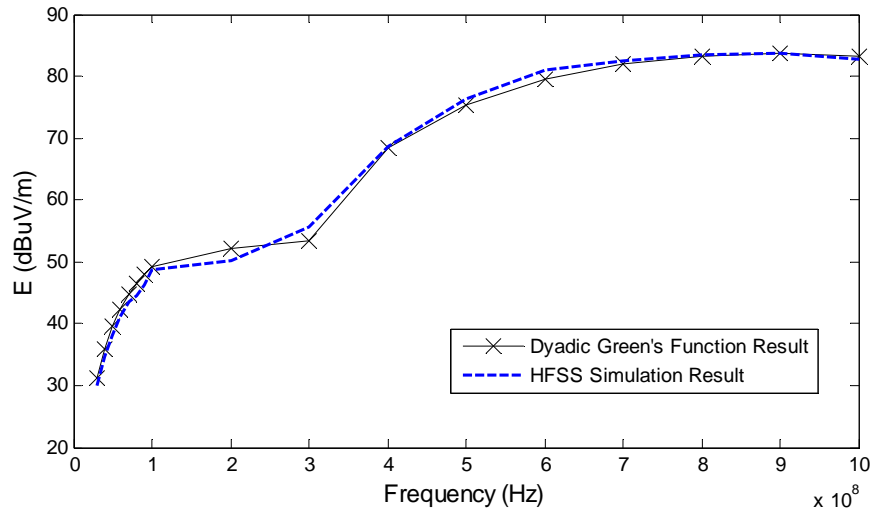
(b) The radiated emission for the open end condition



(c) The radiated emission for the short end condition



(d) The radiated emission for the negative reactance load condition



(e) The radiated emission for the positive reactance load condition

Fig. 2.14: The radiated emissions from the straight microstrip line with different loading conditions.

The radiated emissions from the straight microstrip line in different loading conditions are further compared in Fig. 2.15. It can be found that at high frequency range, i.e., 0.5-1 GHz, the radiated emission of the positive reactance end condition is getting close to the radiation of the open end condition, while the radiated emission of the negative reactance end condition is getting close to the radiation of the short end condition. This is can be easily explained as the higher the frequency, the larger the impedance of the negative reactance end which is represented by an inductor connection and the smaller the impedance of the negative reactance end which is represented by a capacitor connection.

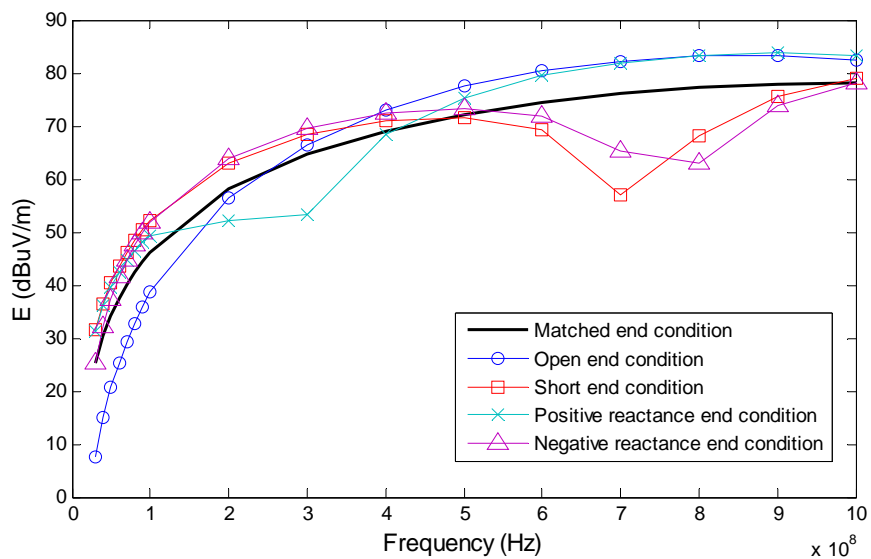


Fig. 2.15: The radiated emission comparison for the straight microstrip line with different loading conditions.

2.4.2 The application of the modeling method for the transmission lines with different materials

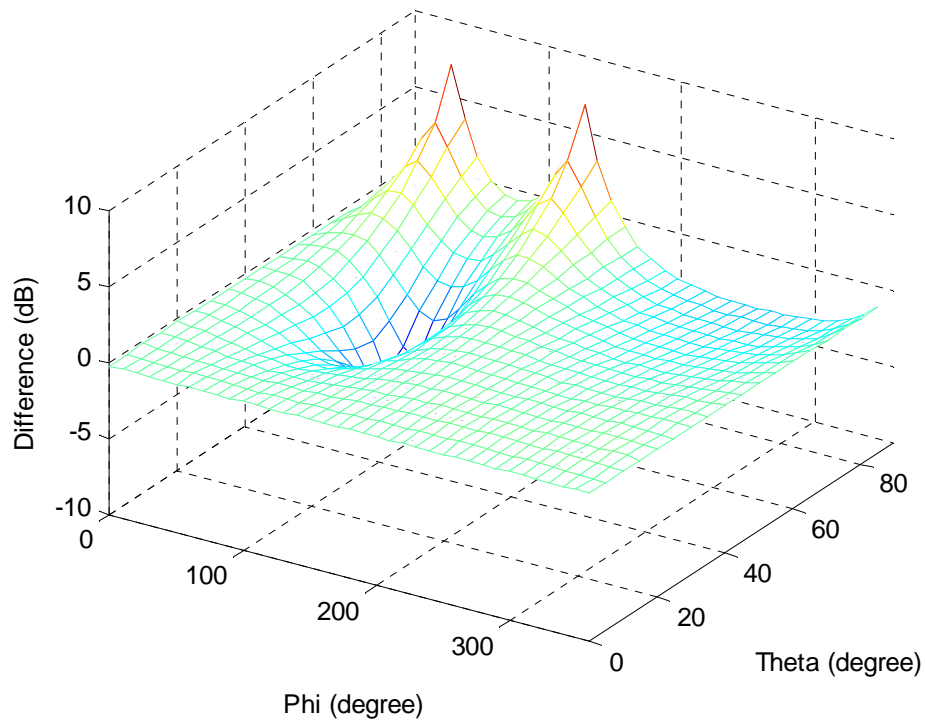
In order to further validate the accuracy of the analytical method based on dyadic Green's function, the investigation is extended to the microstrip transmission lines with different materials. Those results are compared with the results obtained by the HFSS full wave simulations, while the later one is used as a benchmark.

In this section, two groups of straight transmission lines are designed. The first group is designed by keeping the same substrate thickness ($H = 62$ mil = 1.6 mm) but varying the substrate permittivity. The geometry and the circuit connection of these microstrip lines are same as Fig. 2.9 by setting the load impedance $Z_l = 50 \Omega$. The trace dimensions are varied with the substrate permittivity to keep the characteristic impedance equal to 50Ω and the electrical length equal to $\lambda/2$, as listed in Table 2.2.

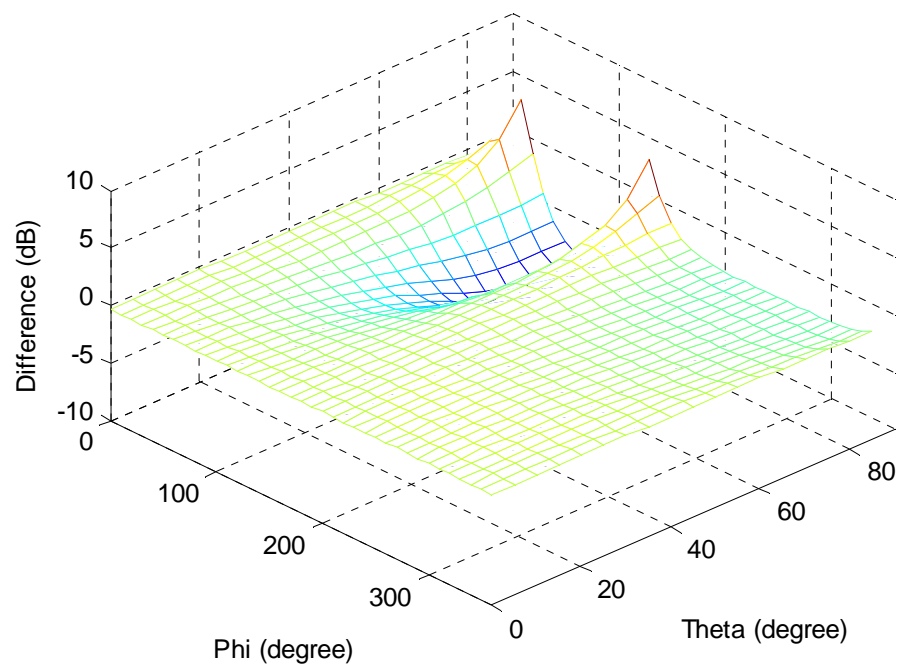
Table 2.2: The transmission line geometry parameters when $H = 62$ mil

$\epsilon_r = 2.2$		$\epsilon_r = 3.38$		$\epsilon_r = 4.4$	
Width (mm)	Length (mm)	Width (mm)	Length (mm)	Width (mm)	Length (mm)
4.88	54.60	3.68	45.8	3.04	41.07

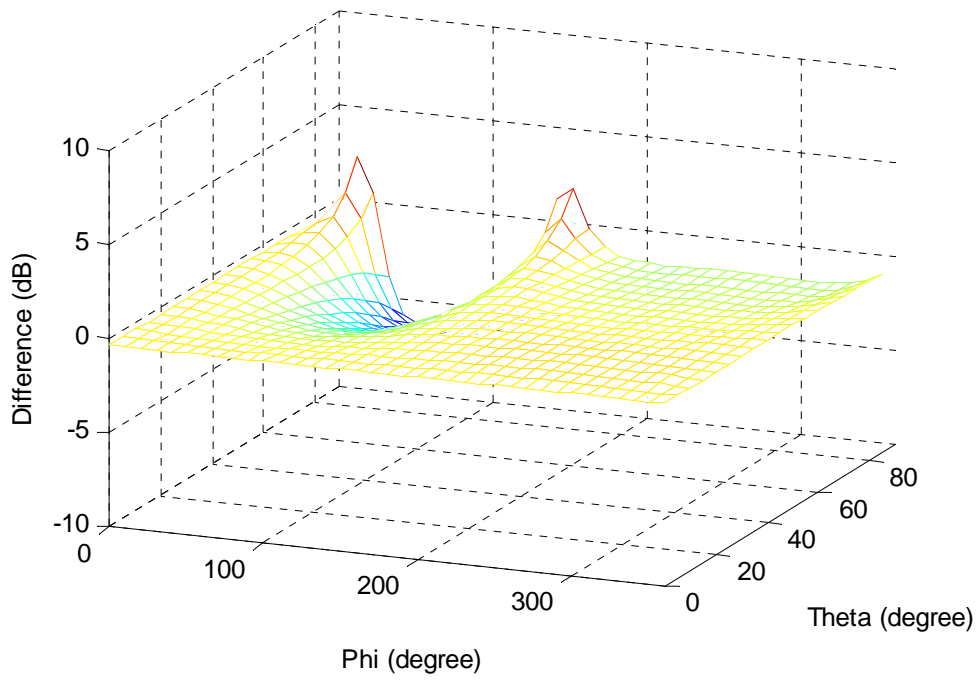
The difference between the 3D radiation pattern by dyadic Green's function and the 3D radiation pattern by HFSS simulation for each trace at 1 GHz is calculated in dB unit and plotted in Fig. 2.16. The observation point is 3 meters from the center of the trace in the range of $0 \leq \theta \leq \frac{\pi}{2}$, $0 \leq \phi \leq 2\pi$, as defined in Fig. 2.11.



(a) The 3D radiation pattern comparison for the transmission line with RT5880 ($\epsilon_r=2.2$).



(b) The 3D radiation pattern comparison for the transmission line with RO4003C ($\epsilon_r=3.38$).

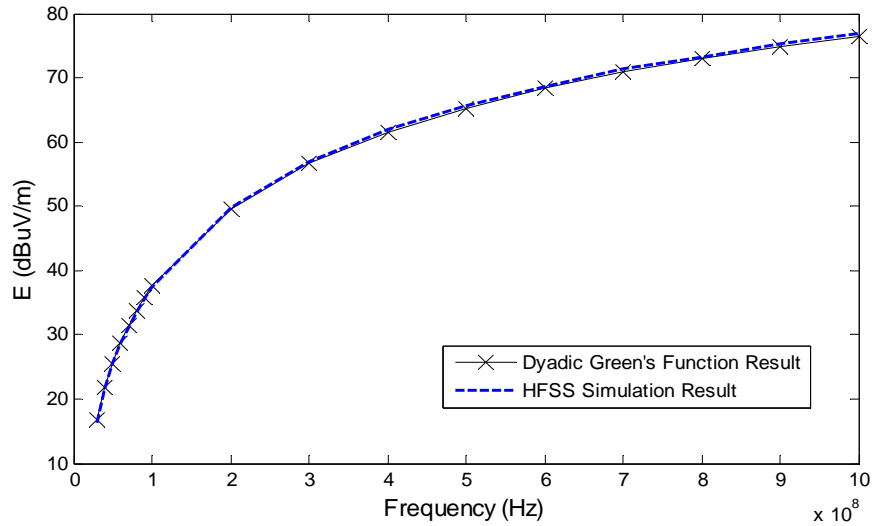


(c) The 3D radiation pattern comparison for the transmission line with FR4 ($\epsilon_r=4.4$).

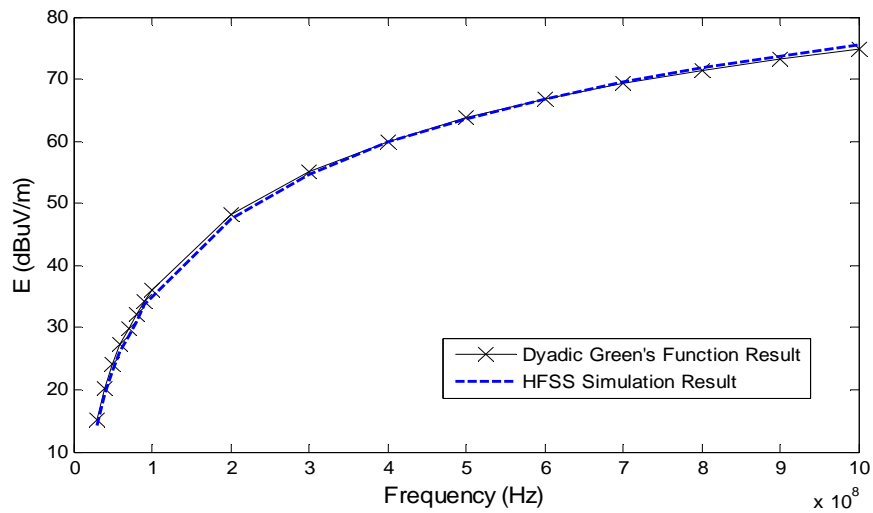
Fig. 2.16: The 3D radiation pattern comparison for the transmission lines with different substrate permittivity.

The differences for most locations are around 0-0.2 dB. However, for some locations, the differences are extremely large and can be close to 7 dB. Same as we discussed before, those locations are corresponding to the places where the radiated emissions are extremely small and close to 0 dBuV/m. Hence, the radiated emissions at these locations are very sensitive. The radiation patterns by the analytical modeling method are actually very similar to the radiation patterns by the HFSS full wave simulations.

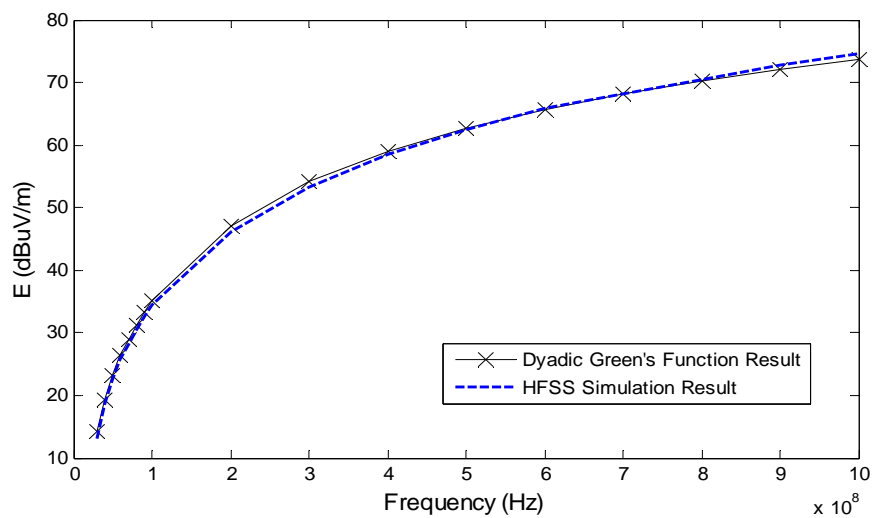
The radiated emission for these microstrip lines with frequency variance (30 MHz to 1 GHz) is plotted in Fig.2.17 when the observation point is 3 meters from the center of the trace at $\theta = 0^\circ$. In Fig.2.16, (a) is the radiated emission for the transmission line with $\epsilon_r = 2.2$, (b) is the radiated emission for the transmission line with $\epsilon_r = 3.38$, (c) is the radiated emission for the transmission line with $\epsilon_r = 4.4$. By observing the plot, it is found that the differences between the modeling results and HFSS simulation results are less than 1 dB. Hence, it can be concluded that no matter how the substrate permittivity changes, the radiated emission calculated by the analytical modeling method agrees well with the radiated emission simulated by HFSS for straight transmission lines.



(a) The radiated emission for the transmission line with RT5880 ($\epsilon_r=2.2$).



(b) The radiated emission for the transmission line with RO4003C ($\epsilon_r=3.38$).



(c) The radiated emission for the transmission line with FR4 ($\epsilon_r=4.4$).

Fig. 2.17: The radiated emissions from the straight microstrip line with different substrate permittivity.

In Fig. 2.18, the radiated emissions from the straight microstrip line with different substrate permittivity are further compared. It can be found that for the transmission line with same electrical length, characteristic impedance and substrate thickness, the radiated emission is increased with the decrease of the substrate permittivity. It is because that decreasing the substrate permittivity makes the fringing fields at the edges of the transmission line become more bowed, i.e., the fringing fields can extend further away, so the radiation is strengthened.

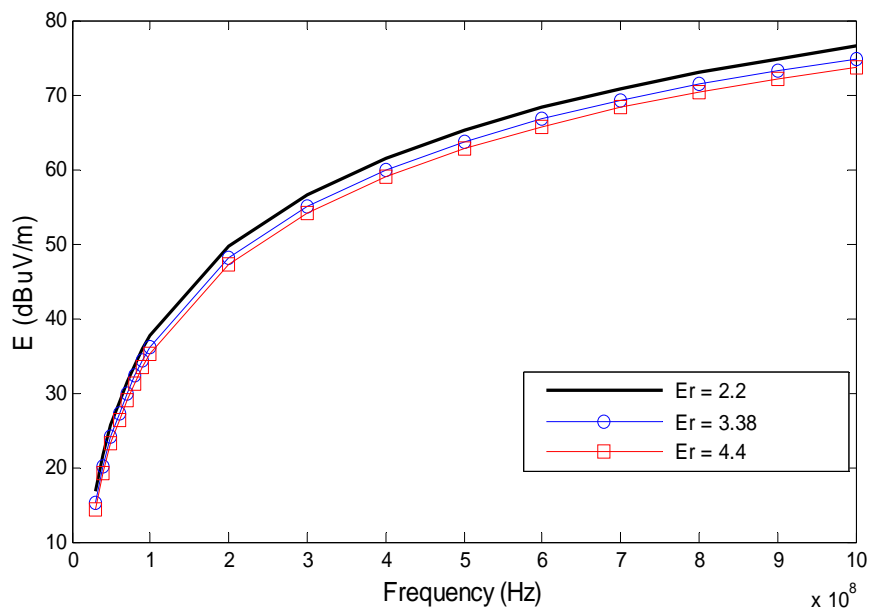


Fig. 2.18: The radiated emission comparison for the straight microstrip line with different substrate permittivity.

The second group of the transmission lines is designed by keeping the same substrate permittivity ($\epsilon_r = 2.2$) but varying the substrate thickness. The geometry and the circuit connection of these microstrip transmission lines are same as Fig. 2.9. The trace dimensions are varied with the substrate thickness to keep the characteristic impedance equal to 50Ω and the electrical length equal to $\lambda/2$, as listed in Table 2.3.

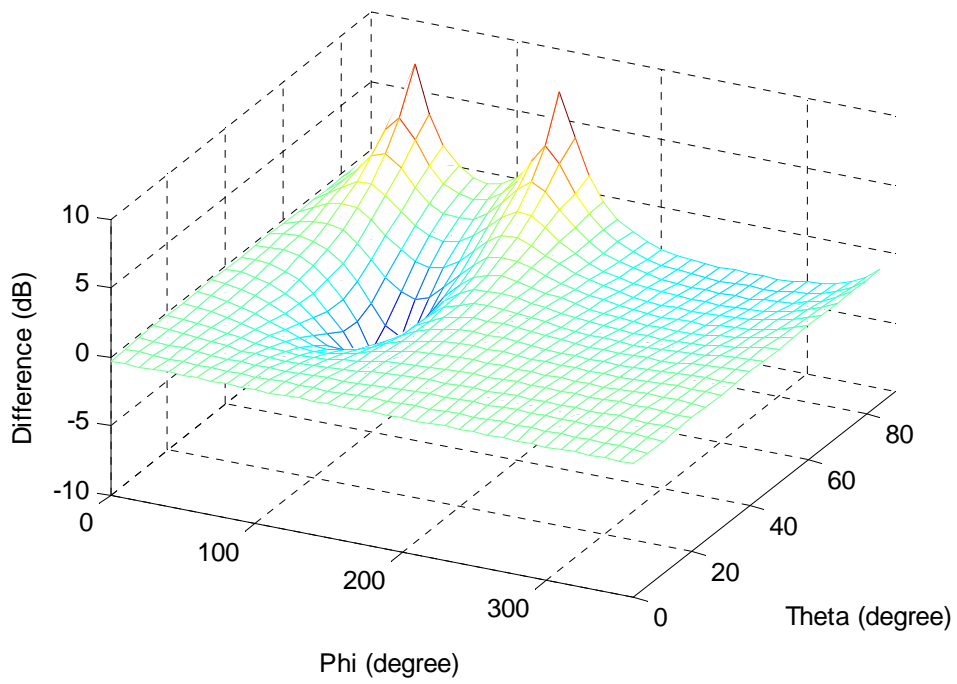
Table 2.3: The transmission line geometry parameters when $\epsilon_r = 2.2$

H = 20 mil		H = 31 mil		H = 62 mil	
Width (mm)	Length (mm)	Width (mm)	Length (mm)	Width (mm)	Length (mm)
1.54	54.77	2.40	54.70	4.88	54.60

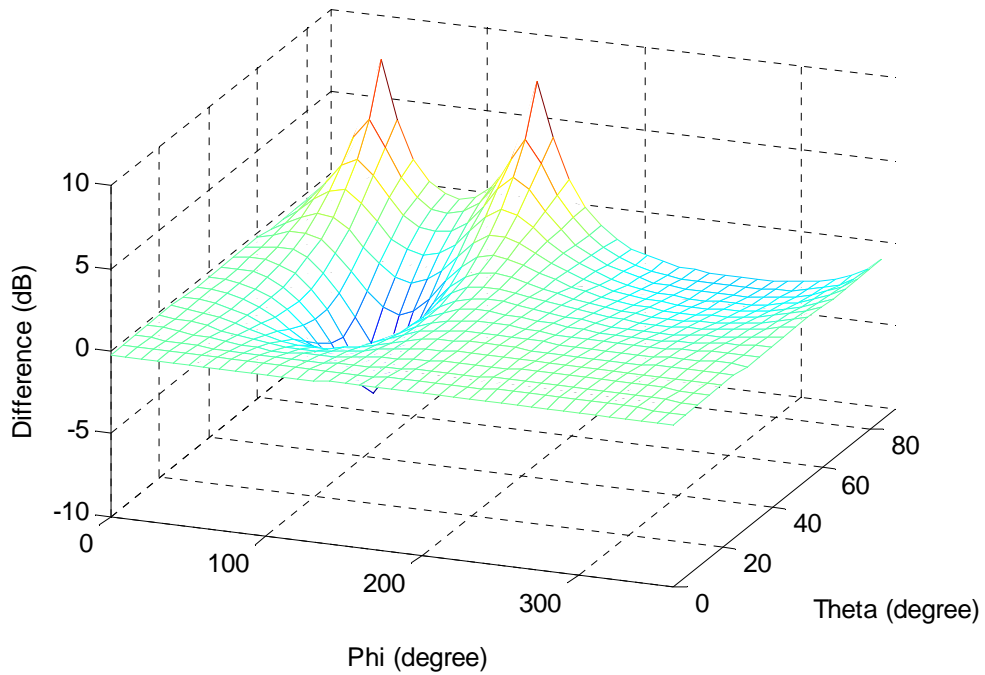
The difference between the 3D radiation pattern by dyadic Green's function and the 3D radiation pattern by HFSS simulation for each trace loaded with matched impedance at 1GHz is calculated in dB unit and plotted in Fig. 2.19. The observation point is 3 meters from the center of the trace in the range of $0 \leq \theta \leq \frac{\pi}{2}, 0 \leq \phi \leq 2\pi$, as defined in Fig. 2.11. In Fig.2.19, (a) is the radiated emission for the transmission line with 20 mil substrate thickness, (b) is the radiated emission for the transmission line with 31 mil substrate thickness, (c) is the radiated emission for the transmission line with 62 mil substrate thickness.

By observing Fig. 2.19, it can be found that the differences are around 0-0.2 dB for most location points. Same as those previous cases, the locations having significant difference values are corresponding to the locations having extremely small radiations. Hence, although the difference is large in dB unit, the difference is rather small in magnitude actually. The 3D radiation patterns

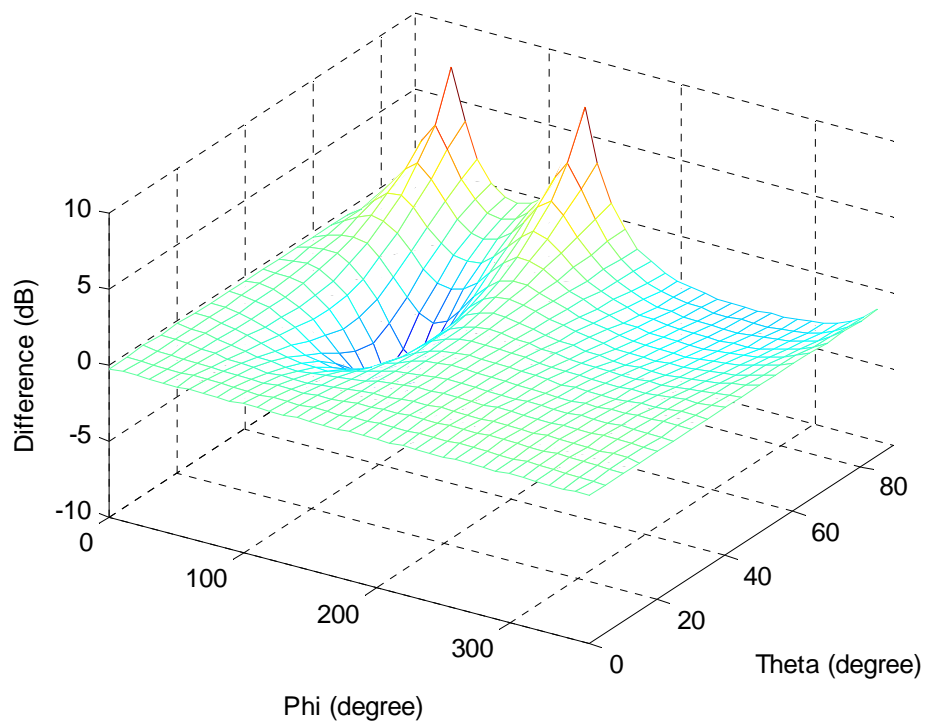
by dyadic Green's function is mimic to the 3D radiation patterns by HFSS simulations no matter how the substrate thickness changes.



(a) The 3D radiation pattern comparison for the transmission line with 20 mil substrate thickness.



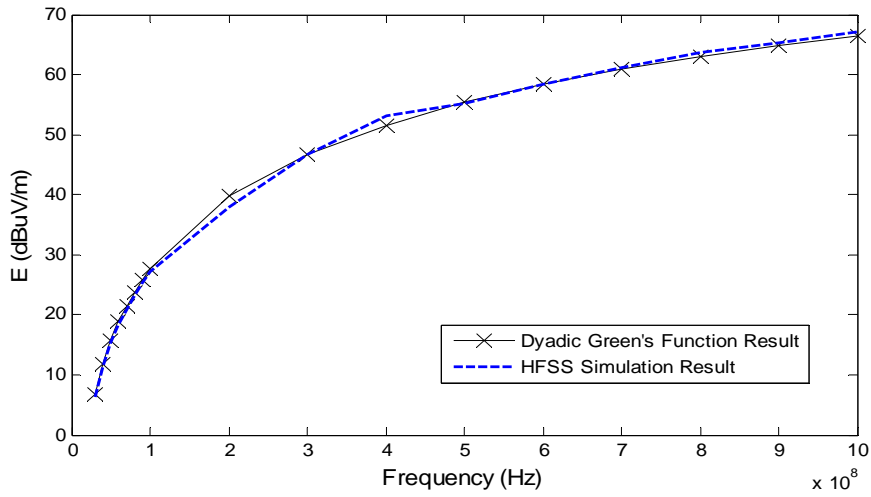
(b) The 3D radiation pattern comparison for the transmission line with 31 mil substrate thickness.



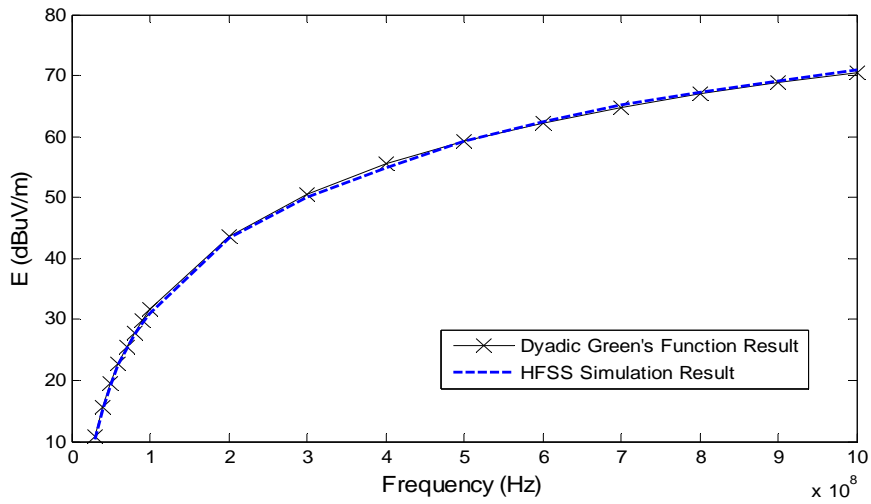
(c) The 3D radiation pattern comparison for the transmission line with 62 mil substrate thickness.

Fig. 2.19: The 3D radiation pattern comparison for the transmission lines with different substrate thicknesses.

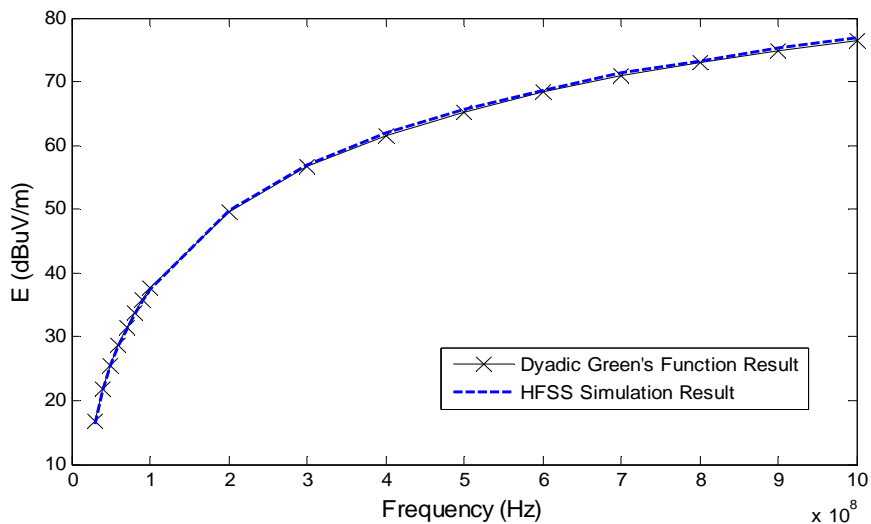
The radiated emission for these microstrip lines with frequency variance (30 MHz to 1 GHz) is plotted in Fig.2.20 when the observation point is 3 meters from the center of the trace at $\theta = 0^\circ$. In Fig.2.18, (a) is the radiated emission for 20 mil substrate thickness, (b) is the radiated emission for 31 mil substrate thickness, (c) is the radiated emission for 62 mil substrate thickness. By observing the plot, it is found that the differences between the modeling results and HFSS simulation results are less than 1 dB. Hence, it can be concluded that the radiated emission modeled by the dyadic Green's function always agrees well with the radiated emission obtained by HFSS full wave simulations for straight transmission lines, no matter the changes of the substrate thickness.



(a) The radiated emission for 20 mil substrate thickness.



(b) The radiated emission for 31 mil substrate thickness.



(c) The radiated emission for 62 mil substrate thickness.

Fig. 2.20: The radiated emissions from the straight microstrip line with different substrate thicknesses.

The radiated emissions from the straight microstrip transmission line with different substrate thicknesses are further compared in Fig. 2.21. From Fig. 2.21, it can be concluded that for the straight transmission lines with same characteristic impedance, electrical length and substrate permittivity, the radiated emission increases with the increase of the substrate thickness. According to Table 2.3, it can be easily found that the W/h ratio for this group of transmission lines is nearly the same, so the difference in radiated emission is not caused by the return current radiation which decided by W/h ratio. However, when the substrate thickness increases, the fringing field increases too. In addition, for keeping the same characteristic impedance, the higher substrate thickness corresponds to the larger width, which provides wider radiating edge for the fringing field.

Therefore, by observing Fig. 2.18 and Fig. 2.21, we can make a recommendation that for reducing the radiated emission, a substrate with higher substrate permittivity and thinner substrate thickness is better. However, in real application, we also need to consider the trade off with the conductor loss and dielectric loss.

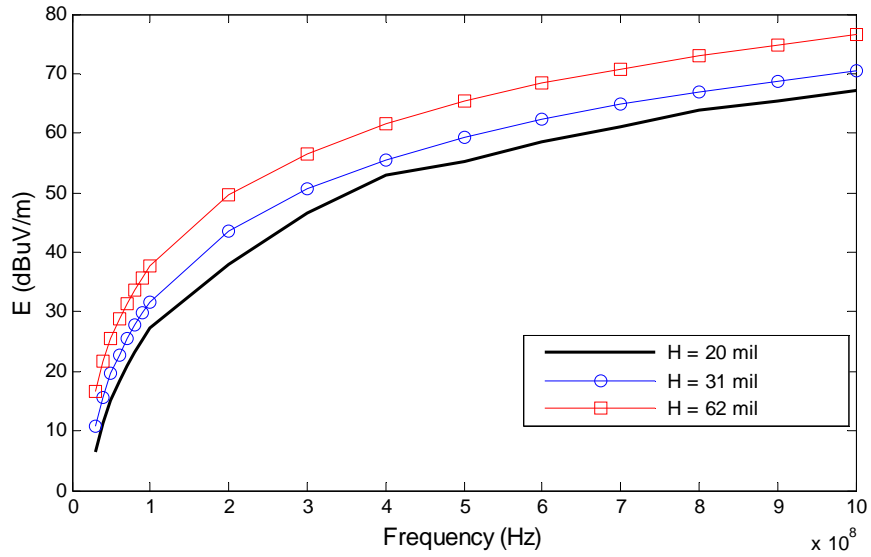


Fig. 2.21: The radiated emission comparisons for the straight microstrip line with different substrate thicknesses.

2.4.3 The application of the modeling method for the transmission lines with different geometries

Besides the straight transmission line, we extend the investigation to L-shaped transmission line and U-shaped transmission line in this section, in order to investigate the influence of transmission line geometry on the accuracy of the radiated emission modeling method.

The L-shaped microstrip line is defined as in Fig. 2.22. The substrate has $\epsilon_r = 2.2$, $\tan\delta = 0.001$, $h = 1.6 \text{ mm} = 62 \text{ mil}$. The trace dimension is $L_1 = L_2 = 75 \text{ mm}$, $W = 4.9 \text{ mm}$ ($Z_0 = 50 \Omega$). The input excitation is set as 1 volt with 50Ω source impedance. The observation point is 3 meter from the center of the trace in the range of $0 \leq \theta \leq \frac{\pi}{2}$, $0 \leq \phi \leq 2\pi$.

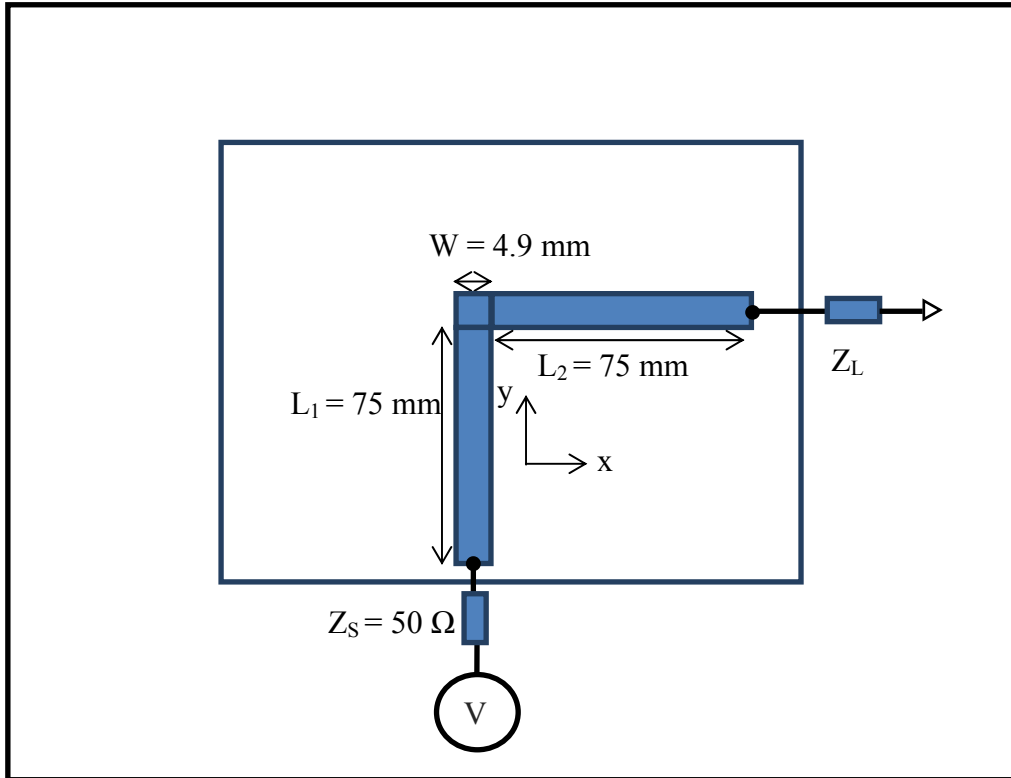


Fig. 2.22: The geometry of the L-shaped microstrip line.

For the L-shaped transmission line, we make the similar 3D radiation pattern comparison between the modeling results by dyadic Green's function and the HFSS simulation results as for the straight transmission line. The result is calculated in dB unit and plotted in Fig. 2.23 for the matched load conditions. It can be found that the difference for most locations for this case is around 0.4-0.6 dB, which is a bit larger than the 0-0.2 dB difference of the straight transmission line with the same material and loading condition. Some locations show large difference around 7 dB. Same as before, these locations are corresponding to the locations having extremely small radiated emission values. Therefore, the difference magnitude is close to the difference at other locations.

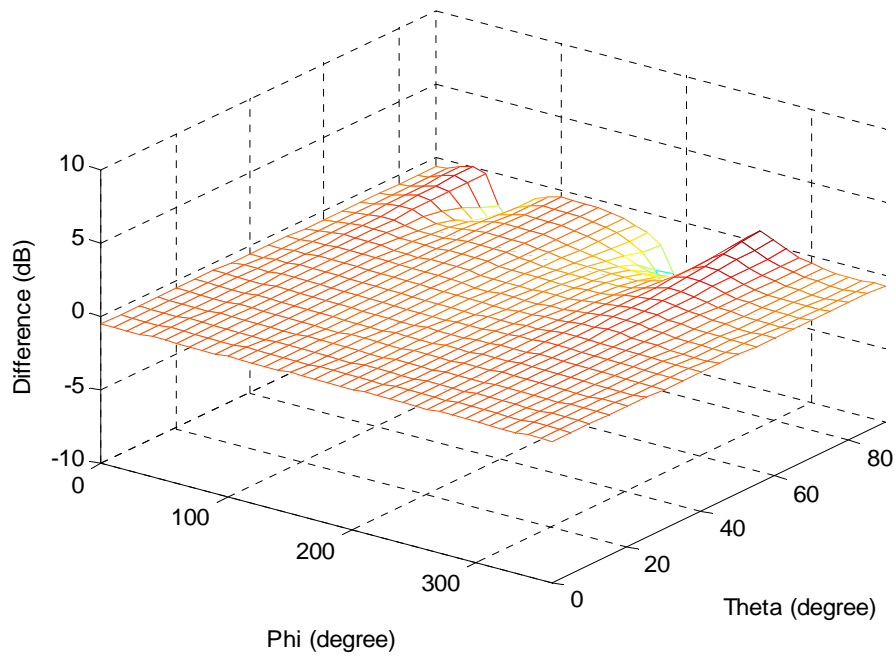


Fig. 2.23: The 3D radiation pattern comparison for the L-shaped microstrip line with matched loading condition.

The radiated emission for the L-shaped microstrip line with frequency variance (30 MHz to 1 GHz) is plotted in Fig.2.24 when the observation point is 3 meters from the center of the trace at $\theta = 0^\circ$. The difference is less than 1 dB over the whole frequency range.

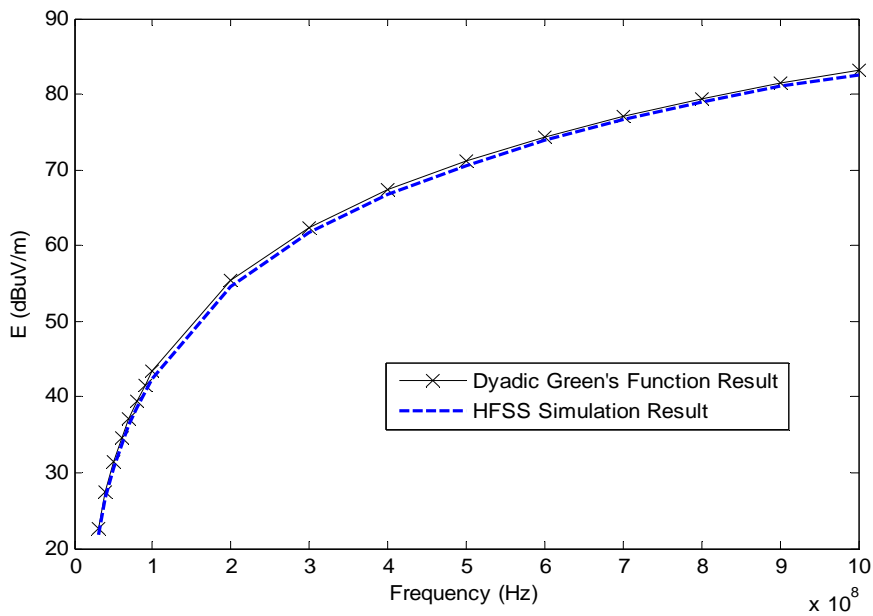


Fig. 2.24: The radiated emissions from the L-shaped microstrip line with matched load condition.

Good agreement can be observed for both 3D radiation pattern comparison and the frequency varied comparison. The comparisons are also made to other load conditions, such as the short end condition, open end condition, positive reactance load condition and negative reactance load condition. Similar to the straight transmission line, the agreement for those conditions are well and even better than the agreement for matched end condition.

The U-shaped microstrip line is defined as in Fig. 2.25. The substrate has $\epsilon_r = 2.2$, $\tan\delta = 0.001$, $h = 1.6 \text{ mm} = 62 \text{ mil}$. The trace dimension is $L_1 = L_2 = L_3 = 50 \text{ mm}$, $W = 4.9 \text{ mm}$ ($Z_0 = 50 \Omega$). The input excitation is set as 1 volt with 50Ω source impedance. The observation point is 3 meter from the center of the trace in the range of $0 \leq \theta \leq \frac{\pi}{2}$, $0 \leq \phi \leq 2\pi$.

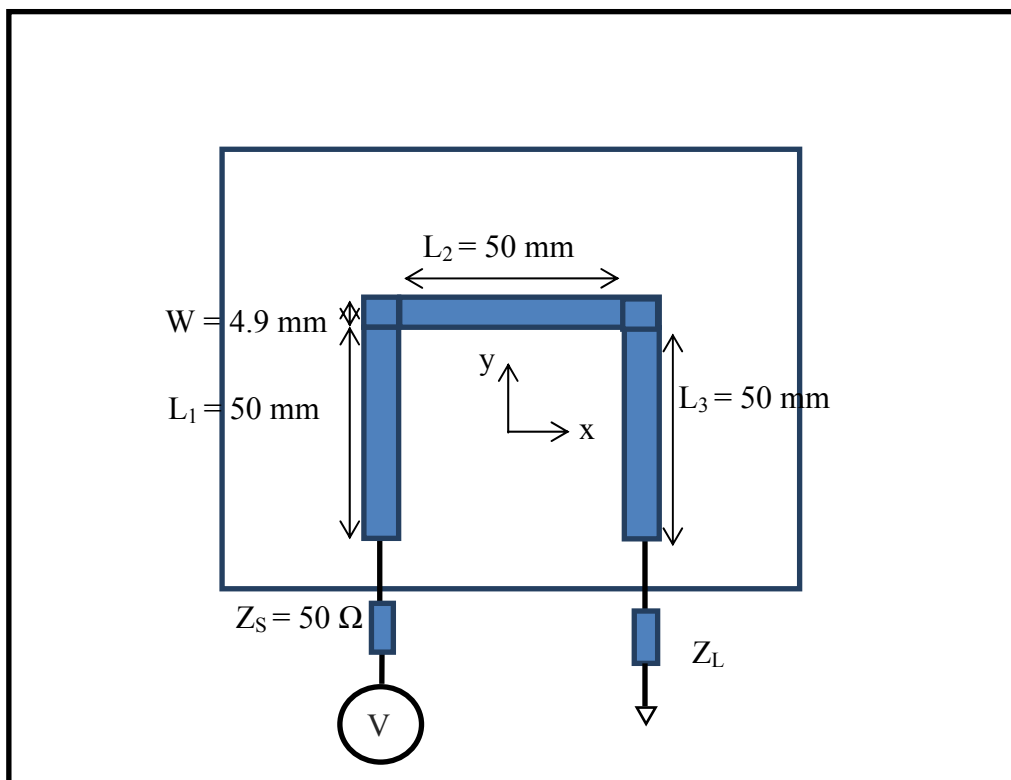


Fig. 2.25: The geometry of the L-shaped microstrip line.

The 3D radiation pattern comparison between the modeling results by dyadic Green's function and the HFSS simulation results as for the U-shaped transmission line is plotted in Fig. 2.26. It can be found that for most of the location points, the two results are agreed well with around 1-3 dB differences. At some locations, the differences are large and sometimes close to 10 dB. Again, those locations are corresponding to the locations where the radiated emission values are extremely small.

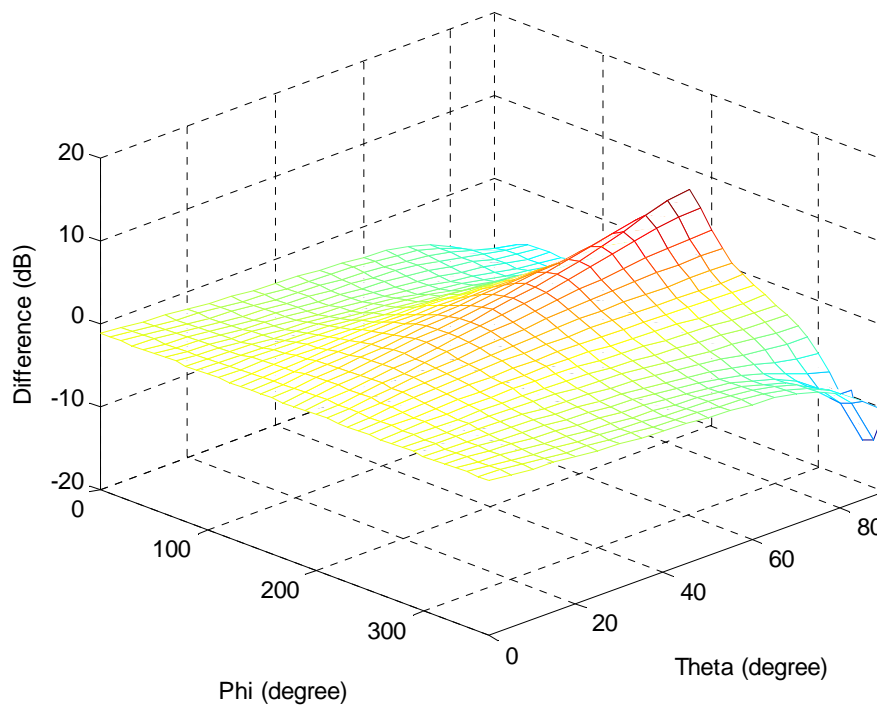


Fig. 2.26: The 3D radiation pattern comparison for the L-shaped microstrip line with matched loading condition.

The radiated emission for the U-shaped microstrip line with frequency variance (30 MHz to 1 GHz) is plotted in Fig.2.24 when the observation point is 3 meters from the center of the trace at $\theta = 0^\circ$. The difference is less than 3 dB over the whole frequency range.

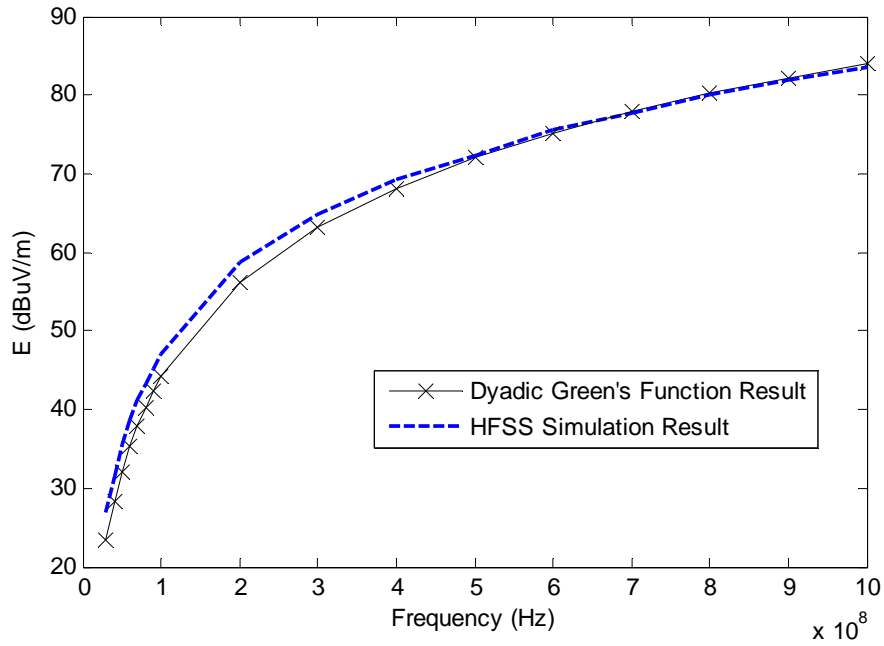


Fig. 2.27: The radiated emissions from the U-shaped microstrip line with matched load condition.

Acceptable agreement can be observed for both 3D radiation pattern comparison and the frequency varied comparison. The comparisons are also made to other load conditions, such as the short end condition, open end condition, positive reactance load condition and negative reactance load condition.

The differences between the modeling results and the HFSS simulation results for the three different geometries can be listed as below.

Table 2.4: The differences between the modeling results and the HFSS simulation results for the three different geometries

TL geometry	The difference from the 3D radiation pattern comparison (dB)	The difference from the frequency varied comparison (dB)
Straight	0 - 0.2	0 - 1
L-shaped	0.4 - 0.6	0 - 1
U-shaped	1 - 3	0 - 3

Please note that the difference from the 3D radiation pattern comparison is obtained by ignoring the locations where the difference value is large in dB but the radiated emission value is extremely small in magnitude.

It can be found that the difference for the L-shaped transmission line is worse than the difference for the straight transmission line and the worst case difference can be up to 3 dB for the U-shaped transmission line. Hence the modeling accuracy of the analytical method for the L-shaped transmission line is a bit influenced by the appearance of the transmission line bends and discontinuities. And this is more significant in the U-shaped transmission line modeling. Therefore, it should be noted that the spurious radiation caused by transmission line bends and discontinuities cannot be very accurately modeled by this method. However, the accuracy is acceptable by considering its advantage in the time and storage saving and complexity reduction.

2.5 Conclusions and recommendations

In this chapter, the radiation characteristics of a single straight transmission line are studied by varying the transmission line parameters, the simulation frequency and the load impedance. The radiated power is significantly affected by the load impedance and increases with decreasing substrate permittivity ϵ_r , increasing frequency f and decreasing W/h ratio. In the following section, the analytical method for electromagnetic radiated emission modeling based on dyadic Green's function is introduced in detail. The method is further adopted to investigate the radiated emissions from the transmission lines with different loading conditions, different substrate

parameters and different geometries. By comparing with the HFSS simulation results, it is found that the accuracy of the method is not influenced by the loading difference, substrate parameter difference and wire length difference. However, the accuracy is limited by the geometry complexity as the spurious radiation caused by transmission line bends and discontinuities cannot be very accurately modeled by this method.

In addition, by comparing the radiated emissions from the transmission lines with different substrate parameters, it is found that for lower radiated emission, the substrate with higher substrate permittivity and thinner substrate thickness is recommended.

In the future work, it might be interesting to expand the radiated emission investigation to more different structures such as parallel straight line, double band, T-junction and so on. On the other hand, since the analytical method is based on the assumption of infinite ground, for the transmission lines on the PCB with small ground size, the method may not be accurate enough. It is a meaningful task to improve the method for more general conditions which including the small ground size condition.

Until now, the investigation is only limited in the circuit with RF input source and fixed load conditions. In the next chapter, we will further explore the radiated emission from the interconnects in digital circuit.

Chapter 3

Modeling electromagnetic radiated emission from high speed interconnects in digital circuits

3.1 Introduction

In this chapter, the IBIS model, which is a widely used digital device model, is introduced in detail. The radiated emission from high speed interconnects in digital circuits can be easily modeled with the use of IBIS models. Hence, the evaluation method is presented and validated by full wave 3D electromagnetic simulation results. Furthermore, this method can be used to investigate the impact of passive SI improvement techniques on the radiated emission from different interconnects in digital circuits. This work can help designers to select the appropriate SI improvement technique taking into account the radiated emission requirements.

3.2 Principle knowledge of IBIS models

3.2.1 The background of IBIS models

IBIS models describe the analog behavior of digital buffers in a behavioral model form using plain ASCII text formatted data. IBIS models are widely used to simulate the impact of interconnects on the performance of digital circuits. Compared with traditional transistor level models, such as SPICE

models, IBIS models have two advantages: a reduction in simulation time and the proprietary information protection. As we know, with the increasing density of digital integrated circuits, traditional transistor level models consume unreasonably long computation time and large CPU storage. In addition, transistor level models tend to reveal the proprietary information, which is undesirable for manufacturers. Thus, the advantages of IBIS models make them widely accepted by designers and manufacturers.

The history of the IBIS model starts from 1990s. Intel created the model for system-level SI analysis as not all the SPICE models for the buffers in the system are available [70]. Intel developed the model by HSPICE originally and then improved it to a tool-independent model format as it realized not all customers can support HSPICE. The IBIS open forum [71] was then funded by Intel and some other electronic design automation (EDA) tool vendors who also showed interest in the model. Presently the IBIS Open Forum is supported by over 35 members who are including the semiconductor vendors, computer vendors, universities and EDA vendors. IBIS 1.0, which is the first version of IBIS specification, was released in 1993 [72]. The newer versions of IBIS specification is kept developed until now with continuous improvements on accuracy and more specified I/O structures. The latest version is IBIS 6.0 [73], but for most manufacturers in industry, IBIS 3.2 [74] or lower version is widely adopted. And the latest IBIS modeling cookbook published on the website of the IBIS Open Forum is for IBIS 4.0 [75]. As a drawback compatible model, all the IBIS models with old versions are guaranteed to compatible with the new versions.

There are usually two ways to generate IBIS models: from SPICE simulation data or from measurement data. Most manufacturers [70], [76], such as Texas Instruments, National Semiconductor and etc., choose to generate IBIS models from SPICE simulation data, as it is difficult to de-embed the package effect and to create process corner data from measurement data. In addition, for a new chip design, the measurement is not available, so the generation of IBIS models from SPICE models is necessary.

The generation of IBIS models from SPICE models can be either done by the S2IBIS software [77], which can convert IBIS models from SPICE models directly or by the different method defined by the manufactures themselves [70], [76]. S2IBIS is written by Java programming language and can be free downloaded from the website of the IBIS Open Forum. By editing a command file, an IBIS model can be fast generated from the corresponding SPICE netlist. The command file consists of a header and a component description. The header described the temperature range and voltage range, all the reference values and the package information. The component description specifies the property of each pin and the model connection to each pin. The working flow of the S2IBIS software is shown in Fig. 3.1 [72]. There are also a number of different versions for S2IBIS. The latest version is s2ibis3, which can generate IBIS 3.2, IBIS 2.1 and IBIS 1.0.

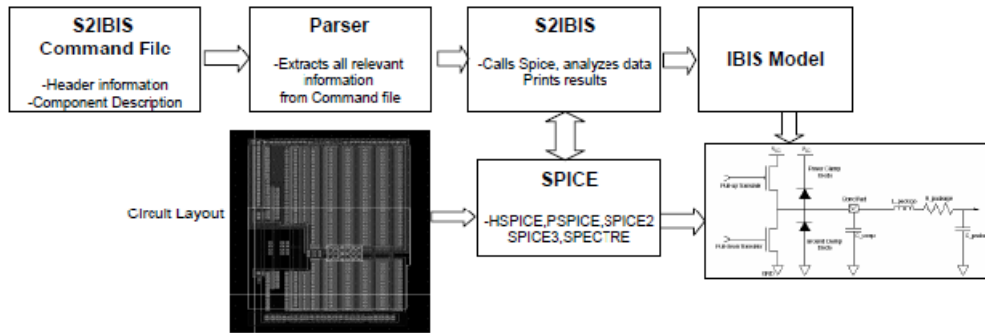


Fig. 3.1: The work flow of the S2IBIS software [72].

As soon as an IBIS model is successfully created, the first step is to do a parser check. The IBIS Open Forum also provides the parser software [71], which is called as “Golden Parser”, to validate the IBIS model file through syntax checking and basic waveform properties. Simulator vendors can purchase the source code while the object code can be downloaded free of charge from the website of the IBIS Open Forum. The latest IBIS parser version is `ibischk6`. It is recommended to use the latest version of the parser even if the IBIS model is an old version.

The application of IBIS models is mainly focused on SI analysis. It can be adopted for SI simulation in the range from single interconnects to complex PCB circuits [78]-[80]. However, when the absence of internal wiring information of IBIS models protects the proprietary information, it also leads to some limitations for IBIS models [81]-[87]. The detailed explanation about these limitations will be given in section 3.3. The most significant influence of these limitations on SI analysis is the overestimation of simultaneous switching noise (SSN). This overestimation severely degrades the accuracy of IBIS models in the SI simulations of digital circuit systems. Hence, a lot of

papers propose the improvement method for this problem [81], [84]-[87]. The main concept is to add some external circuits or macro-models to compensate the missing circuit information. Good SI analysis results can be obtained by those improvement methods. The more accurate SI simulation results can be obtained by a co-simulation approach which combines the IBIS models with the 3D full wave EM models of the interconnects [88]. By making some improvements, the application of IBIS models can be further extended to the prediction of electrostatic discharge failure at system level [89].

In this thesis, the application of IBIS models is further extended to the modeling of electromagnetic radiated emission from interconnects in digital circuits, by making use of the analytical method based on dyadic Green's function. The detailed description of the application will be given in section 3.4 and 3.5.

3.2.2 The description of IBIS models

The contents of an IBIS model include [75]:

- 1) Header section ([File name], [Date], [Source], [Disclaimer], etc.)
- 2) Component section ([Manufacturer], [Package], and [Pin])
- 3) Model and Model_Type section
- 4) I/V curves
- 5) V/t curves
- 6) Additional keywords and sub-parameters ([Test data], [External Model], etc.)

The main function parts of an IBIS model include I/V curves, V/t curves and some package information. The four I/V curves are used to

describe the pull-up information, pull-down information, power clamp information and ground clamp information, respectively. The four V/t curves are used to describe the transient characteristics of the pull-up and pull-down for different output loading. The package information is provided as a set of RLC values for each pin. The basic elements in an IBIS model can be shown as in Fig. 3.2, in which, the left half represents the input buffer while the right half represents the output buffer.

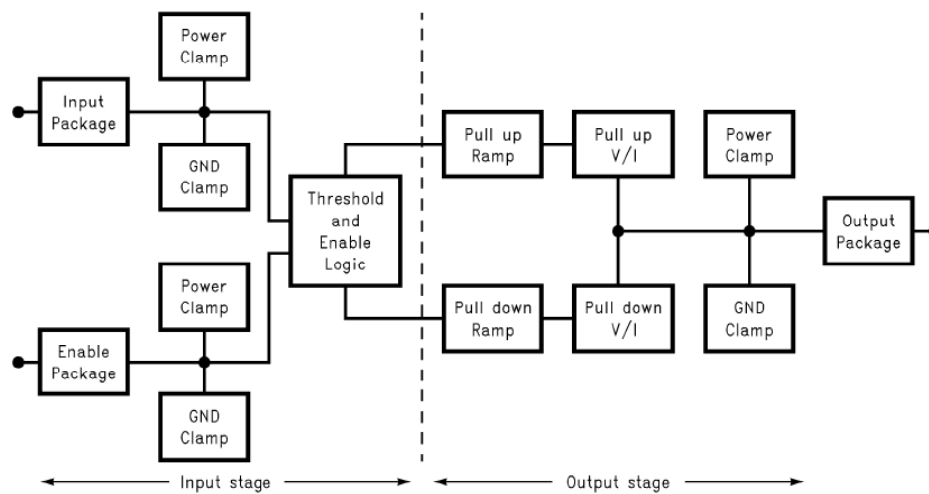


Fig. 3.2: The basic elements in an IBIS model [72].

Each IBIS model contains the data for minimum, typical, and maximum corner conditions [75]. Hence, each I/V and V/t curve contains three sets of data for minimum, typical, and maximum corner conditions. The silicon process limits and the operating environment for the process determine the corner conditions.

Generally, the maximum IV curve represents the largest supply voltage, while the minimum IV curve represents the smallest supply voltage. Typical IV curves give the nominal value which describes the ideal situation. The maximum VT curve represents the fastest process, while the minimum VT

curve represents the slowest process. The typical VT curve is just for ideal case.

In system simulations, we usually use the slow mode to determine the propagation time. And the fast mode is used to estimate overshoot, undershoot and crosstalk. The slow mode is composed of the smallest voltage supply (min. IV data), the slowest process (min. VT data), the highest temperature and the maximum package parasitic values. The fast mode is composed of the largest voltage supply (max. IV data), the fastest process (max. VT data), the lowest temperature and the minimum package parasitic values. However, this is not always the case. Thus, it is recommended to simulate all the corners and observe which one gives the longest propagation time and which one estimates the overshoot, undershoot and crosstalk. In conclusion, the corner situations are very useful in system simulation because they can be used to simulate the worst case results for different considerations.

Generally, there are maximum four I/V curves in IBIS models, which are called [GND_clamp], [Power_clamp], [Pullup], [Pulldown]. [GND_clamp] describes the I-V characteristics when the output is in high impedance state and referenced at ground. [Power_clamp] describes the I-V characteristics when the output is in high impedance state and referenced at V_{dd} . [Pullup] describe the I-V characteristics when the output is in the high logic state and referenced at V_{dd} . [Pulldown] describe the I-V characteristics when the output is in the low logic state and referenced at ground. For most IBIS models (e.g. 3-state model), all the four I/V curves are needed, but for some IBIS models, less than four I/V curves are required. For example, in the input model, there are only [GND_clamp] and [Power_clamp] I/V curves.

There are at least two V/t curves. One for the rising edge transient response is called [Rising Waveform]. And the other for the falling edge transient response is called [Falling Waveform]. It is recommended to have four V/t curves, which means two [Rising Waveform] and two [Falling Waveform]. The two [Rising Waveform] describe the rising edge transient response for different loading conditions. And it is the same for the two [Falling Waveform].

3.2.3 The simulation tools of IBIS models

IBIS models can be simulated as a component of a system in Mentor Graphics, Signal Explorer, SpectraQuest, XTK, HSPICE, ADS, etc. The main simulators used in the thesis are HSPICE and ADS.

In ADS, there is a group of symbols for different kinds of IBIS models, such as input model, output model, 3-state model, open source model and so on. Users can directly drag an IBIS model symbol into the schematic design and import the corresponding IBIS model file to define the symbol. The usage of IBIS models in HSPICE is similar to the usage in ADS, except the circuit is described in netlist.

3.3 The limitation of IBIS models

3.3.1 The natural discrepancies of IBIS models

The generally used IBIS models [75] have two natural deficiencies. Firstly, they model I/O buffers only correctly under the assumption that the power supply rail voltage is constant. This is not a realistic assumption, because, in

reality, the power supply rail and ground rail are not ideal conductors but have parasitic inductances. Hence, there are always voltage fluctuations on these rails caused by the current driven by different circuit blocks. Besides the signal current of the buffer modeled by IBIS models, the total power supply rail current also includes the pre-driver current from the pre-driver circuit, the bypass current through the on-die decoupling and parasitic capacitances, the termination current through the on-die termination resistor network and so on. Therefore, IBIS models cannot accurately model the real power supply rail current [81].

The second deficiency is the absence of gate modulation effect modeling [82], [83]. In the IBIS models, the IV data is obtained under a fixed gate voltage V_{gs} . Thus, the output current in IBIS models is only related to the drain voltage. Yet, in real MOSFET devices, the current has a gate voltage dependency:

$$I_{ds} = \mu C_{ox} \frac{W}{L} \left[(V_{gs} - V_{th}) V_{ds} - \frac{1}{2} V_{ds}^2 \right] \text{ for the linear region} \quad (3.1)$$

$$I_{ds} = \mu C_{ox} \frac{W}{2L} (V_{gs} - V_{th})^2 \text{ for the saturation region} \quad (3.2)$$

In reality, a change in V_{gs} leads to a change in the drain current I_{ds} . This is the gate modulation effect. Fluctuations in the power and ground voltages do occur in reality. These, in turn, produce a change in V_{gs} . Without the model for the gate modulation effect, IBIS models cannot properly capture this behavior. Note that this effect is properly modeled when using SPICE models.

3.3.2 Limitations of the IBIS model in SSN simulation

IBIS models are widely used in SI analysis. However, it is found that there is a limitation of IBIS models in simulating SSN, which is defined as “a voltage glitch induced at power/ground distribution connections within a chip due to switching currents passing through either wire/substrate inductance or package lead inductance associated with power or ground rails” [5].

In order to investigate the IBIS model performance in SSN simulations, the simulation circuit is set up as [82]. Firstly, a buffer consisting of four identical cascading inverting drivers is defined as in Fig.3.3. The example driver used here is NXP’s 74LVC04A. Then, the circuit for SSN simulation is setup with four identical buffers connected in parallel to the same power supply rail and ground rail as shown in Fig. 3.4.

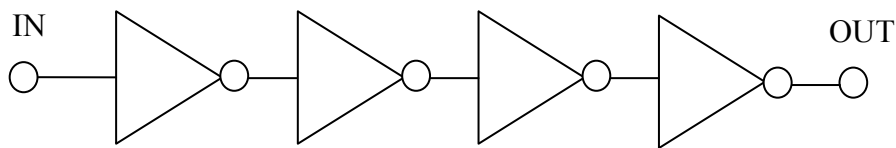


Fig. 3.3: The buffer with four cascaded inverting drivers.

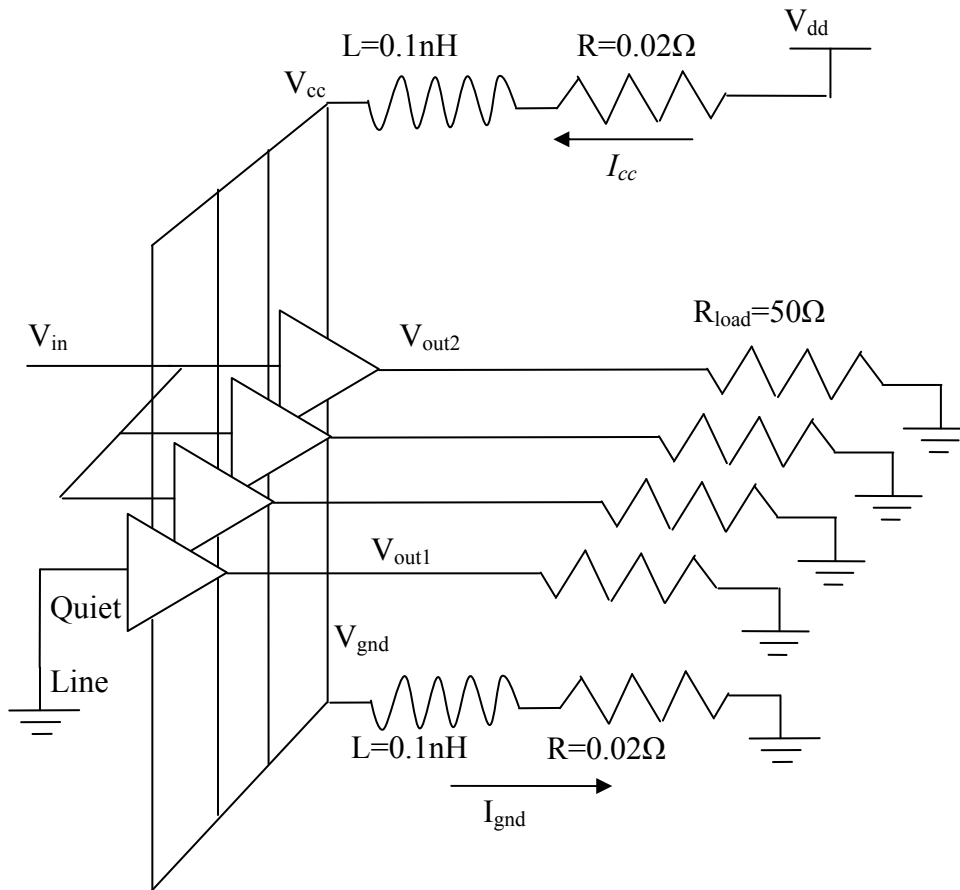


Fig. 3.4: The circuit for SSN simulation with four parallel buffers.

Simple RL circuits are added to model the lossy parasitic inductance of the power and ground rails. All the buffers are connected to 50 Ω terminations. Three of the four buffers are driven by a simultaneous switching input and the fourth buffer input, called the quiet line, is directly connected to ground.

The circuit is simulated with the SPICE model provided by NXP [90] and the IBIS model is generated from the SPICE model using S2IBIS3, which is the software for converting IBIS models to SPICE models. Thus the SPICE simulation results serve as the benchmark to assess the accuracy of the IBIS model.

The output response of the quiet line buffer has significant noise as observed in Fig.3.5. This noise is the SSN due to the other three buffers

switching simultaneously. From Fig. 3.5, it is observed that the IBIS model results overestimate the noise at the quiet line output response. Since the noise represents the SSN, the SSN voltage by the IBIS model at the power supply rail should also be larger than the voltage when using the SPICE model.

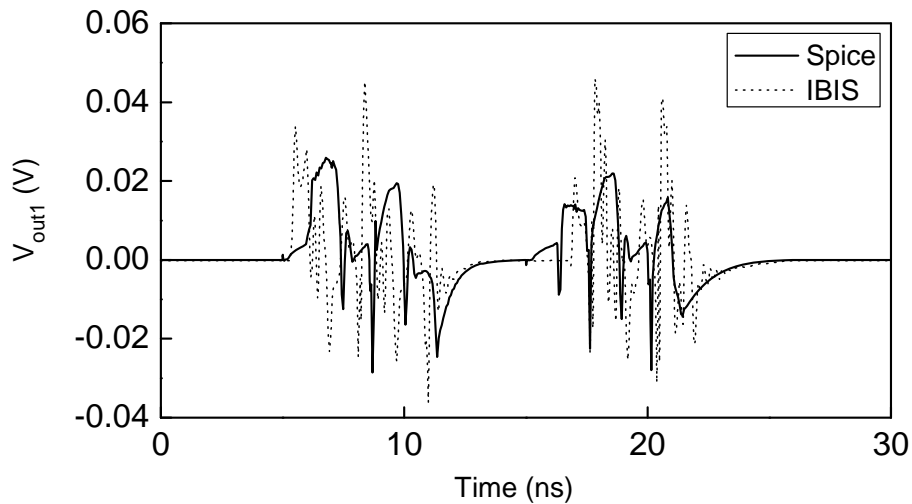


Fig. 3.5: The quiet line buffer output response V_{out1} using the SPICE model (solid line) and the IBIS model (dotted line).

This is confirmed in Fig. 3.6, where the SSN on the power supply rail is shown. Therefore, it is concluded that IBIS models tend to overestimate the simultaneous switching noise compared with SPICE models. This conclusion is in agreement with observations made in [82].

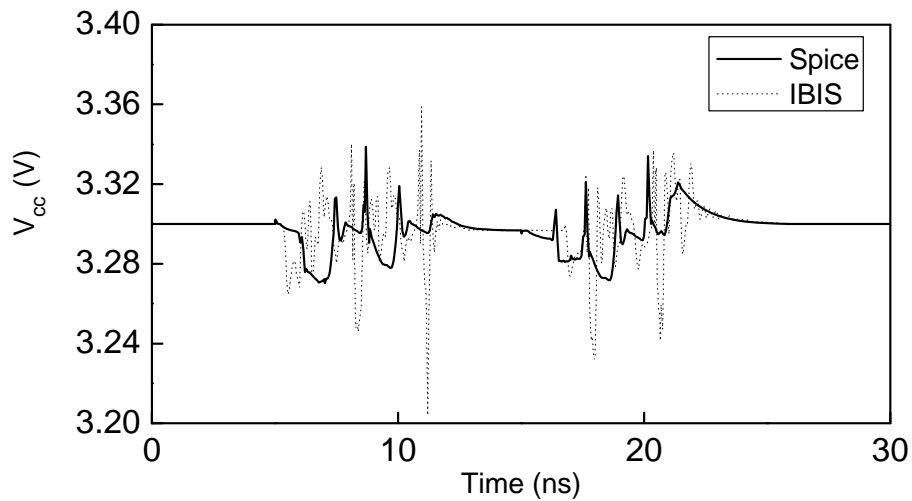


Fig. 3.6: The SSN response at V_{cc} using the SPICE model (solid line) and the IBIS model (dotted line).

3.3.3 Explanation for the IBIS model limitations in SSN simulation

According to the definition of SSN, the SSN at the power supply rail can be calculated as

$$V_{noise} = L \cdot di/dt \quad (3.3)$$

Since the inductance is the same in both models, the overestimation of the voltage when using the IBIS model indicates the current switching rate di/dt is overestimated. Therefore, the current on the supply rail is simulated and is shown in Fig.3.7.

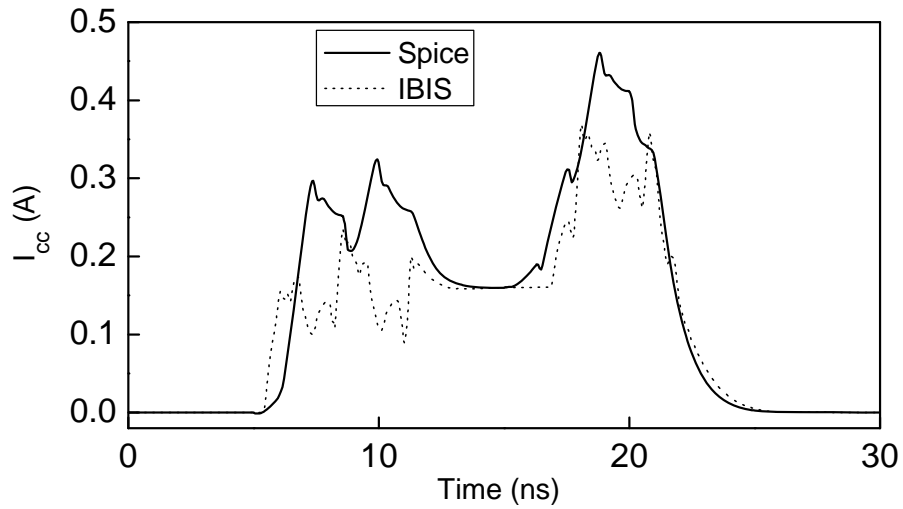


Fig. 3.7: The current at the power rail I_{cc} using the SPICE model (solid line) and the IBIS model (dotted line).

Two important observations are made from this Fig. 3.7. The first observation is that the current when using the IBIS model is smaller than the current when using the SPICE model. This is due to the fact that the pre-driver current, bypass current, termination current and so on are not accounted for when using the IBIS model. The second observation is that the current switching rate dI/dt when using the IBIS model is indeed larger than the current when using the SPICE model, which is more clearly presented in Fig.3.8. It is the same case for the current on the ground rail.

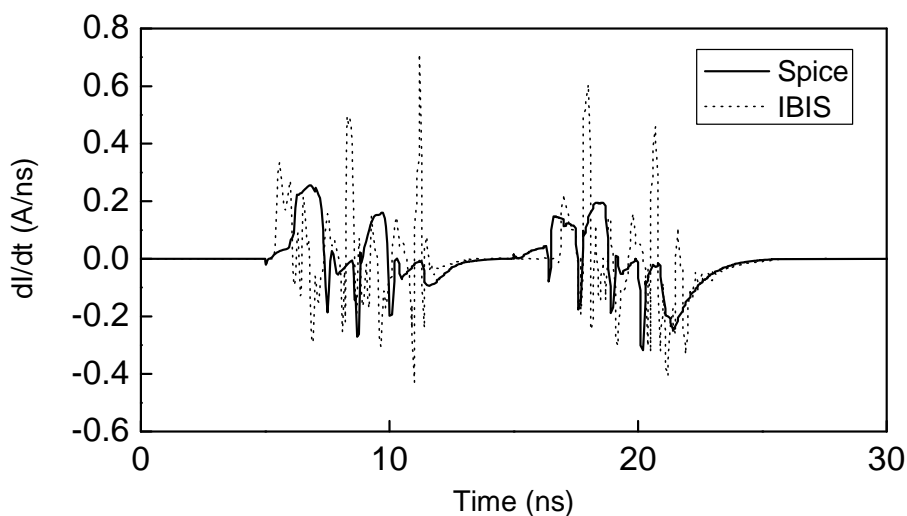


Fig. 3.8: The power rail current switching rate dI/dt using the SPICE model (solid line) and the IBIS model (dotted line).

In order to find the reason for the overestimation of the current switching rate when using IBIS models, a simple output driver is analyzed at the switching edge. We use a CMOS inverter as shown in Fig. 3.9 to represent the output driver and take the rising edge as an example.

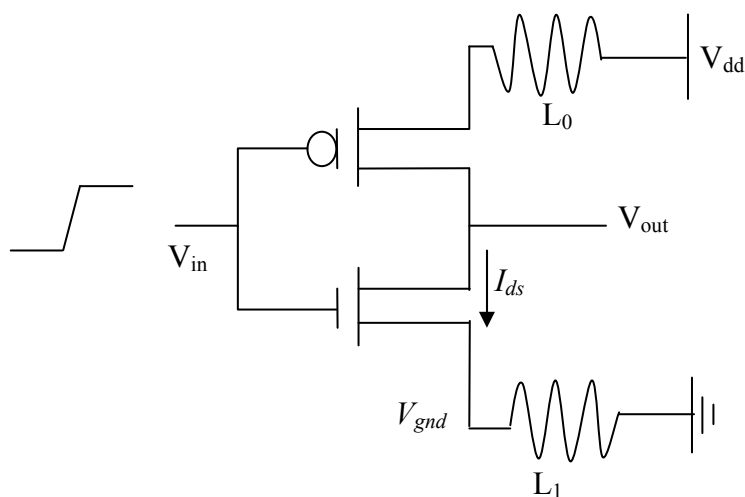


Fig. 3.9: The circuit diagram of the CMOS output driver.

In this analysis we only consider the nMOS transistor effect as the pMOS transistor effect is negligible [84]. At the beginning of the rising edge, the nMOS transistor is in the cut-off region as $V_{gs} < V_{th}$. When the input voltage V_{in} gradually increases from 0 and the drain voltage gradually decreases from 1, the nMOS transistor goes into the saturation region. If V_{in} further increases until the drain voltage is smaller than $V_{in} - V_{th}$, then MOS transistor moves into the linear region and keeps in this region even after V_{in} reaches its steady state.

The nMOS transistor drain current I_{ds} is also the switching current passing through the wire/substrate inductance or package lead (represented by L_1) associated with the ground rails. If the first few ground bounces happen in the saturation region, then

$$I_{ds} = \mu C_{ox} \frac{W}{2L} (V_{gs} - V_{th})^2 = \mu C_{ox} \frac{W}{2L} (V_{in} - V_{gnd} - V_{th})^2 \quad (3.3)$$

$$V_{gnd} = L_1 \cdot \frac{dI_{ds}}{dt} = L_1 \cdot \frac{I_{ds}}{t} \quad (3.4)$$

According to (3.3) and (3.4), it is found that the V_{gnd} and I_{ds} affect each other through V_{gs} . When the increase of I_{ds} leads to the increase of the dI_{ds}/dt , V_{gnd} is also increased according to (3.4), so V_{gs} is reduced and then I_{ds} is reduced according to (3.3), which is opposite to its initial trend. Hence, this effect is a negative feedback effect [85]. IBIS models do not incorporate this negative feedback effect, because it is assumed that V_{gs} is constant and equal to the maximum drain voltage V_{dd} . Hence, for the IBIS models, the current always is

$$I_{ds} = \mu C_{ox} \frac{W}{2L} (V_{gs} - V_{th})^2 = \mu C_{ox} \frac{W}{2L} (V_{dd} - V_{th})^2 \quad (3.5)$$

According to (3.5), it is obvious that dI_{ds}/dt in the IBIS models is larger than in the SPICE models.

If the first few ground bounces happen in the linear region, the current is given by

$$\begin{aligned} I_{ds} &= \mu C_{ox} \frac{W}{L} \left[(V_{gs} - V_{th}) V_{ds} - \frac{1}{2} V_{ds}^2 \right] \\ &= \mu C_{ox} \frac{W}{L} \left[(V_{in} - V_{gnd} - V_{th}) V_{ds} - \frac{1}{2} V_{ds}^2 \right] \end{aligned} \quad (3.6)$$

$$V_{gnd} = L_1 \cdot \frac{dI_{ds}}{dt} = L_1 \cdot \frac{I_{ds}}{t} \quad (3.7)$$

In this case, the negative feedback effect still exists but does not apply in IBIS models for the same reason as in the saturation region. The switching current in IBIS models is given by

$$\begin{aligned} I_{ds} &= \mu C_{ox} \frac{W}{L} \left[(V_{gs} - V_{th}) V_{ds} - \frac{1}{2} V_{ds}^2 \right] \\ &= \mu C_{ox} \frac{W}{L} \left[(V_{ad} - V_{th}) V_{ds} - \frac{1}{2} V_{ds}^2 \right] \end{aligned} \quad (3.8)$$

which is still larger than the current in reality and causes the overestimation of dI_{ds}/dt in the IBIS models. Therefore, IBIS models always overestimate the current switching rate due to the absence of a gate modulation effect model, irrespective of the fact that the first few ground bounces happen in the saturation region or the linear region. Similarly, the same conclusion applies to the falling edge.

3.3.4 Improvement method for IBIS models in SSN simulation

There are mainly two kinds of improvement methods for the IBIS models in SSN simulations. One is to add external circuits to the current IBIS models [81], [62], [86], the other is to modify the current IBIS models themselves by adding more SSN information [91]. The external circuits in the first kind of improvement methods are always developed from the SSN simulation results

of the SPICE model circuits, so this kind of methods is not practical. The second kind of improvement methods does not have this problem. It is suggested by the committee of IBIS open forum and leads to the updating of the new version of IBIS models [91], but this new standard has not been adopted by the industry yet.

The second kind of improvement methods include BIRD95 [92] and BIRD98 [93]. BIRD 95 suggests adding the I/t tables, which describe the current waveforms at rising and falling edge from the power reference terminal of the buffer in IBIS models. BIRD 98 suggests adding the I/V tables, which provide the effective current of the pullup/pulldown structures of a buffer by a function of the voltage on the pullup/pulldown reference nodes. From section 3.3, we know that the inaccurate SSN simulation results when using IBIS models is caused by the absence of the gate modulation effect, which affects the simulation results by two ways. The first one is that the absence of gate modulation effect leads to the inaccurate modeling of the voltage fluctuations at the power supply rail and ground rail. The second one is that even if those fluctuation voltages are modeled accurately, the absence of gate modulation effect makes the output current be invariant with the change of the gate voltage. BIRD 95 focuses on the improvement on the first one, while BIRD 98 focuses on the improvement of the second one. BIRD 98 only works on the basis of BIRD 95.

In order to validate the effectiveness of BIRD 95, we add external current sources to the existing IBIS model circuit to mimic the effects of BIRD 95. The power supply rail and ground rail currents are extracted from the previous SSN simulation circuits when using SPICE models. Then two

current sources, which represent the differences between the SPICE model and the IBIS model for the power supply rail and ground rail, respectively, are added to the previous SSN simulation circuits when using the present IBIS models, as shown in Fig. 3.10.

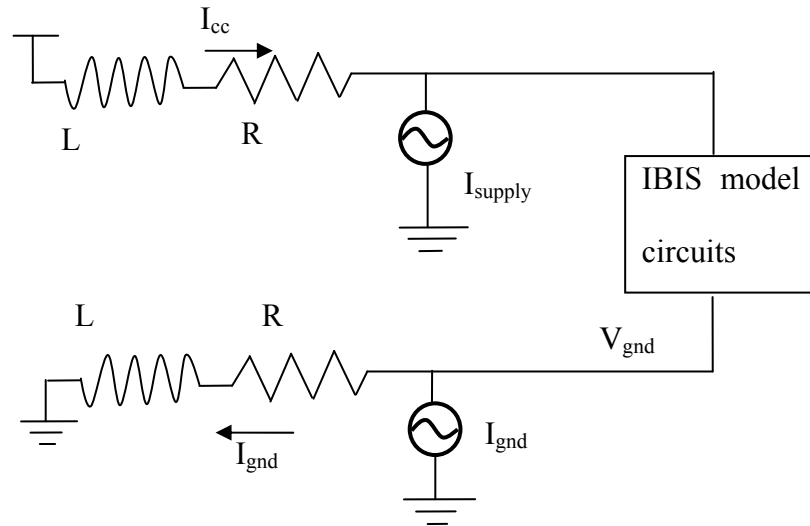


Fig. 3.10: The diagram of the improved IBIS model circuits

The comparison of the V_{cc} difference between the SPICE model and the improved IBIS model with the V_{cc} difference between the SPICE model and the original IBIS model is shown in Fig. 3.11. It can be observed that the improved IBIS model circuit can model the V_{cc} fluctuation much better than the original IBIS model circuit compared to the simulation result using the SPICE model. The comparison for the V_{gnd} difference is also simulated and similar to the result shown in Fig. 3.11. As the modeling of the fluctuation of the gate voltage is improved, the quiet line buffer output response V_{out1} should also be improved using the improved IBIS model. The comparison of the V_{out1} difference between the SPICE model and the improved IBIS model with the V_{out1} difference between the SPICE model and the original IBIS model is shown in Fig.3.12. It is indeed observed that the accuracy of the quiet line

buffer output response is improved significantly using the improved IBIS model. Thus, by providing enough information for the current at the power reference terminal, the modeling of SSN performance in IBIS models can be significantly improved.

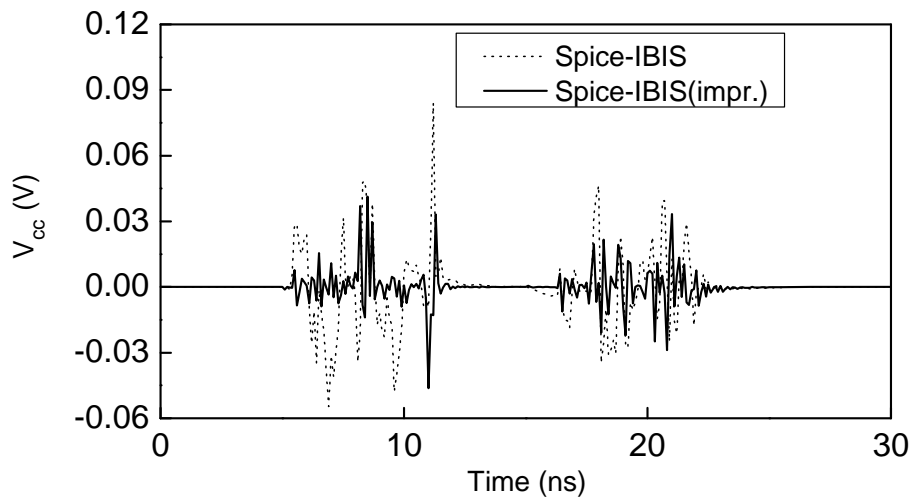


Fig. 3.11: The V_{cc} difference between the SPICE model and the original IBIS model (dotted line) and the V_{cc} difference between the SPICE model and the improved IBIS model (solid line).

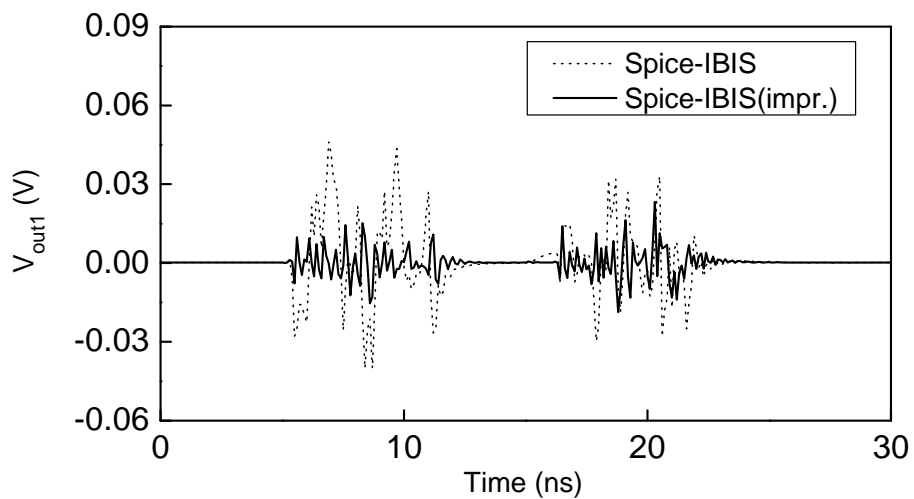


Fig. 3.12: The V_{out1} difference between the SPICE model and the original IBIS model (dotted line) and the V_{out1} difference between the SPICE model and the improved IBIS model (solid line).

3.4 The radiated emission from interconnects with a non-linear dynamic load

3.4.1 The radiated emission model

In chapter 2, we have introduced the model which can be used to model the radiated emission from interconnects by using the distributed current along the interconnects, when voltage source and load impedance are fixed at a certain frequency. In this section, we still focus on the radiated emission of the straight interconnect and L-shaped interconnect but the interconnects are loaded by digital devices, i.e., in a non-linear dynamic load condition. Hence, we use the same model to derive the distributed current by IBIS models with the use of a circuit simulator.

In the first step, we build a digital circuit in the circuit simulator. The digital devices are modeled by the corresponding IBIS models and the interconnects are modeled by transmission line models. Then the voltage and current at the two-port of the investigated interconnects are simulated. The distributed current along the transmission lines can be derived from the two-port voltages and currents, which are Fourier transformed from the time domain. After that, the radiated emission can be modeled using the dyadic Green's function with the distributed current along the interconnects as introduced in chapter 2.

3.4.2 The radiated emission from the interconnects loaded with a digital receiver

The circuit structure is shown in Fig. 3.13. The source in all cases is a $50\ \Omega$ pulse generator at 8 MHz, 50% duty cycle with $t_r = t_f = 2\ \text{ns}$, $V_{high} = 5\ \text{V}$, $V_{low} = 0\ \text{V}$, as shown in Fig. 3.14. The straight line as shown in Fig. 3.13 has $L = 150\ \text{mm}$ and $W = 4.9\ \text{mm}$. Its characteristic impedance is around $50\ \Omega$. The L-shaped line shown in Fig. 3.13 is defined as $L_1 = L_2 = 75\ \text{mm}$ and $W = 4.9\ \text{mm}$. The substrate material are the same for both lines which have $\epsilon_r = 2.2$, $\tan\delta = 0.001$ and $h = 1.6\ \text{mm}$. The dynamic load is the Texas Instruments buffer 74LVC125A and the corresponding IBIS model is provided by the manufacturer. The measurement is 3 meters from the center of the interconnects in the direction of $\theta = 0$.

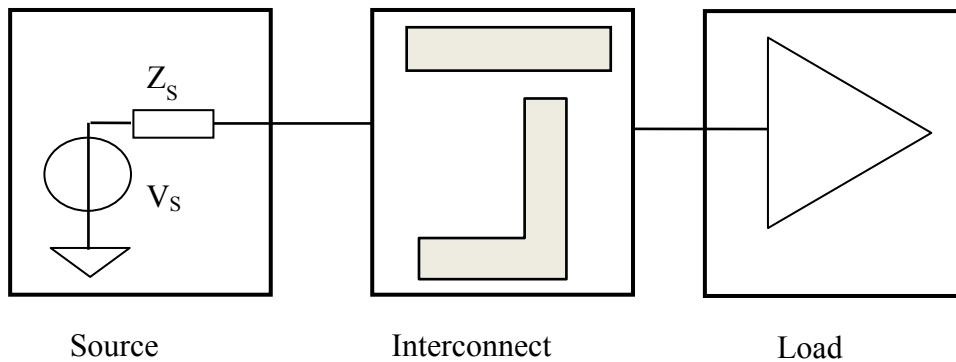


Fig. 3.13: The circuit diagram for dynamic load condition.

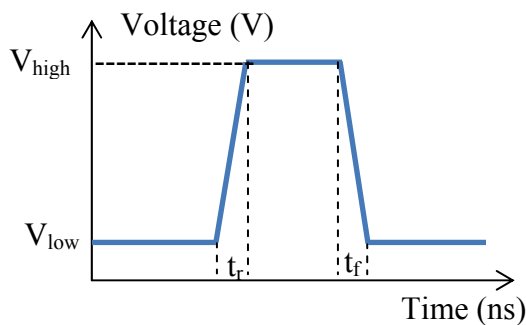


Fig. 3.14: The circuit diagram for dynamic load condition.

IBIS models only work in time domain, but the two-port voltage and current values used for deriving the distributed current along the interconnects are in frequency domain. To solve the problem, one method is to build a frequency dependent impedance model to represent the load. The impedance value is obtained from Fourier transforming the voltage and current value at the input of the receiver in transient simulation. Then the two-port voltage and current values in frequency domain can be obtained by the AC simulation (frequency domain simulation) in which the trace is fed by the frequency spectrum of the original pulse and the load is represented by frequency dependent impedance. The frequency-dependent load profile for the investigated circuit is plotted as in Fig. 3.15. It should be noted that this frequency dependent impedance is only corresponding to the specific input pulse. If the input pulse is changed, the frequency dependent impedance will also change.

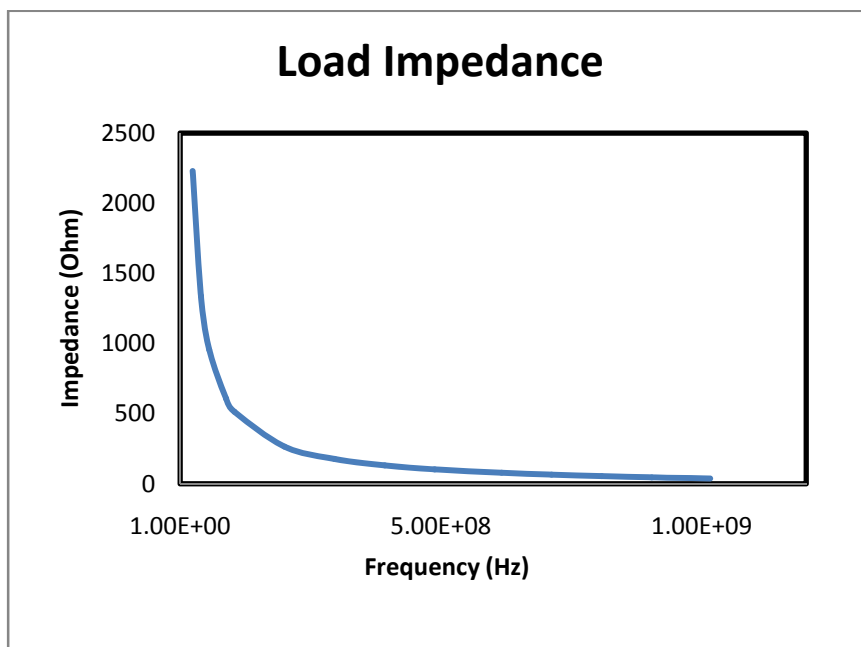


Fig. 3.15: The frequency-dependent load profile.

The other method is to do the transient simulation to obtain all the two-port voltage and current values for the interconnects and then to Fourier transform all the results.

Three kinds of radiated emission results are compared for each interconnect. The first one is the radiated emission evaluation result derived by the first method. The second one is the radiated emission evaluation result derived by the second method. The third result is the full wave simulation result from ANSYS HFSS as a benchmark.

The radiated emission from the straight interconnect under dynamic loading condition is shown in Fig. 3.16. The radiated emission evaluation results of the two different methods are totally the same. The HFSS simulation result is close to the two evaluation results.

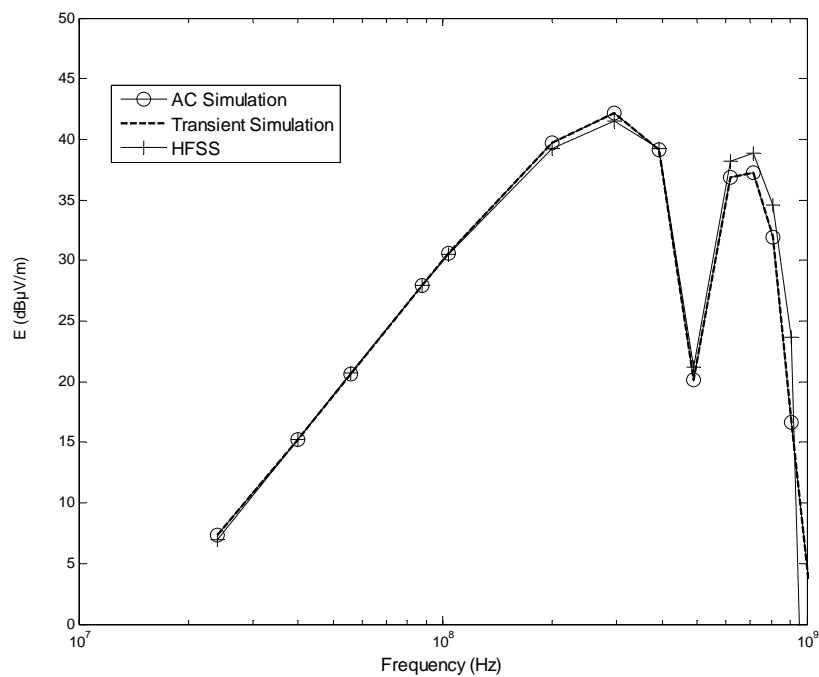


Fig. 3.16: The radiated emission from the straight interconnect under dynamic loading condition.

The radiated emission from the L-shaped interconnect under dynamic loading condition is shown in Fig. 3.17. The radiated emission evaluation results by the two different methods are totally the same. The HFSS simulation result is also close to the two evaluation results.

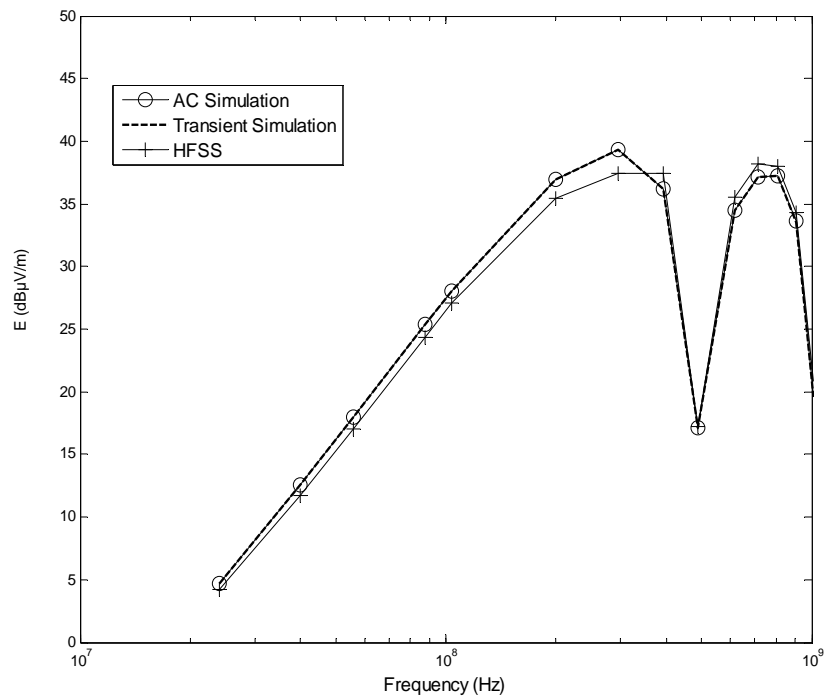


Fig. 3.17: The radiated emission from the L-shaped interconnect under dynamic loading condition.

The good agreement between the two evaluation results confirms the effectiveness of the frequency dependent impedance. The consistence between the full wave simulation result and the two evaluation results confirms the accuracy of the evaluation method. The method can also be applied to other digital device models such as SPICE models. The procedure is exactly the same.

3.5 The influence of various SI improvement techniques on the radiated emission

3.5.1 Motivation

With the increasing speed and density of digital integrated circuits, the radiated emission of digital circuits also increases, which makes the SI no longer the only important issue for desired functional performance. In addition, EMC standards also put constraints on the radiated emission for commercial devices. Hence, it is critical to know at the design stage the impact of SI improvement techniques on the radiated emission of digital circuits, although it is often ignored in conventional design flows because of the separation of SI design and radiated emission analysis.

In the last section, we have introduced the method to model the radiated emission from the interconnects in dynamic load conditions using IBIS models. Here, we use the same method to extend the investigation to the interconnects placed between two dynamic digital devices, i.e., a dynamic source and a dynamic load. In addition, we investigate the influence of various SI improvement techniques on the radiated emission from interconnects. Therefore, SI designers can estimate the change in the radiated emission from the interconnects as soon as they apply common passive SI improvements on digital circuits and modify the improvement design by considering the influence on the radiated emission. The interconnects investigated here include both straight and L-shaped interconnects. The digital devices are modeled using the corresponding IBIS models provided by the manufacturers.

3.5.2 SI improvement techniques

The schematic diagram for the PCB interconnects without any SI improvement technique is shown in Fig. 3.18(a). The impact of the following four passive SI improvement techniques [94], [95] on the radiated emission is analyzed:

- 1) Series termination technique, shown in Fig. 3.18(b)
- 2) Parallel termination technique, shown in Fig. 3.18(c)
- 3) Thévenin termination technique, shown in Fig. 3.18(d)
- 4) AC termination technique, shown in Fig. 3.18(e)

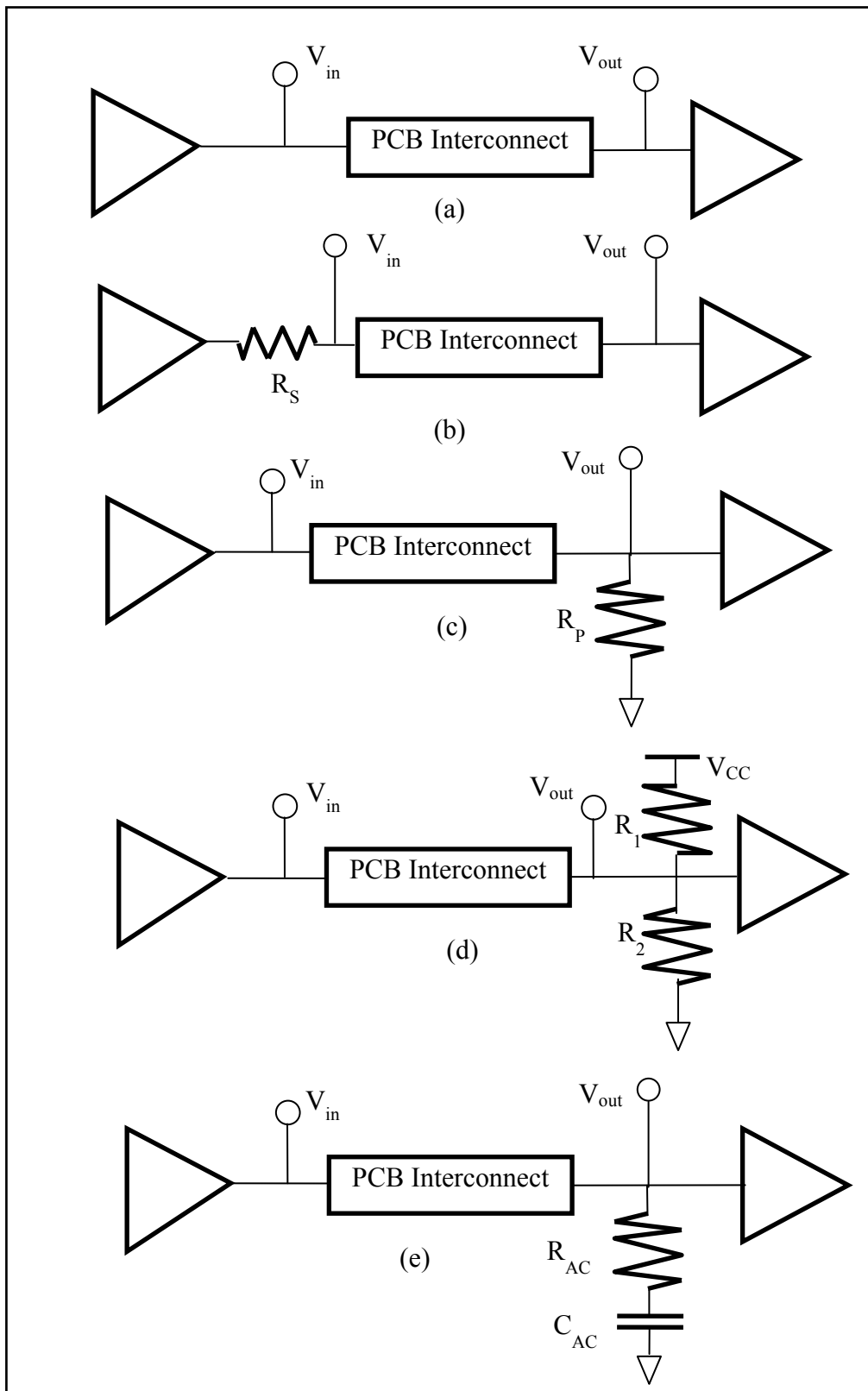


Fig. 3.18: The schematic diagram for the original circuit and the four SI improvement techniques considered (a) no SI improvement technique; (b) series termination technique; (c) parallel termination technique; (d) Thévenin termination technique; (e) AC termination technique.

The series termination technique adds a resistor R_S in series with the source while the total impedance before the interconnect equals the characteristic impedance Z_0 of the interconnect. Since the output impedance of the driver varies with the change of the driver's logic state, the value of R_S is calculated as the difference between Z_0 and the average value of the driver output impedance [96]. The steady state current for the series termination is zero as the input impedance of the receiver is very high at the steady state. Thus, the power dissipation in steady state is also zero. Compared with other passive SI improvement techniques, the series termination technique has the limitation that it can only apply to the case when the driver output impedance is less than the characteristic impedance. And this technique reduces the response speed [5].

The parallel termination technique [94] is the simplest and only requires a resistor $R_P = Z_0$ in parallel with the load. However, its steady state current is nonzero when the digital signal is in the high state, thus there is power consumption in the high state when using this technique.

The Thévenin termination technique [94] adds two resistors, R_1 and R_2 , in parallel with the load. The parallel combination of R_1 and R_2 equals to Z_0 . The two resistors serve as pull up and pull down resistors respectively. Although it has power consumption in the steady state, it reduces driver burden by supplying additional current to the load.

The AC termination technique [94] is to add a resistor R_{AC} and a capacitor C_{AC} in parallel with the load. As in the parallel termination, the R_{AC} value is matched to Z_0 to eliminate reflections. C_{AC} is used to reduce the steady state power consumption.

3.5.3 Radiated emission of SI improvement techniques

The radiated emission of the straight and L-shaped interconnects between digital devices with different passive SI improvement techniques is investigated using the method introduced in section 3.4. The first step is to derive the distributed current along the interconnects from the two-port voltages and currents extracted from circuit simulations with a commercial circuit simulator. Since the driver and the receiver are modeled by IBIS models which only worked in time domain, all the two-port voltage and current values for the interconnects are obtained by transient simulation and then Fourier transformed to frequency domain. Then the second step is to model the total radiated emission by dyadic Green's function with the distributed current values.

The straight interconnect has $L = 150$ mm and $W = 4.9$ mm and the characteristic impedance is around 50Ω . The L-shaped interconnect has the same width W and $L_1 = L_2 = 75$ mm. The substrate parameters for both interconnects are $\epsilon_r = 2.2$, $\tan\delta = 0.001$ and $h = 1.6$ mm. Two SN74LVC125A buffers from Texas Instruments are used as the driver and the receiver respectively. The driver is stimulated by a pulse input of 8 MHz, 50% duty cycle, $t_r = t_f = 2$ ns, $V_{high} = 5$ V, $V_{low} = 0$ V.

A. Radiated Emission from Straight Interconnect

The maximum radiated emission at $r = 3$ m for the original circuit and the improved SI circuits in case of the straight interconnect is shown in Fig. 3.19. It is noted that the maximum radiated emission from this geometry is generally around the z-axis ($\theta = 0^\circ$). From Fig.3.19, it is found that only the series

termination circuit always has lower radiated emission than the original circuit. The other three SI improved circuits have higher radiated emission than the original circuit from 0.03 to 0.2 GHz. They have much lower radiated emission in the range of 0.2-0.5 GHz and 0.8-1 GHz.

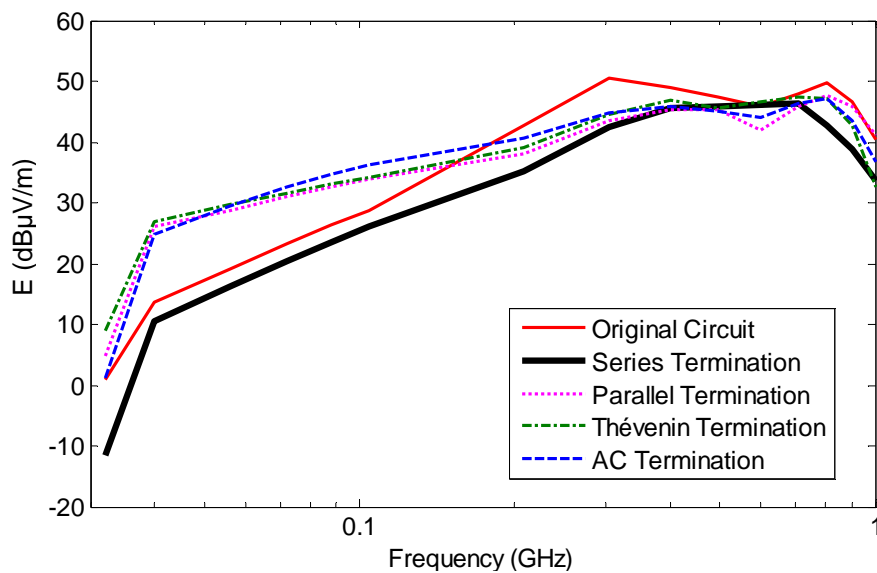


Fig. 3.19: The maximum radiated emission from the straight interconnect

Since the radiated emission is directly related to the current in the interconnect, the comparison result for the current at the output of the straight interconnect (I_{out}) can be used to explain the radiated emission. The comparison of the current in the original circuit and the current in the improved SI circuits in time domain is shown in Fig. 3.20. It is found that by comparing with the current of the original circuit, (1) the series termination circuit has smaller current peaks and has zero DC current at the same time; (2) the parallel termination circuit has smaller current peaks but a significant DC current in the steady state; (3) the Thévenin termination circuit also has smaller current peaks but significant DC current in the steady state; (4) the AC termination circuit has zero DC current, but the current peaks are much larger.

Hence, among the four different SI improvement termination circuits, only the series termination circuit has smaller current peak and has zero DC current at the same time by comparing with the original circuit. All the currents along the straight interconnect show similar phenomena.

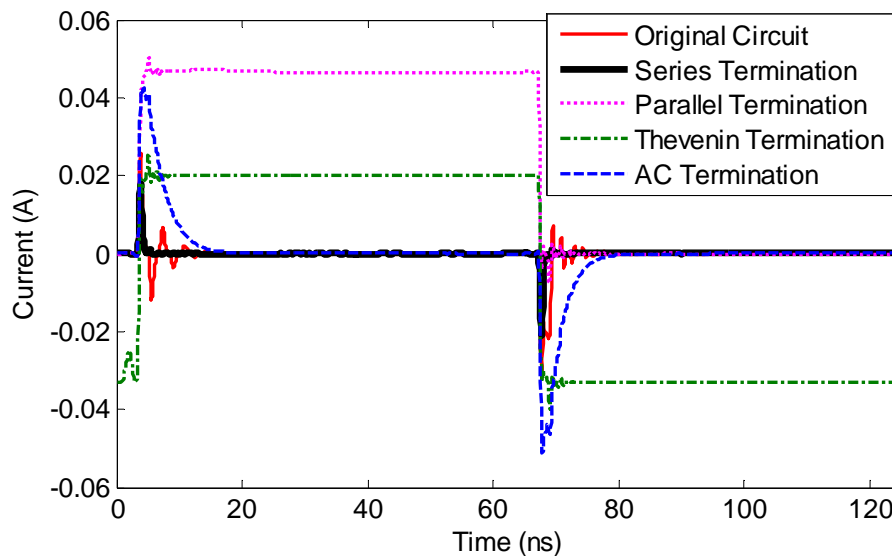


Fig. 3.20: Time domain current for the straight interconnect

The Fourier transformed time domain current at the same position is shown in Fig. 3.21. It is found that only the series termination circuit always has a smaller current than the original circuit current. The other three improved circuits have much larger currents than the original circuit for frequencies below 0.2 GHz and have smaller currents only for the ranges of 0.2-0.5 GHz and 0.8-1 GHz. This can be easily explained by the former observation made from Fig. 3.20.

By comparing Fig. 3.21 with Fig. 3.19, we can conclude:

- (1) For the original circuit without any SI improvement techniques, the low current at low frequencies corresponds to low radiated emission at low frequencies.

- (2) For the circuit with series termination technique, the low current at low frequencies also corresponds to the low radiated emission at low frequencies.
- (3) For the circuit with parallel termination technique, the high current at low frequencies corresponds to the high radiated emission at low frequencies.
- (4) For the circuit with Thévenin termination technique, the high current at low frequencies corresponds to the high radiated emission at low frequencies.
- (5) For the circuit with AC termination technique, the high current at low frequencies corresponds to the high radiated emission at low frequencies.

Hence, the trends of the radiated emission totally follow the trends of the current.

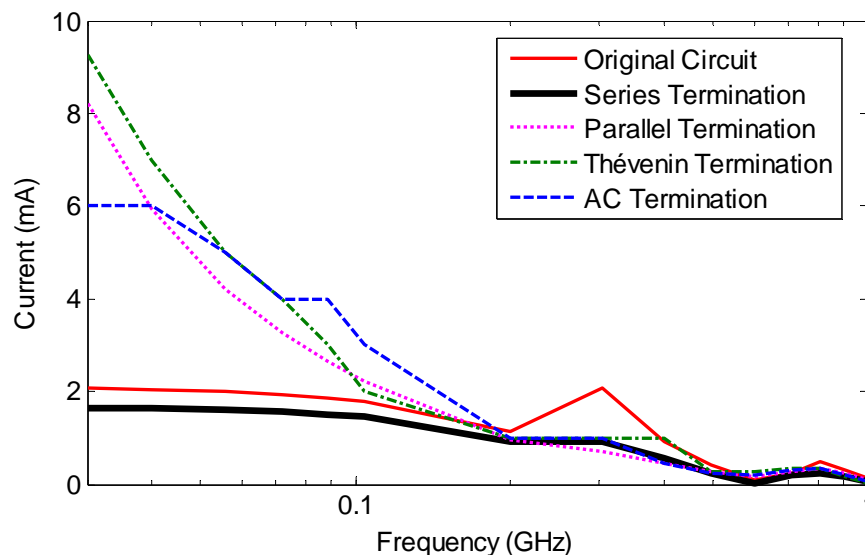


Fig. 3.21: Frequency domain current for the straight interconnect

B. Radiated Emission from L-shaped Interconnect

The maximum radiated emission at $r = 3$ m of the original circuit and the improved SI circuits in case of the L-shaped interconnect is shown in Fig. 3.22. For this geometry, the maximum radiated emission is still generally around the z-axis ($\theta = 0^\circ$). From Fig. 3.22, it is found that although the radiated emission envelope for the L-shaped interconnect is different from the radiated emission envelope for the straight interconnect in the frequency above 0.7 GHz, the series termination circuit is still the only improved circuit which has smaller radiated emission than the original circuit over the whole frequency range. Similarly, the other three SI improved circuits have more radiated emission than the original circuit in the range of 0.03-0.2 GHz, although they have less radiated emission in the ranges of 0.2-0.5 GHz and 0.8-1 GHz.

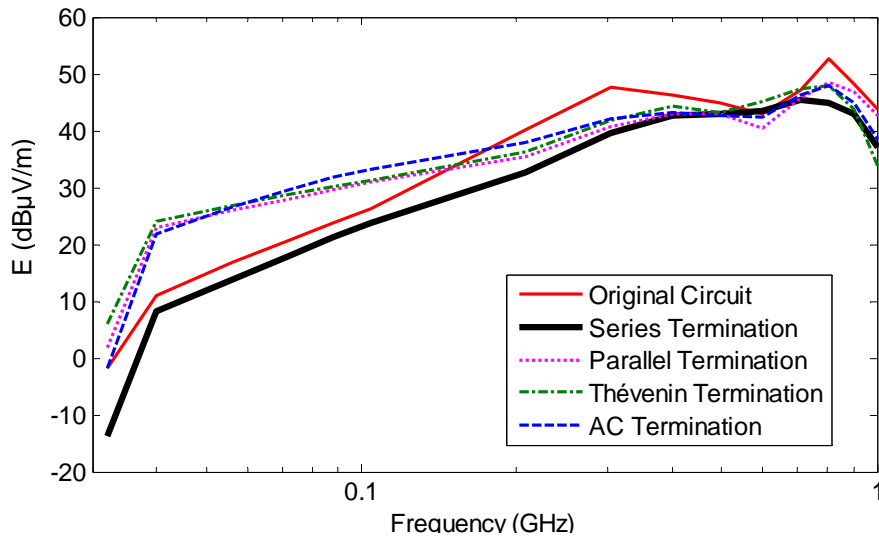


Fig. 3.22: The maximum radiated emission from the L-shaped interconnect

The current comparisons for the L-shaped interconnect in the time domain and frequency domain show the same phenomena as the straight interconnect in Fig. 3.20 and Fig. 3.21. And the trends for the radiated

emission still follow the trends of the current. The impacts of these SI improvement techniques on radiated emission from both two kinds of interconnect structures are consistent with their impact on the distributed currents, respectively.

Since SI design and radiated emission analysis are usually separated in conventional design flows, the impact of SI improvement techniques on the radiated emission is usually ignored. The method presented here can be easily adopted to model the radiated emission from the interconnects between dynamic digital devices when these SI improvements or even more complicated improvements are applied. As mentioned in section 3.4, this method can be applied not only with IBIS models but also SPICE models. The further validation of the method is presented by the comparisons of the results of this method with the measurement results and the results of the method using SPICE model in chapter 4.

3.6 Conclusions and recommendations

In this chapter, the IBIS model, which is a behavioral model for digital devices, is introduced and investigated. By adopting the analytical method introduced in chapter 3 with the IBIS model, the electromagnetic radiated emission from interconnects in digital circuits can be modeled. Section 3.3 presents the modeling results for the interconnects between a non-linear dynamic load by comparing with the HFSS simulation results, which is used as a benchmark. The good agreement proves the accuracy of the method.

In the following section, the method is extended to the electromagnetic radiated emission modeling for the interconnects between a dynamic source and a dynamic load. By implementing different passive SI improvement techniques on the original circuit, we can evaluate the influence of various SI improvement techniques on the radiated emission from the straight and L-shaped interconnects by adopting the method. The discussed termination techniques are series termination technique, parallel termination technique, Thévenin termination technique and AC termination technique. According to the modeling results of the radiated emission, series termination technique performs better radiation suppression than others. However, it is just the conclusions obtained from the two specified cases. For more general conclusion, more different transmission line structures need to be investigated. In addition, series termination technique has more limitations by comparing with others, such as the long response time and the application condition that the characteristic impedance must be larger than the source impedance. Hence, some active SI improvements techniques need to be explored for better solution.

In conclusion, this section demonstrates a fast method for designers to easily predict the radiated emission level as soon as they made any SI improvements. The measurement validation for the method implemented in this section will be further presented in chapter 4.

Chapter 4

Measurement of radiated emission measurement from high speed interconnects

4.1 Introduction

4.1.1 The test site for radiated emission measurement

According to the CISPR standards [2], [97], the measurement of electromagnetic radiated emission should be operated at an open area test site (OATS). In an OATS, the radiated emission from the device under test (DUT) can spread over the open area without any reflection, i.e., no reflective objects inside the area. A perfect infinite ground plane is also required for OATS.

However, the requirement for a standard OATS is hard to achieve. Hence, practically, the radiated emission is measured in an anechoic chamber in this thesis. The details of the measurement setup is given in section 4.2, and the measurement results are given in section 4.3 and 4.4, which are compared with the results of our radiated emission models.

4.1.2 The antenna for radiated emission measurement

The antennas used for radiated emission measurement must be broadband antennas. The common used antennas include biconical antennas, log periodic dipole arrays, bicon/log hybrid antennas and broadband ridged

waveguide horn antennas. The typical frequency range for biconical antenna is from 20 MHz to 300 MHz, while for log periodic dipole arrays and bicon/log hybrid antennas, the frequency range can be extended to several Gigahertz. For frequency up to 40 GHz, broadband ridged waveguide horn antennas are the typical choice.

Besides those common used antenna parameters such as gain, and directivity, antenna factor (AF) is a critical term for radiated emission measurement but seldom used in other applications. As a parameter describing the relationship between the incident electric field and the voltage on the 50 Ω load, the expression of AF is:

$$AF = E/V \quad (4.1)$$

where E represents the incident electric field and V represents the voltage with 50 Ω load. The unit of AF is dB m⁻¹ or 1/m.

In radiated emission measurement, antennas are used as receivers. Thus, AF is used to determine the radiated electric field from the voltage measured by the testing instruments such as spectrum analyzer. Higher AF [98] value is desired as it indicates the more sensitive receiver. AFs are usually obtained from the antenna manufacturers or some specified calibration labs.

4.2 The setup for the radiated emission measurement

The measurement setup in the chamber is shown in Fig. 4.1, in which the DUT is placed on a 1.2 m high holder inside the chamber. The DUT is mounted on the shielding box at the side facing the receive antenna. The antenna is 4.5 meters from the center of the DUT in the direction of $\theta = 0$.

The chamber has the dimension of 700 x 400 x 250 cm. The absorber used in the chamber is ZXB-500. Each absorber contains 64 pyramids and each pyramid has the dimensions of 500 x 500 mm base size and 500 mm height. The uncertainty level of the chamber is ± 2 dB for 30 MHz-200 MHz and ± 1 dB for 200 MHz-1 GHz. The noise floor of the chamber is around -80 dBm.

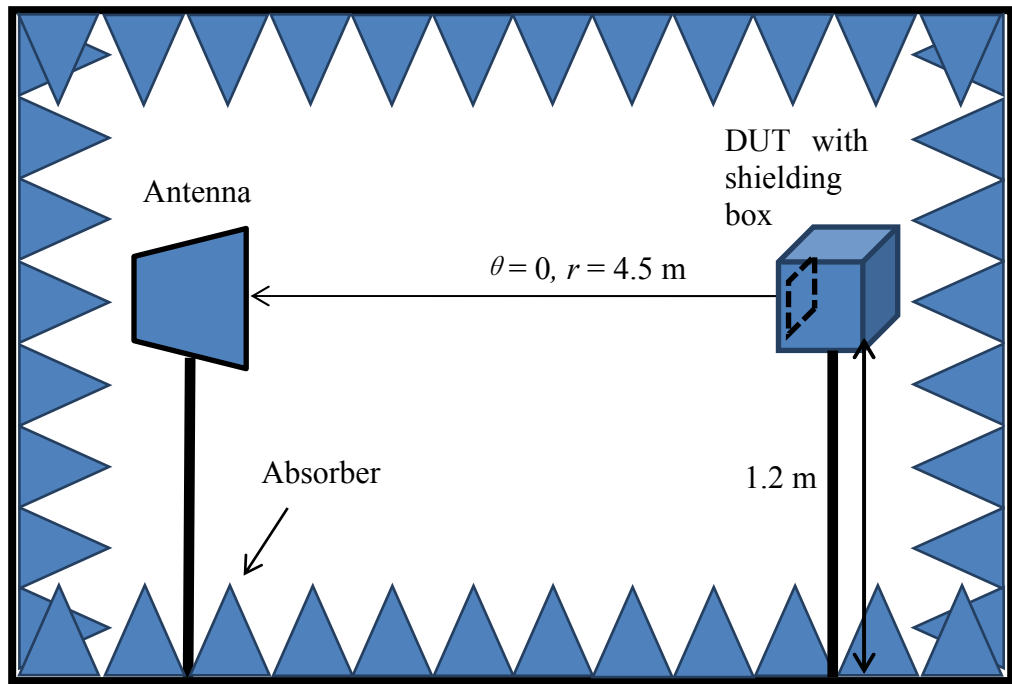


Fig. 4.1: The measurement setup in the chamber.

Since the radiated emission level is low, the broadband receive antenna is connected to the spectrum analyzer through a pre-amplifier as shown in Fig. 4.2. An Anritsu MS2651B spectrum analyzer from 9 kHz to 3 GHz is used. The choice of the receive antenna and the pre-amplifier depends on the signal frequency. For the signal in the range of 30 MHz-1 GHz, the Aaronia AG BicoLOG 30100E bicon hybrid antenna and the HP 8447D pre-amplifier are used. For the signal in the range of 1GHz-18GHz, the Rohde&Schwarz HF907 horn antenna and the HP 8449B pre-amplifier are used. The antenna factor and

cable losses are taken into account in the measurements as shown in Table 4.1.

The antenna factor is provided by the manufacturer of the antenna.

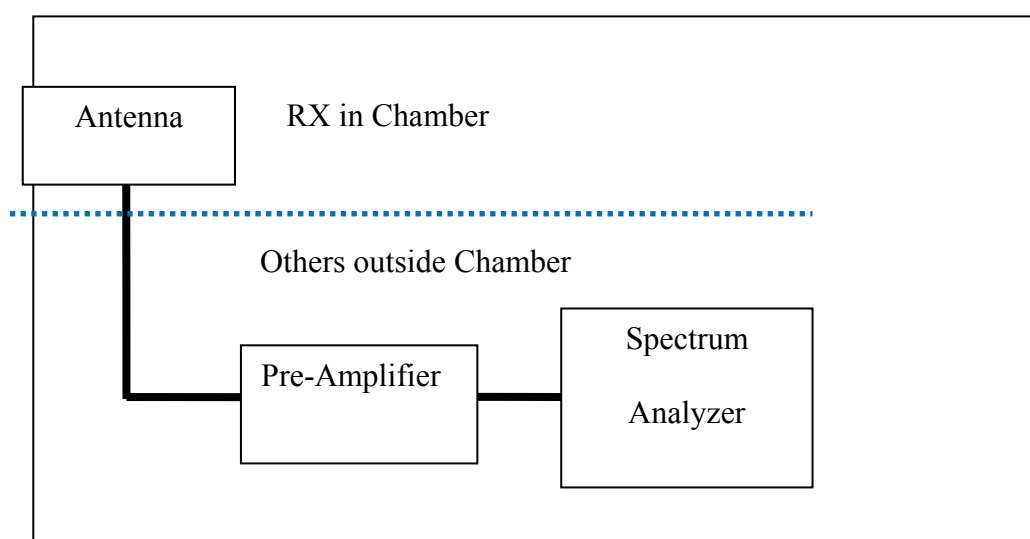


Fig. 4.2: The instrument connection for the measurement

Table 4.1: The antenna factor and cable loss

Frequency	AF (dB m ⁻¹)	Cable Loss at the receiver end (dB)	Cable Loss at the transmitter end (dB)
2.00E+8	17.2	1.51	1.48
3.00E+8	20.5	1.87	1.82
4.00E+8	23.4	2.17	2.12
5.00E+8	25.5	2.45	2.39
6.00E+8	27.7	2.69	2.63
7.00E+8	29.8	2.92	2.86
8.00E+8	31.7	3.14	3.07
9.00E+8	32.8	3.34	3.26
1.00E+9	24.4	3.53	3.46
1.20E+9	24.5	3.90	3.82
1.40E+9	25.45	4.25	4.16
1.60E+9	26.48	4.57	4.48
1.80E+9	27.22	4.88	4.78
2.00E+9	28.72	5.17	5.07

The far field radiated emission results are obtained by the following procedure:

1. Read the power P_0 from the spectrum analyzer in the unit of dBm.
2. Calculate the received power $P_{\text{rec}} = P_0 - \text{Gain}$, in which ‘Gain’ is the gain of the pre-amplifier.
3. Derive the received voltage V_{rec} from P_{rec} .
4. Derive the radiated emission by $E = V_{\text{rec}} + \text{AF} + \text{Cable Loss}$

4.3 Measurement of radiated emission from interconnects in simple RF circuits

The measurement starts with the straight interconnect placed between an RF signal source and a fixed load. The first investigated straight line is fabricated on FR4. The substrate has $\epsilon_r = 4.4$, $\tan\delta = 0.018$, $h = 1.524 \text{ mm} = 60\text{mil}$. The trace dimension is $L = 82 \text{ mm}$, $W = 3.04 \text{ mm}$, which makes the characteristic impedance of the interconnect around 50Ω . The input signal power is 0 dBm over the frequency range of 200-1400 MHz and the load is 50Ω . The lowest frequency limit is chosen as the lowest frequency of the chamber is around 200 MHz. The highest frequency limit is chosen according to the frequency limitation of the quasi-TEM mode, which is the pre-assumption of the modeling method.

Two radiated emission results are shown in Fig. 4.3 for this interconnect. The dotted line is the measurement result. The solid line is the modeling result obtained using the analytical method. The detailed procedure

to obtain the modeling result is the same with the procedure introduced in section 2.3.2, which includes:

1. Build a digital circuit in the circuit simulator. (digital device → IBIS model, interconnect→two-port TL model)
2. Simulate the voltages and currents at the two ports of the investigated interconnects.
3. Derive the distributed current from the simulated two-port voltage and current.
4. Use dyadic Green's function to model the radiated emission by using the distributed current derived in step 3.

From Fig. 4.3, good agreement is observed between the measurement result and modeling result. The difference between the two results is kept less than 4dB.

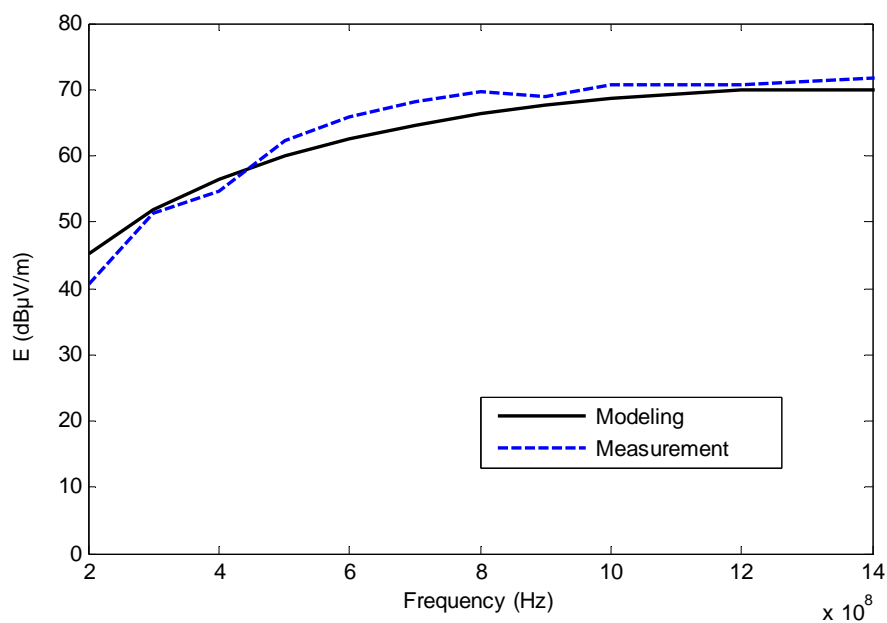


Fig. 4.3: The radiated emission from the straight interconnect made on FR4.

By using the same excitation and loading condition setting, another straight line fabricated on RT5880 is also measured. The substrate has $\epsilon_r = 2.2$, $\tan\delta = 0.001$, $h = 0.787$ mm = 31 mil. The trace dimensions are $L = 110$ mm, $W = 2.4$ mm, which makes the characteristic impedance of the interconnect around 50Ω . The modeling result and the measurement result are shown in Fig. 4.4. Good agreement can be observed between the two results. The difference between the two results is less than 4dB.

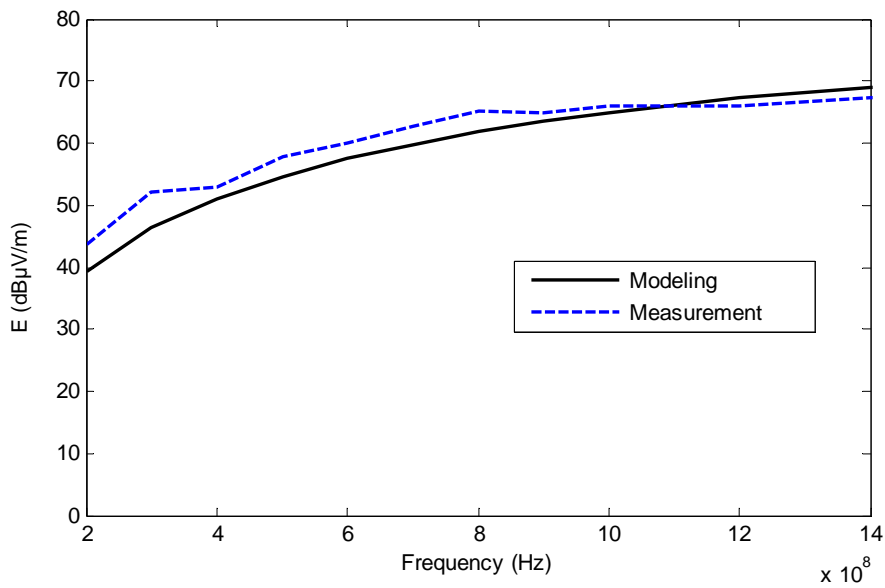
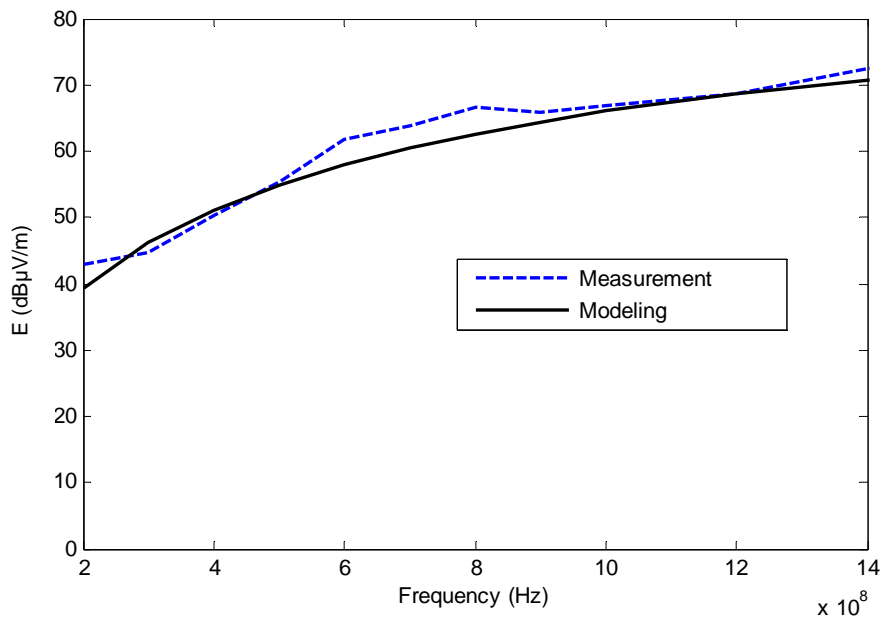


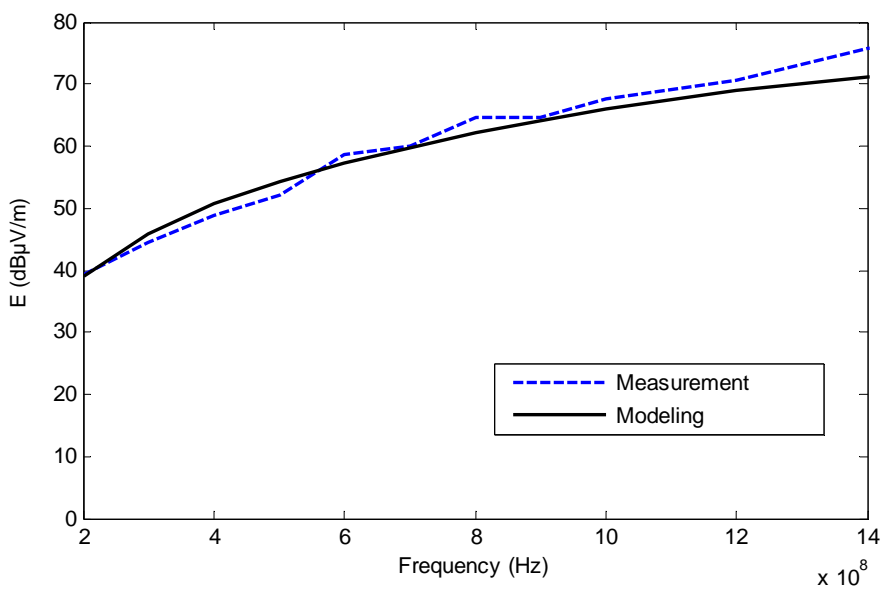
Fig. 4.4: The radiated emission from the straight interconnect made on RT5880.

The measurement is also extended to L-shaped interconnects. The L-shaped interconnects are also fabricated on FR4 and RT5880 respectively. For the L-shaped interconnect fabricated on FR4, the dimensions are $L_x = L_y = 41$ mm, $W = 3.04$ mm. L_x and L_y represent the length of the two branches which are along the x -axis and y -axis respectively. The radiated emissions from the L-shaped interconnect made on FR4 is shown in Fig. 4.5. The radiated emission contributed by the branch along the x -axis is plotted in Fig. 4.5(a),

while the radiated emission contributed by the branch along the y -axis is plotted in Fig. 4.5(b). Good agreement is observed between the modeling results and the measurement results for both branches. The difference is kept less than 5dB.



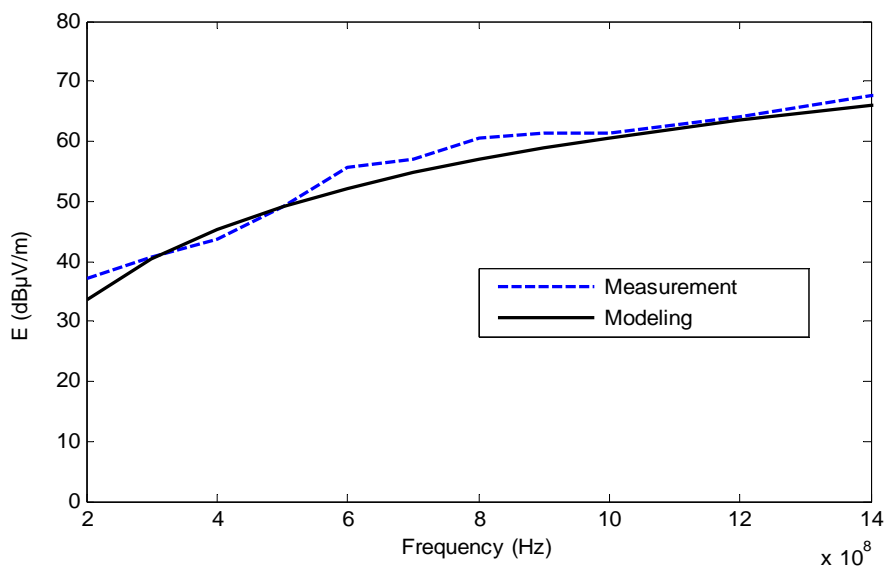
(a)



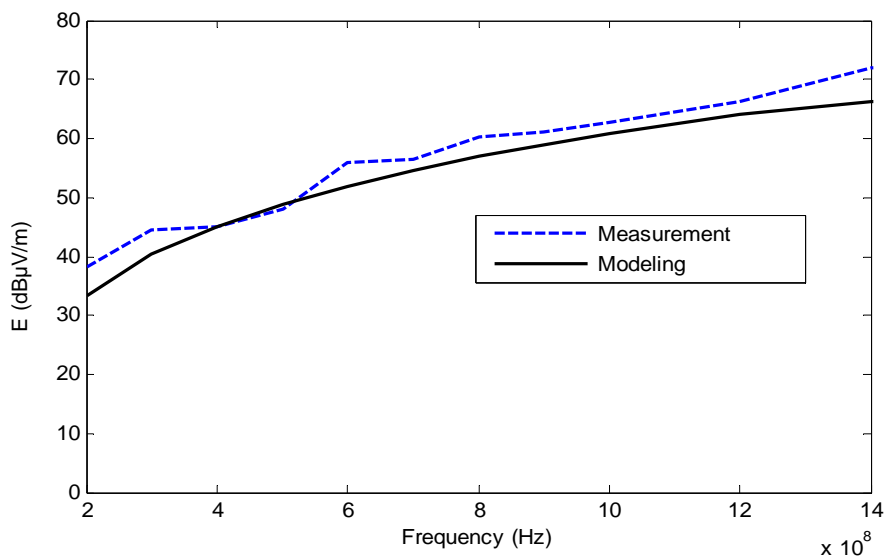
(b)

Fig. 4.5: The radiated emission from the L-shaped interconnect made on FR4.

For the L-shaped interconnect fabricated on RT5880, the dimensions are $L_x = L_y = 55$ mm, $W = 2.4$ mm. The radiated emissions from the L-shaped interconnect made on RT5880 is shown in Fig. 4.6. The radiated emission contributed by the branch along the x -axis is plotted in Fig. 4.6(a), while the radiated emission contributed by the branch along the y -axis is plotted in Fig. 4.6(b). Good agreement is observed between the modeling results and the measurement results for both branches. The difference is kept less than 5dB.



(a)



(b)

Fig. 4.6: The radiated emission from the L-shaped interconnect made on RT5880.

By comparing the modeling results and the measurement results for different interconnects on different materials, it is found that the envelopes of the two results are consistent. The magnitude difference between them is less than 5dB, which is good enough by comparing with the results in other publications using the same method [36]-[43].

4.4 Measurement of radiated emission from interconnects in digital circuits

4.4.1 Measurement of radiated emission from interconnects placed between a digital signal and a fixed load

When dealing with radiated emissions from a digital circuit, the investigation should be performed in the frequency domain, as the limits of standards are given in this domain, although the SI analysis on circuit level is usually in time domain. The peaks of emission for a digital circuit are due to the clock fundamental and higher-order harmonics. In this section, the investigated interconnects, which are the same as in the previous section, are excited by a digital clock signal as in real digital circuit condition. This signal is generated by a 200 MHz FXO-HC536R-200 oscillator with $V_{high} = 2.4$ V, $V_{low} = 0.6$ V, $t_r = t_f = 1.5$ ns. The circuit diagram is shown in Fig. 4.7.

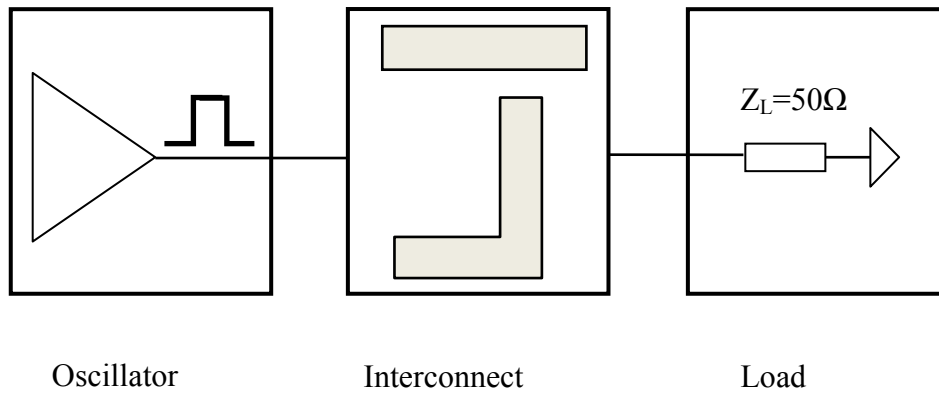
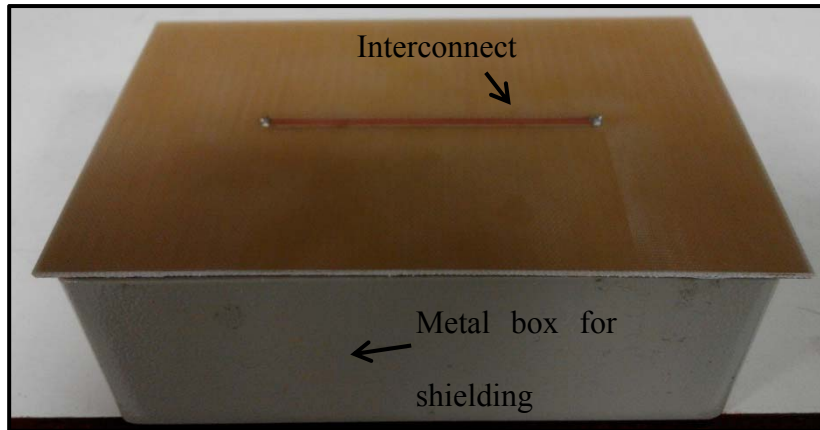
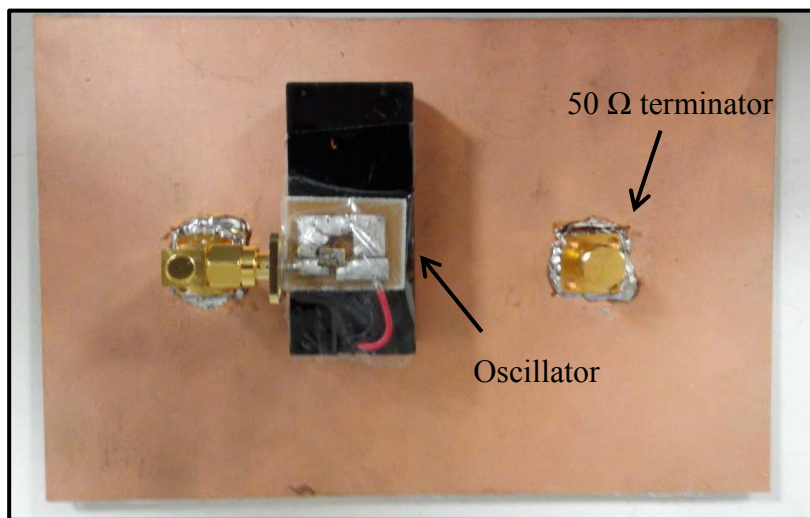


Fig. 4.7: The circuit diagram for the interconnects placed between a digital pulse input and fixed load.

In order to focus on the radiation from the interconnects only, we minimize the radiation of the oscillator by attaching it at the back side (ground side) of the PCB interconnect and using a metal box to shield it. By taking the straight interconnect made on FR4 as an example, the structure of the DUT is shown in Fig. 4.7. The external structure of the DUT is shown in Fig. 4.8(a), and the internal structure of the DUT is shown in Fig. 4.8(b). Since the peaks of emission are due to the clock fundamental and higher-order harmonics, we measure the radiation on the clock fundamental and harmonics from 200 MHz to 1.4 GHz.



(a)



(b)

Fig. 4.8: Photo of the fabricated DUT.

The radiated emission from the interconnects under this condition is modeled using the following steps:

1. Measure the output signal of the oscillator with an oscilloscope. The oscilloscope used here is the Tektronix DPO 7354C, with a frequency up to 3.5 GHz with 40 GS/s.
2. Build the circuit in a circuit simulator by exciting the interconnects with the measured pulse signal.

3. Simulate the circuit to obtain the two-port voltage and current values for the interconnects.
4. Derive the distributed current values from those two-port voltage and current values.
5. Calculate the radiated emission using the dyadic Green's function with the use of the distributed current values.

The radiated emission from the straight interconnect on FR4, which is defined in section 4.2, is plotted in Fig. 4.9. The modeling result for the radiated emission is represented by the triangle sign and the measurement result is represented by the star sign. The modeling results agree well with the measurement results. The difference between them is less than 3dB.

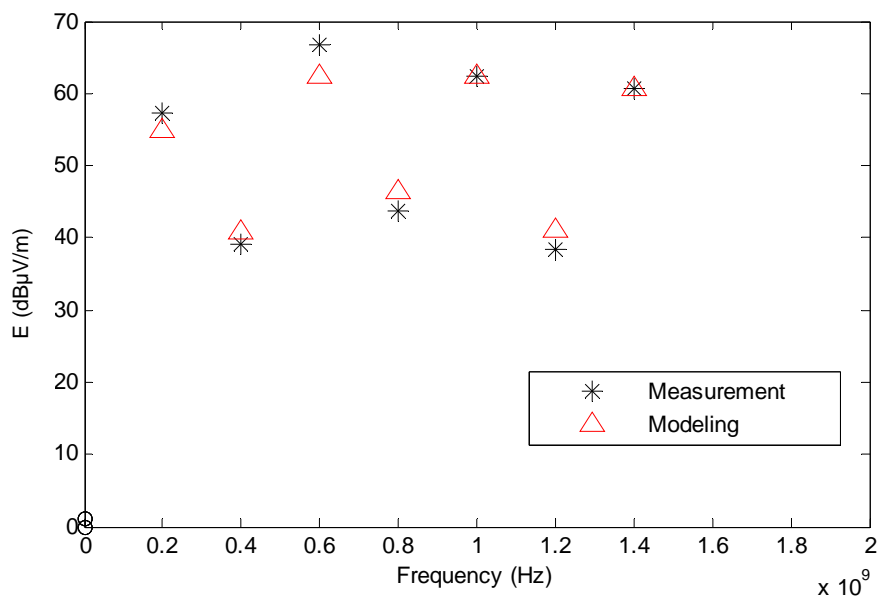


Fig. 4.9: The radiated emission from the straight interconnect on FR4.

The radiated emission from the straight interconnect on RT5880, which is defined in section 4.2, is plotted in Fig. 4.10. Good agreement

between the modeling results and the measurement results can be observed from the plot.

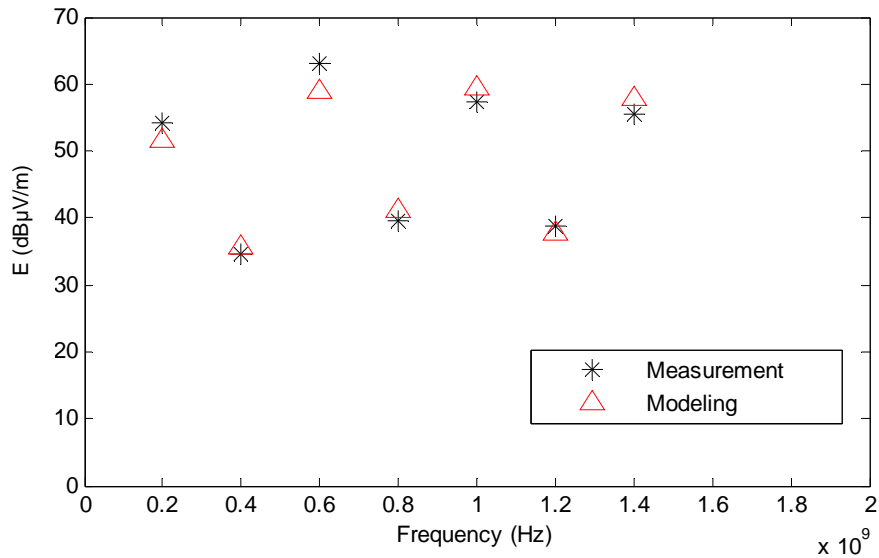
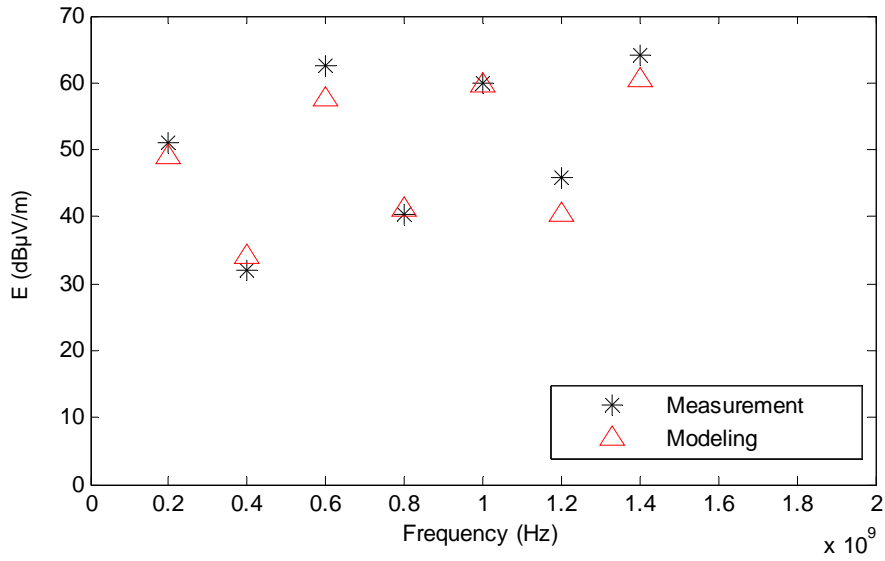
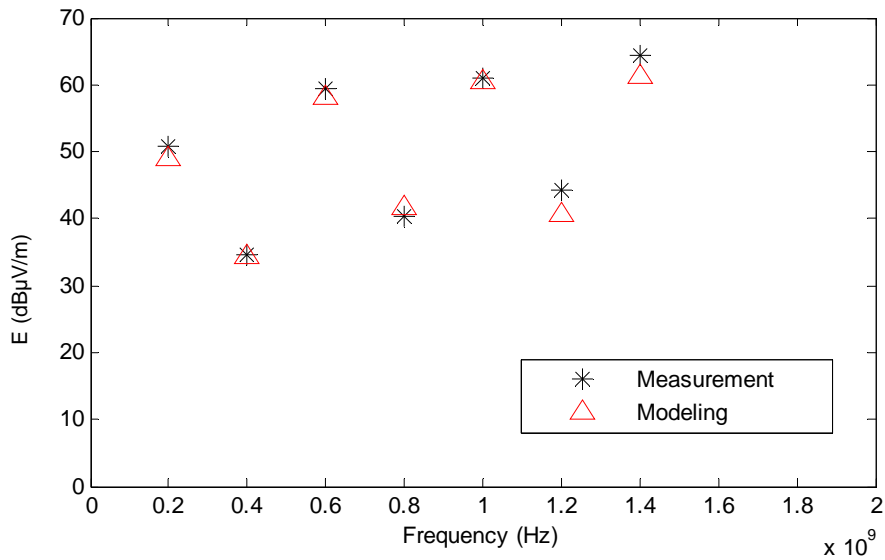


Fig. 4.10: The radiated emission from the straight interconnect on RT5880.

After investigating the radiated emission from the straight interconnects on different substrates, the investigation is extended to the L-shaped interconnects on different substrates. The radiated emission from the L-shaped interconnect on FR4, which is defined in section 4.2, is plotted in Fig. 4.11. The radiated emission contributed by the branch along the x -axis is plotted in Fig. 4.11(a), while the radiated emission contributed by the branch along the y -axis is plotted in Fig. 4.11(b). It is found that the difference between the modeling results and the measurement results is less than 2 dB, so the modeling results consist well with the measurement results.



(a)

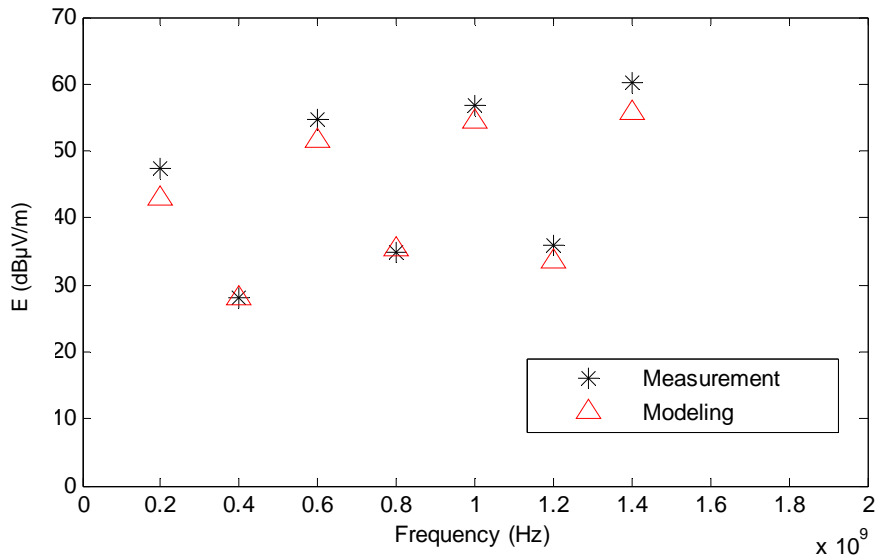


(b)

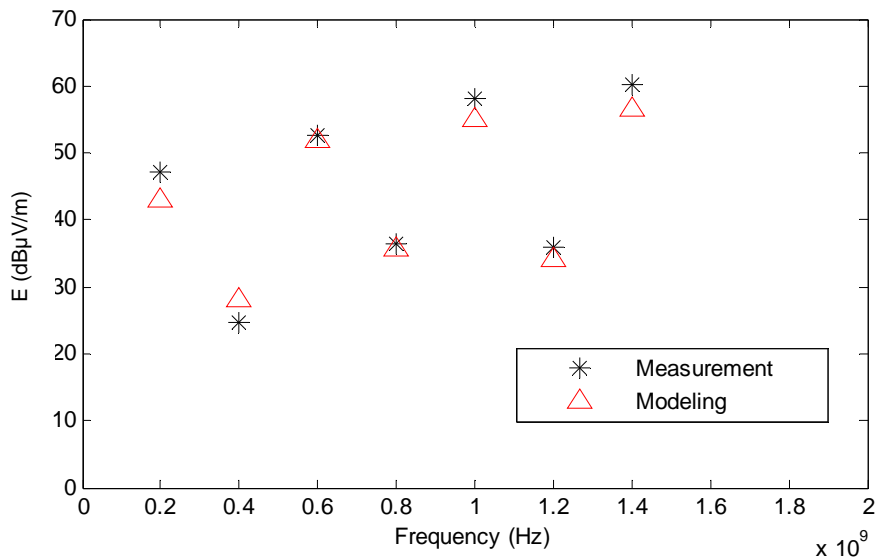
Fig. 4.11: The radiated emission for the L-shaped interconnect on FR4.

The radiated emission from the L-shaped interconnect on RT5880, which is defined in section 4.2, is plotted in Fig. 4.12. The radiated emission contributed by the branch along the x -axis is plotted in Fig. 4.12(a), while the radiated emission contributed by the branch along the y -axis is plotted in Fig.

4.12(b). The agreement between the modeling results and the measurement results is as good as in previous cases.



(a)



(b)

Fig. 4.12: The radiated emission from the L-shaped interconnect on RT5880.

From Fig. 4.9 to Fig. 4.12, we can observe that the modeling results always agree well with the measurement result at the fundamental and harmonic frequencies of the clock signal, for different substrates and the two

different interconnect shapes. Hence, the method can be used to model the radiated emission from the interconnects which are fed by a digital clock signal accurately.

4.4.2 Measurement of radiated emission from the interconnects between digital devices

In this section, the interconnects are placed between two digital devices while the driver is fed by a clock signal. The two digital devices are two identical SN74LVC125AD buffers by Taxes Instruments. The clock signal is generated by the 200 MHz FXO-HC536R-200 oscillator as introduced before. The circuit diagram is shown in Fig. 4.13.

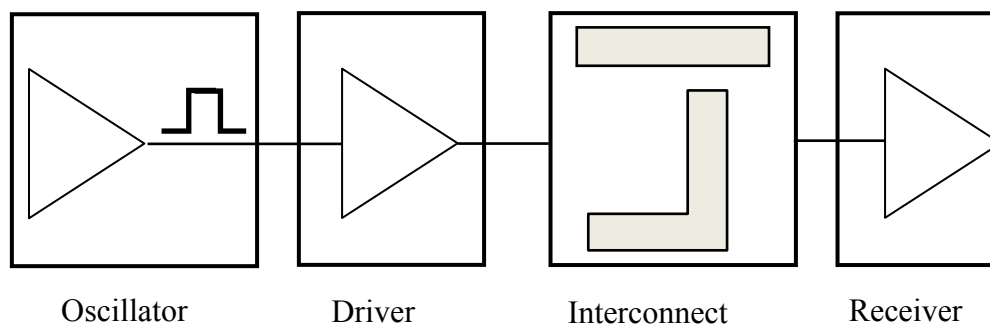
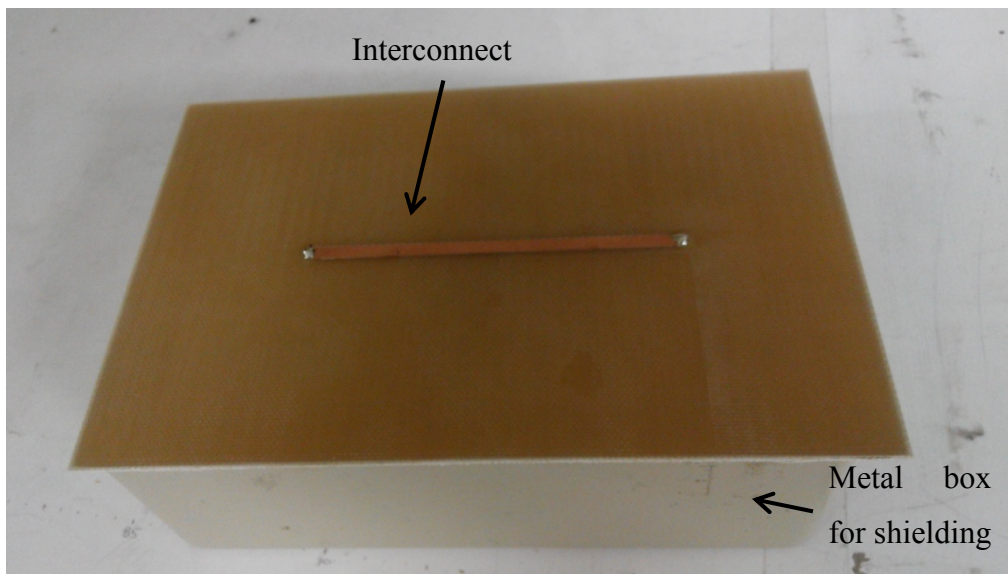


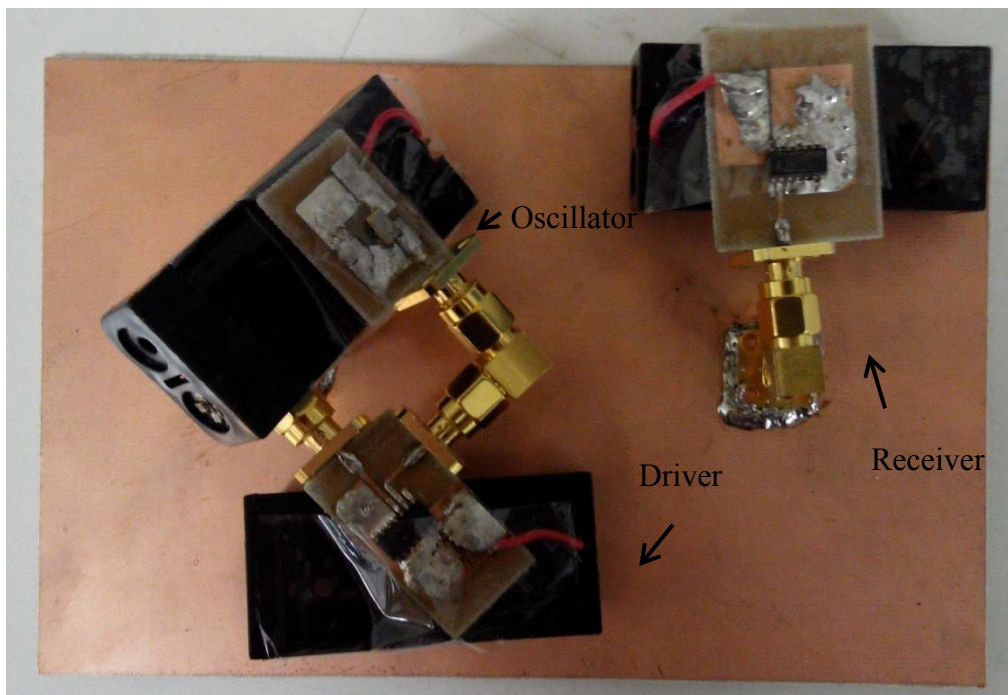
Fig. 4.13: The circuit diagram for the interconnects placed between two digital devices.

In order to focus on the radiation from the interconnects only, we minimize the radiation from the other digital devices by attaching them at the back side (ground side) of the PCB interconnect and using a metal box to shield them. By taking the straight interconnect made on FR4 as an example, the structure of the DUT is shown in Fig. 4.14. The external structure of the

DUT is shown in Fig. 4.14 (a), and the internal structure of the DUT is shown in Fig. 4.14 (b).



(a)



(b)

Fig. 4.14: Photo of the fabricated DUT.

The radiated emission from the straight interconnect on FR4, which is identical with the one defined in section 4.2, is plotted in Fig. 4.15. Based on

the modeling method described in section 4.3.1, there are two kinds of radiated emission modeling results. The first one is obtained by using the distributed current derived with the IBIS model, which is represented by the circle sign. The second one is obtained by using the distributed current derived with the SPICE model, which is represented by the rectangular sign. The radiated emission result using SPICE models is used as a benchmark for the radiated emission result using IBIS models. The measurement result is represented by the star sign. The envelopes of the three results are close. It is found that the difference between the IBIS model results and the measurement results is kept less than 5 dB, which is the same with the difference between the SPICE model results and the measurement results. The difference between the IBIS model results and the SPICE model results is less than 1 dB for most harmonics. It is noted that the IBIS model result is the same with the SPICE model result at the fundamental frequency.

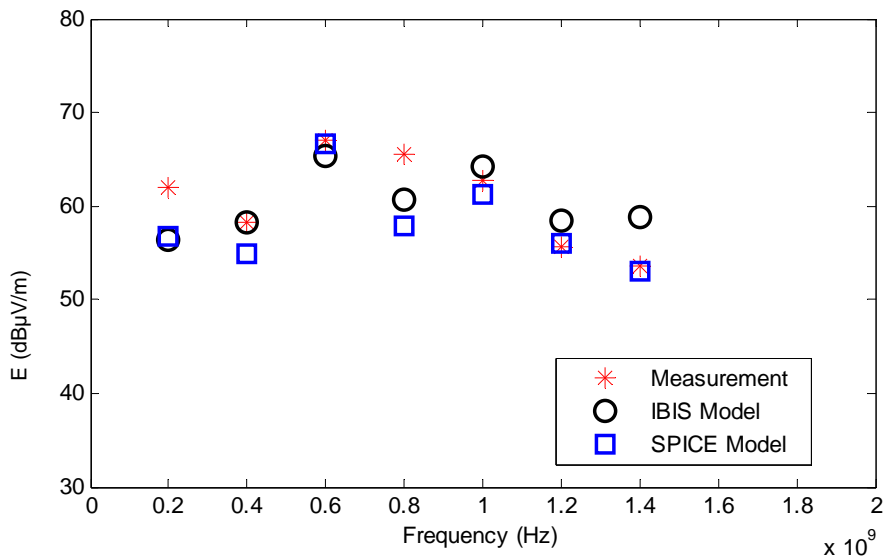


Fig. 4.15: The radiated emission from the straight interconnect on FR4 placed between two digital devices without any SI improvement techniques.

The measurement is extended to the conditions of applying four different passive SI improvement techniques on this circuit respectively. The four SI improvement techniques are: series termination technique, parallel termination technique, Thévenin termination technique and AC termination technique, which all have been introduced in section 3.5.2. The radiated emission comparison for the interconnect with series termination technique is plotted in Fig. 4.16. The envelopes of the three results are close. The difference between the IBIS model results and the measurement results is around 3 dB for the fundamental frequency and most harmonics, except the difference at 0.8 GHz is around 5 dB. The difference between the SPICE model results and the measurement results is less than 2 dB. Hence, the measurement results are closer to the SPICE model results in this case. The difference between the IBIS model results and the SPICE model results is less than 4 dB. It is noted that the IBIS model result is the same with the SPICE model result at the fundamental frequency.

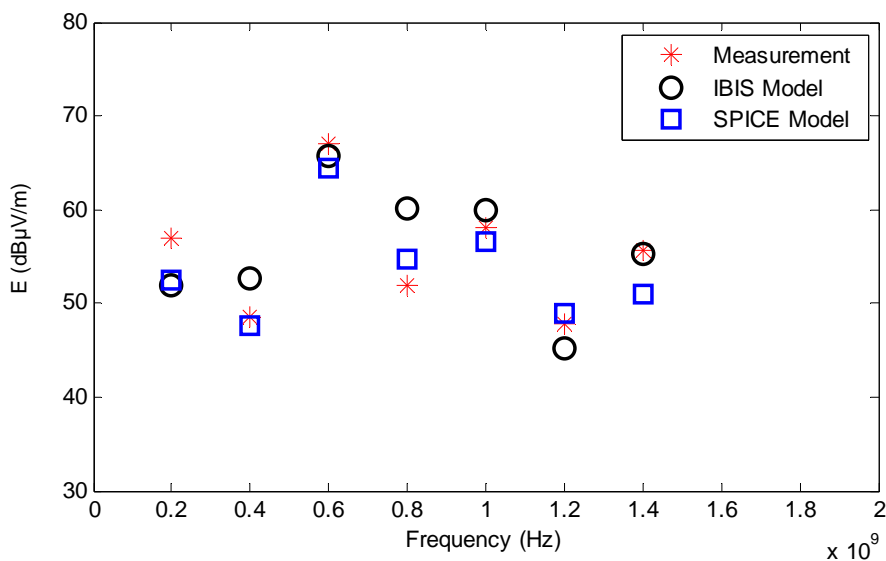


Fig. 4.16: The radiated emission from the straight interconnect on FR4 placed between two digital devices with series termination technique.

The radiated emission from the interconnect with parallel termination technique is plotted in Fig. 4.17. The envelopes of the three results are close. The difference between the IBIS model results and the measurement results is larger than before and can reach 9 dB. In contrast, the difference between the SPICE model results and the measurement results is a bit smaller, which keeps less than 8 dB. Thus, the measurement result is a bit closer to the SPICE model results. The difference between the IBIS model results and the SPICE model results is less than 3 dB, except for the radiated emission at 1 GHz, where the difference reaches 8 dB. It is noted that the IBIS model result is the same with the SPICE model result at the fundamental frequency.

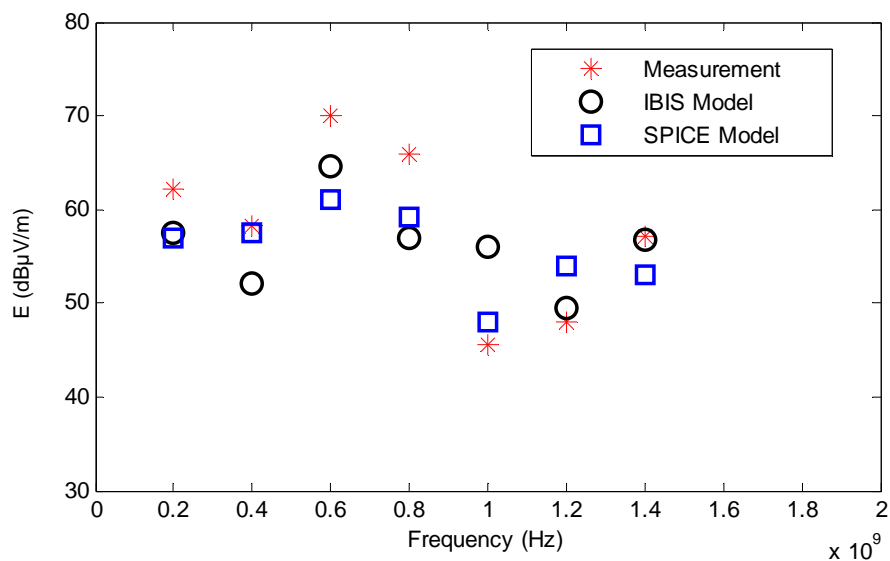


Fig. 4.17: The radiated emission from the straight interconnect on FR4 placed between two digital devices with parallel termination technique.

The radiated emission from the interconnect with Thévenin termination technique is plotted in Fig. 4.18. The envelopes of the three results are close. The difference between the IBIS model results and the SPICE model results is less than 3 dB, while the difference between the SPICE model results and the measurement results reaches 4 dB. Hence, in this case, the measurement

results are a bit closer to the IBIS model results. The difference between the IBIS model results and the measurement results is less than 3 dB. And the IBIS model result is totally the same with the SPICE model result at fundamental frequency.

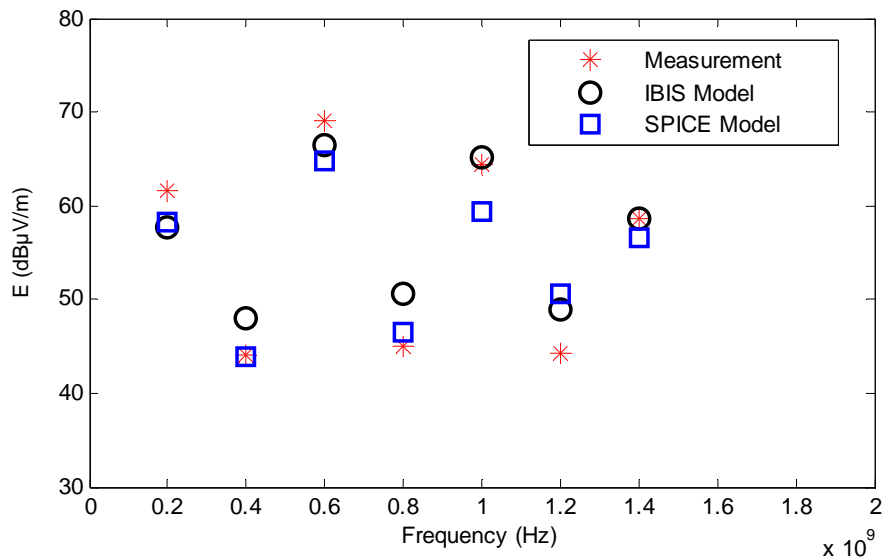


Fig. 4.18: The radiated emission from the straight interconnect on FR4 placed between two digital devices with Thévenin termination technique.

The radiated emission from the interconnect with AC termination technique is plotted in Fig. 4.19. The envelopes of the three results are close. The difference between the IBIS model results and the measurement results is kept less than 6 dB, while the difference between the SPICE model results and the measurement results is less than 5 dB. Hence the measurement results are a bit closer to the SPICE model results than the IBIS model results. The difference between the IBIS model results and the SPICE model results is less than 5 dB. The IBIS model result is still the same with the SPICE model result at fundamental frequency as in the previous cases.

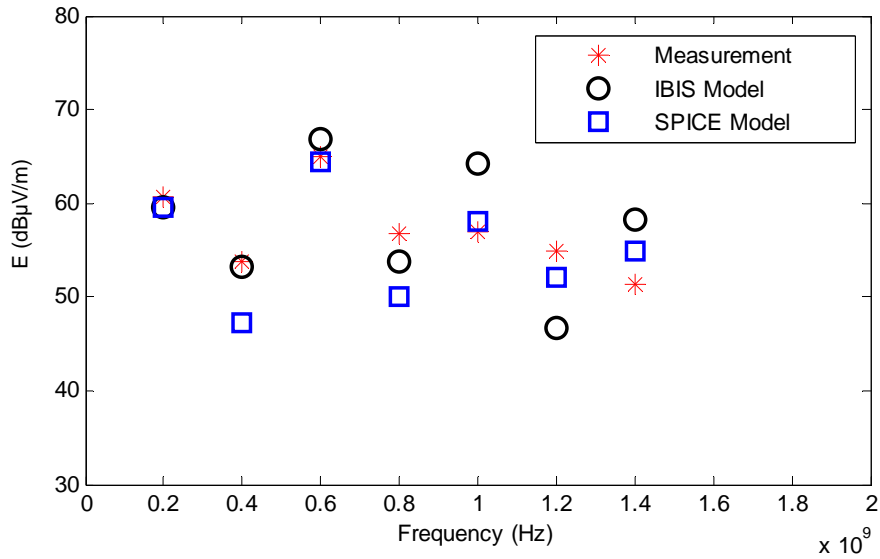


Fig. 4.19: The radiated emission from the straight interconnect on FR4 placed between two digital devices with AC termination technique.

According to the observations from Fig. 4.15 to Fig. 4.19, we can conclude that:

1. The IBIS model results always have the same envelope with the measurement results, which is similar to results in other papers [38][39]. The point to point difference is around 3-5 dB difference for most cases. The difference might be caused by the inaccuracy of those digital device models in frequency domain, as they used to provide accurate information in signal integrity analysis in time domain only. In the previous section (section 4.4.1), which is about the measurement of the radiated emission from the interconnects placed between a digital signal and a fixed load, the agreement between the measurement results and the modeling results is good over the whole frequency range for both straight and L-shaped interconnects with different substrates. Hence, the doubt about measurement set-up

problem can be eliminated. The only difference between the two measurement sections is the adoption of dynamic driver and dynamic receiver in this section. Therefore, the inaccuracy of the digital device models in the frequency domain may lead to the inaccuracy of the radiated emission analysis.

2. The IBIS model results remain close to the SPICE model results especially at the fundamental frequency as expected.
3. The measurement results are a bit closer to the SPICE model results than IBIS model results for some cases. It is because SPICE models tend to provide more information about the device circuit so the accuracy is obviously better. However adopting IBIS models can have other advantages such as reductions in simulation time and complexity reduction.

For further investigation, we measure the radiated emissions from the straight interconnect on RT5880, which is identical with the one defined in section 4.2, with and without different passive SI improvement techniques. The radiated emission from the interconnect placed between two digital devices without any SI improvement technique is plotted in Fig. 4.20. The envelopes of the three results are close. The difference between the IBIS model results and the measurement results is less than 6 dB, which the difference between the SPICE model results and the measurement results is around the same. The difference between the IBSI model results and the SPICE model results is around 2 dB for most harmonics, while at 0.8 and 1.4 GHz, the difference can reach 6 dB. The difference at the fundamental frequency is 0.

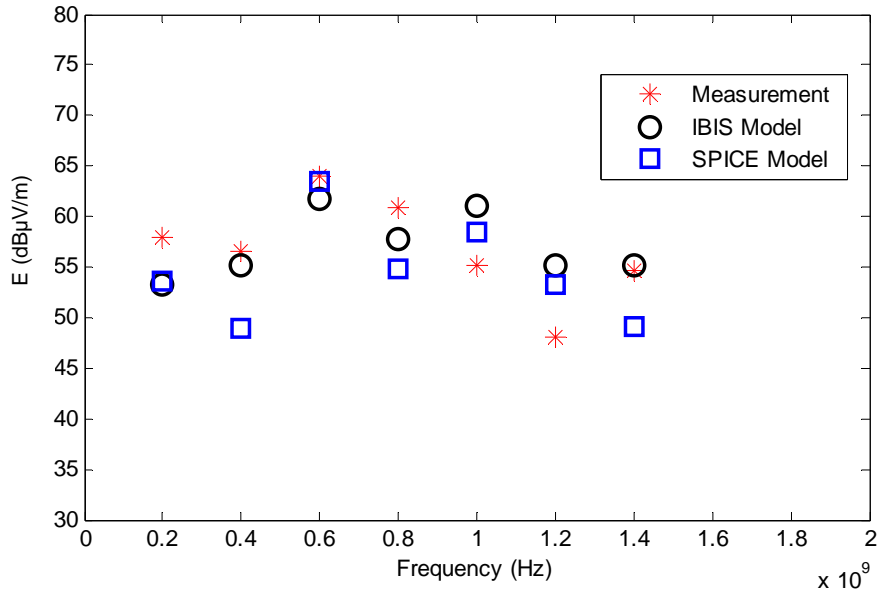


Fig. 4.20: The radiated emission from the straight interconnect on RT5880 placed between two digital devices without any SI improvement techniques.

The radiated emission comparison from the interconnect with series termination technique is plotted in Fig. 4.21. The envelopes of the three results are close. The difference between the IBIS model results and the measurement results is less than 7 dB. In contrast, the difference between the SPICE model results and the measurement results is less than 5 dB. Hence, the measurement results are closer to the SPICE model results than IBIS model results. The difference between the IBIS model results and the SPICE model results is less than 5 dB and the value at the fundamental frequency is about 0.

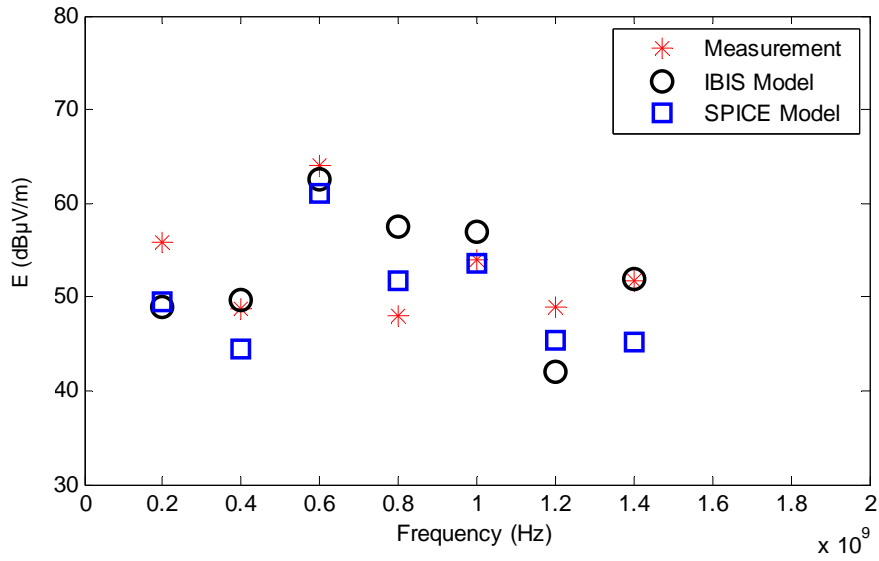


Fig. 4.21: The radiated emission from the straight interconnect on RT5880 placed between two digital devices with series termination technique.

The radiated emission from the interconnect with parallel termination technique is plotted in Fig. 4.22. The envelopes of the three results are close. The difference between the IBIS model results and the measurement results is less than 8 dB, while the difference between the SPICE model results and the measurement results is around the same value. The difference between the IBIS model results and the SPICE model results is less than 5 dB, and the value at the fundamental frequency is 0.

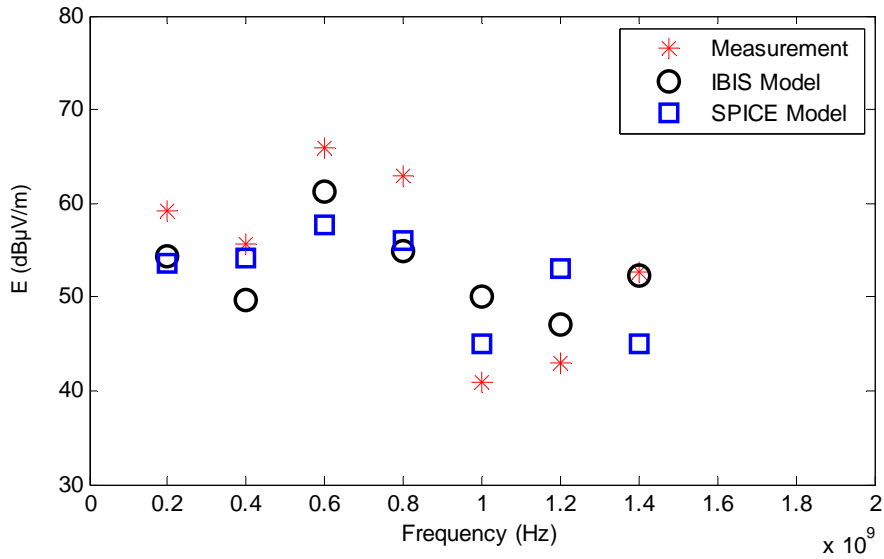


Fig. 4.22: The radiated emission comparison from the straight interconnect on RT5880 placed between two digital devices with parallel termination technique.

The radiated emission from the interconnect with Thévenin termination technique is plotted in Fig. 4.23. The envelopes of the three results are consistent. The difference between the IBIS model results and the measurement results can reach 9 dB at 0.4 and 0.8 GHz, while for other harmonic frequencies, the difference is around 1 dB. The difference between the SPICE model results and the measurement results is kept less than 4 dB. The difference between the IBIS model results and the SPICE model results is around 4 dB, while the difference value at the fundamental frequency is still 0.

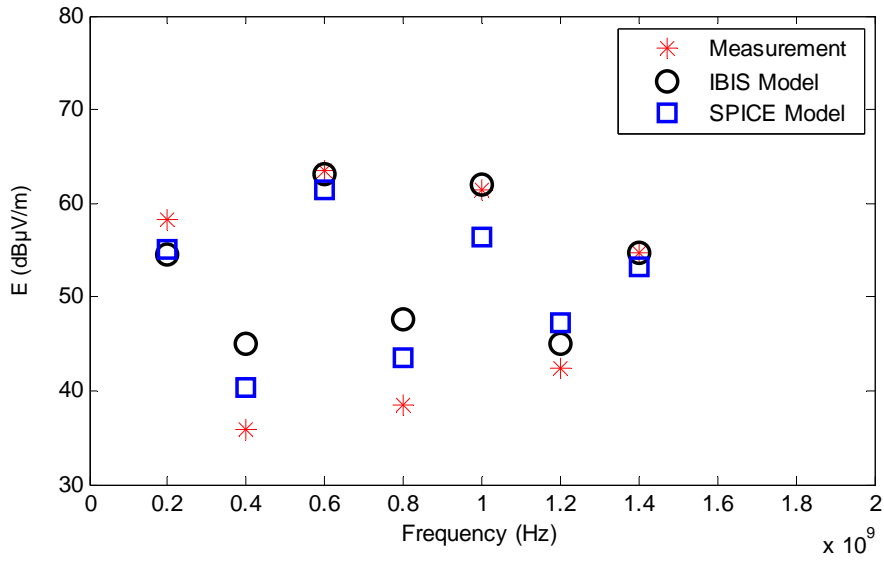


Fig. 4.23: The radiated emission from the straight interconnect on RT5880 placed between two digital devices with Thévenin termination technique.

The radiated emission from the interconnects with AC termination technique is plotted in Fig. 4.24. The envelopes of the three results agree well. The difference between the IBIS model results and the measurement results is less than 7 dB, which is the same with the difference between the SPICE model results and the measurement results. The difference between the SPICE model results and the IBIS model results is also in the same range. The IBIS model result still the same with the SPICE model result at the fundamental frequency.

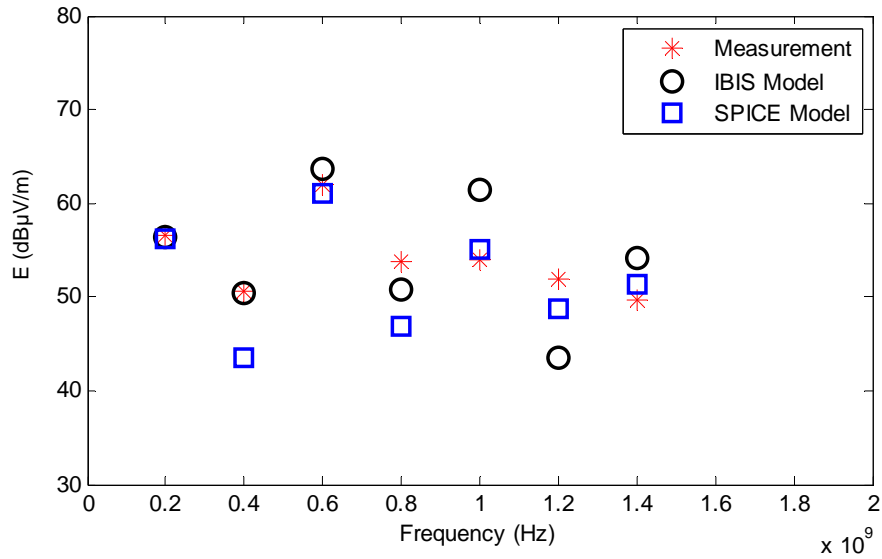
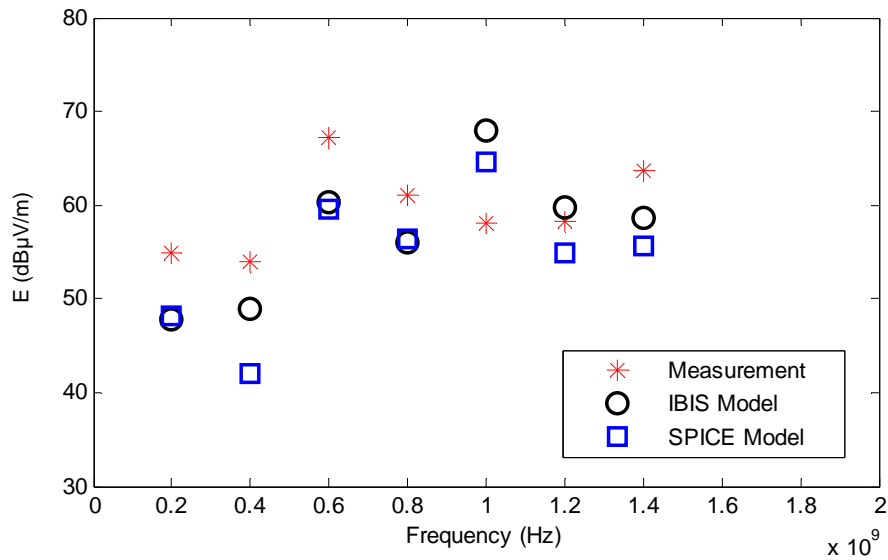


Fig. 4.24: The radiated emission from the straight interconnect on RT5880 placed between two digital devices with AC termination technique.

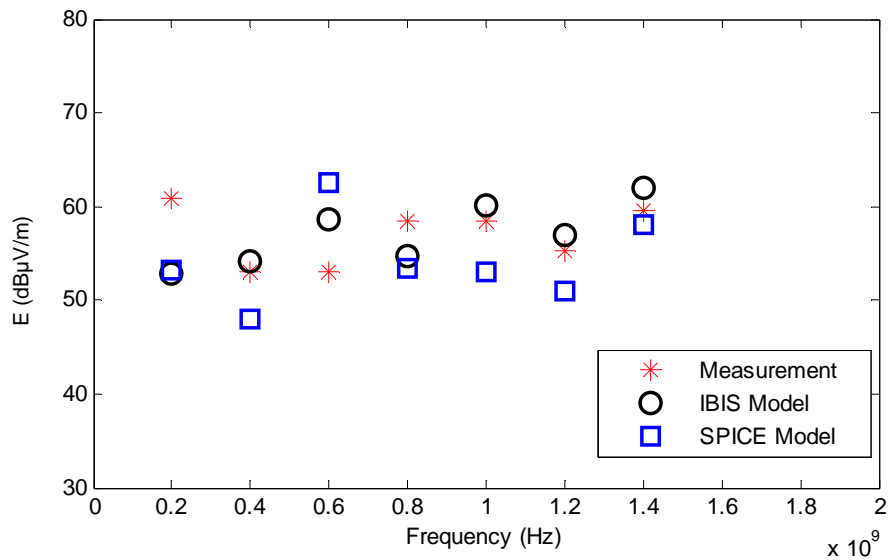
The comparisons for the straight interconnects on RT 5880 can lead to the similar conclusions as for the straight interconnects on FR4. The IBIS model results are still in the same envelope with the measurement results but have 5-8 dB differences for most cases, which is higher than the term for the interconnects on FR4. The IBIS model results always follow the SPICE model results and are nearly identical to the SPICE model results at the fundamental frequency. The measurement results just get a bit closer to the SPICE model results than IBIS model results for some cases.

Since the L-shaped interconnects are also the target in our investigation, we make the measurement for radiated emission from the L-shaped interconnect on FR4, with or without SI improvement techniques. The L-shaped interconnect is identical with the one defined in section 4.2. Fig. 4.25 represents the radiated emission from the L-shaped interconnect placed between two digital devices without any SI improvement techniques. The

radiated emission contributed by the branch along the x -axis is plotted in Fig. 4.25(a), while the radiated emission contributed by the branch along the y -axis is plotted in Fig. 4.25(b). By observing Fig. 4.25(a), it is found that at most harmonics, the difference between the IBIS model results and the measurement results is around 6 dB, which is the same with the difference between the SPICE model results and measurement results. The difference between the IBIS model results and the SPICE model results is less than 5 dB, while the value at the fundamental frequency is 0. The envelopes of the three results are close. The same observations can also be made from Fig. 4.25(b).



(a)

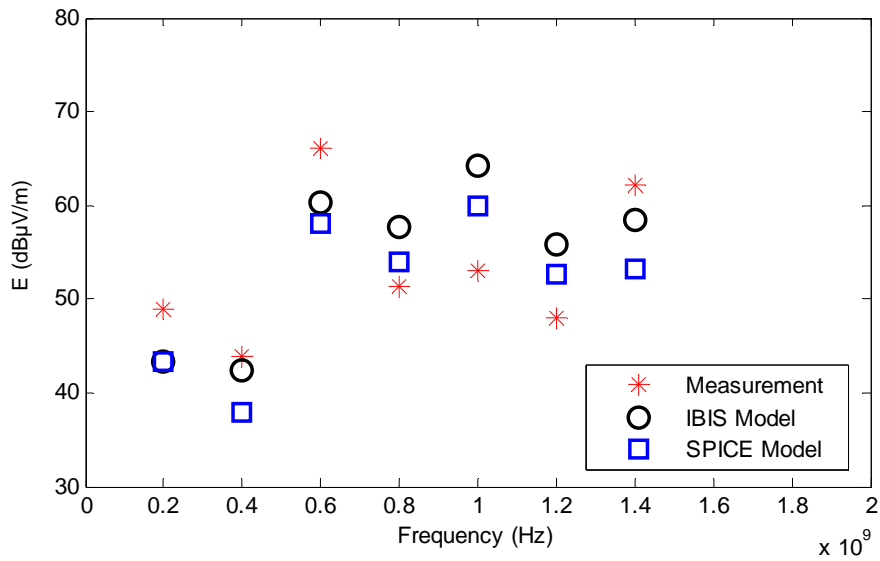


(b)

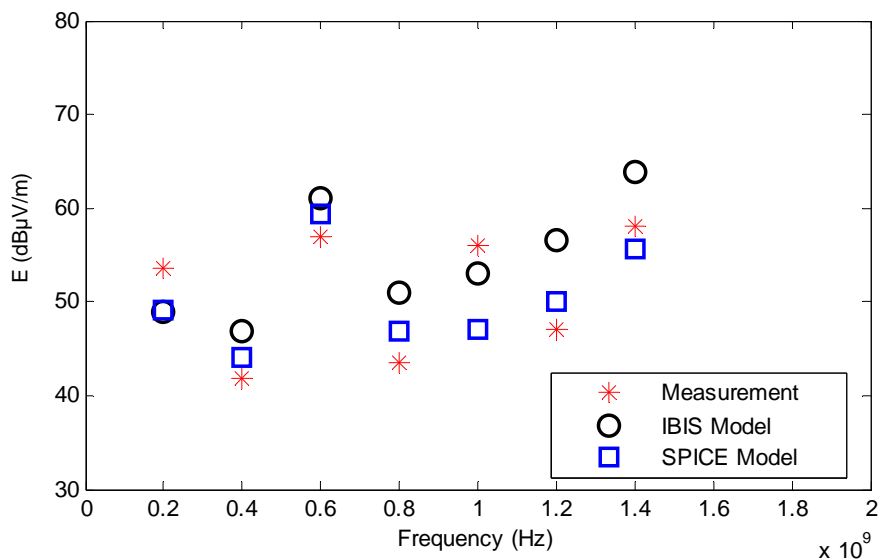
Fig. 4.25: The radiated emission from the L-shaped interconnect on FR4 placed between two digital devices without any SI improvement techniques.

The radiated emission from the L-shaped interconnect with series termination technique is plotted in Fig. 4.26. By observing Fig. 4.26(a), it is found that the envelopes of the three results are close. For most harmonics, the difference between the IBIS model results and the measurement results is kept less than 6 dB, except for an unexpected large difference at 1 GHz. And the

difference between the SPICE model results and the measurement results is around 6 dB. By comparing the IBIS model results and the SPICE model results, it is found that the difference is less than 5 dB, while the difference at the fundamental frequency is 0. For Fig. 4.26(b), similar observations can be made.



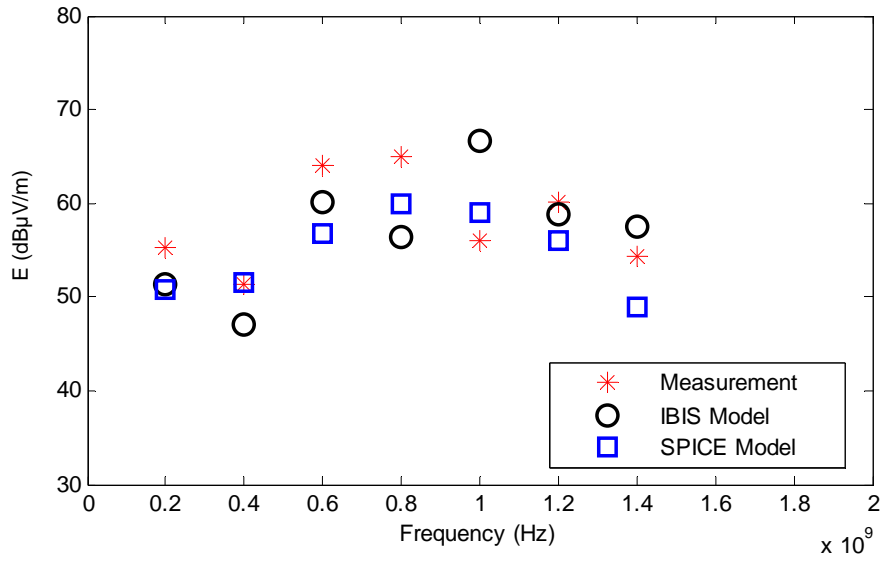
(a)



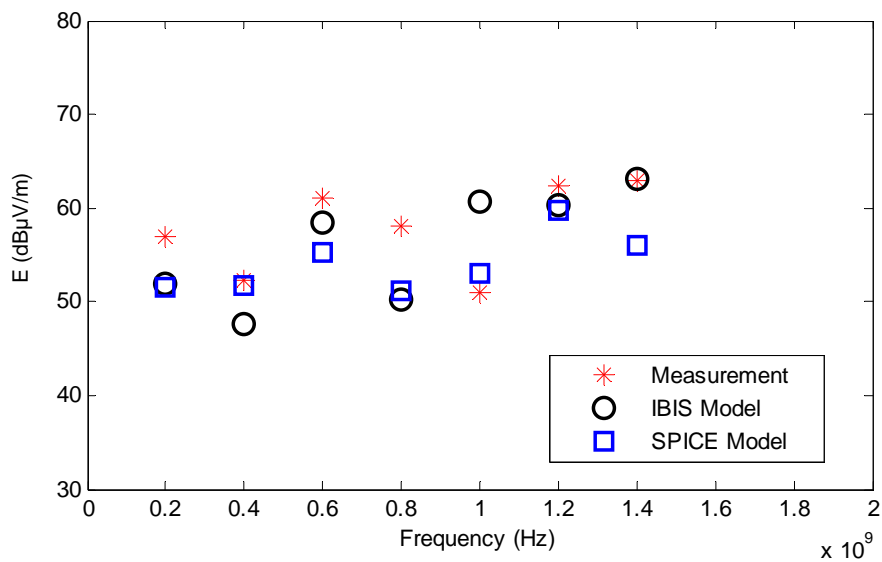
(b)

Fig. 4.26: The radiated emission from the L-shaped interconnect on FR4 placed between two digital devices with series termination technique.

The radiated emission from the L-shaped interconnect with parallel termination technique is plotted in Fig. 4.27. In Fig. 4.27(a), it is found that at most harmonics, the difference between the IBIS model results and the measurement results is less than 3 dB, except for the difference at 1 GHz. The difference between the SPICE model results and the measurement results is also around 3 dB at most harmonics, except a 9 dB difference at 1.4 GHz. The difference between the IBIS model results and the SPICE model results is around 2 dB for most harmonics. At fundamental frequency, the IBIS model result agrees very well with the SPICE model results. In general, the envelopes of the three results are close. In Fig. 4.27(b), the comparison results among the IBIS modeling results, the SPICE modeling results and the measurement results are the same as in Fig. 4.27(a)



(a)

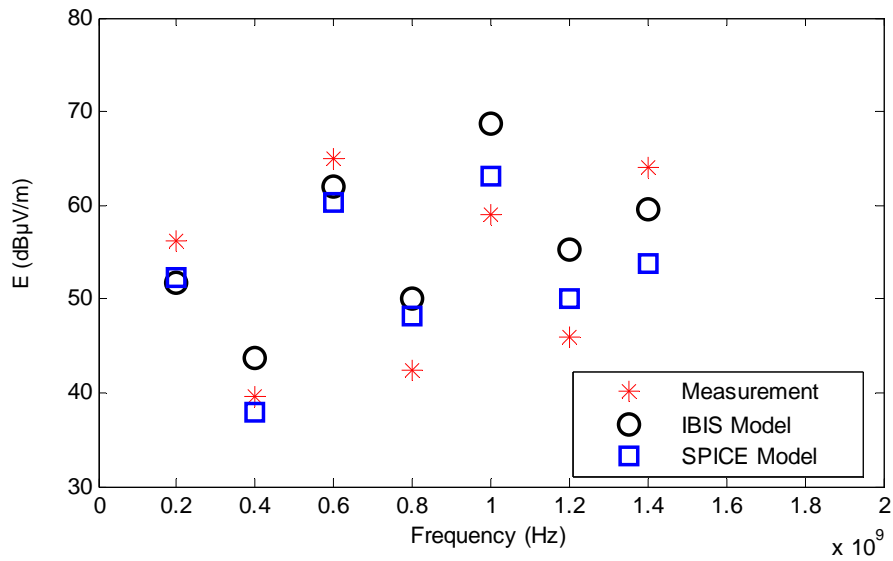


(b)

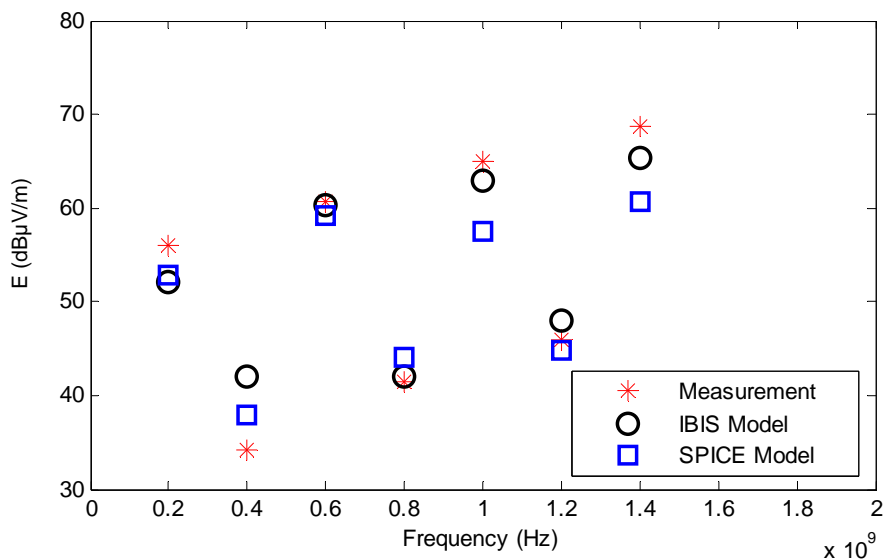
Fig. 4.27: The radiated emission from the L-shaped interconnect on FR4 placed between two digital devices with parallel termination technique.

The radiated emission from the L-shaped interconnect with Thévenin termination technique is plotted in Fig. 4.28. By observing Fig. 4.28(a), it is found that the envelopes of the three results are consistent. The difference between the IBIS model results and the measurement results is around 5 dB,

except for two large differences at 1 and 1.2 GHz, which can reach 10 dB. The difference between the SPICE model results and the measurement results is kept less than 4 dB except for a 10 dB difference at 1.4 GHz. The difference between the IBSI model results and the SPICE model results is kept less than 5 dB. In Fig. 4.28(b), the difference between the IBIS model results and the measurement results is kept less than 2 dB except for a 6 dB difference at 0.4 GHz. The difference between the SPICE model results and the measurement results is kept less than 4 dB. The IBIS model results are consistent with the SPICE model results with the difference less than 4 dB. The excellent agreement exists between the IBIS model results and the SPICE model results at the fundamental frequency for both figures.



(a)

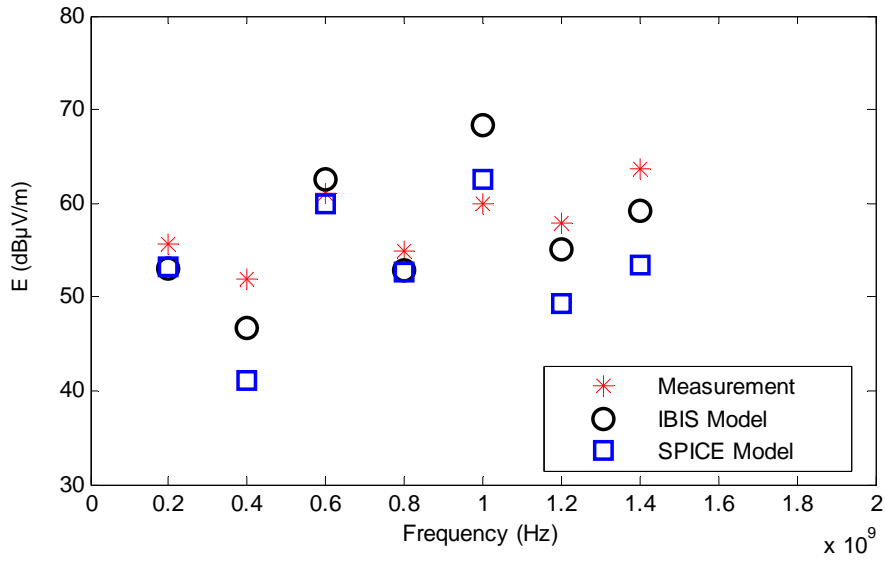


(b)

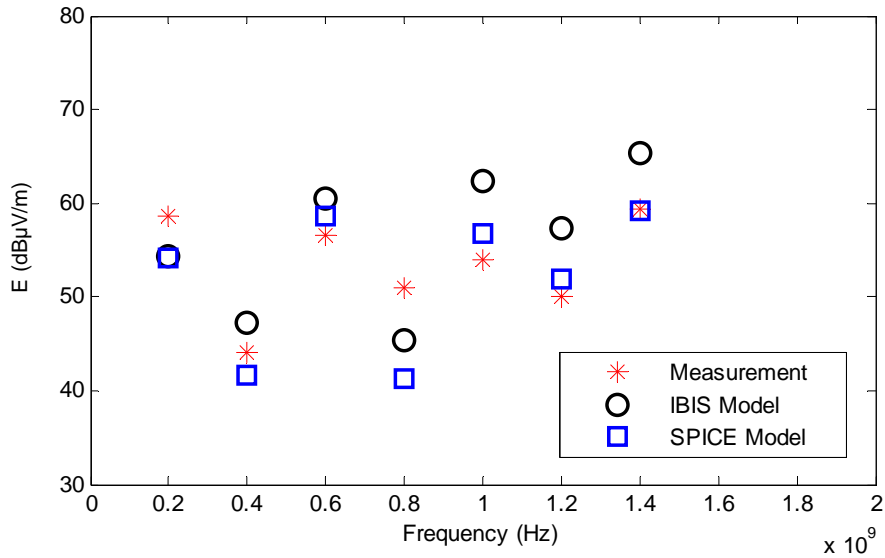
Fig. 4.28: The radiated emission from the L-shaped interconnect on FR4 placed between two digital devices with Thévenin termination technique.

The radiated emission from the L-shaped interconnect with AC termination technique is plotted in Fig. 4.29. In Fig. 4.29(a), the difference between the IBIS model results and the measurement results is less than 5 dB. The difference between the SPICE model results and the measurement results

varies a lot. At the fundamental frequency and most harmonics, the difference is less than 1 dB. However, at 0.4, 1.2 and 1.4 GHz, the difference can reach 11 dB. The difference between the IBIS model results and the SPICE model results is kept less than 5 dB. In Fig. 4.29 (b), the difference between the IBIS model results and the measurement results is less than 6 dB. The difference between the SPICE model results and the measurement results is less than 2 dB except for a 10 dB difference at 0.8 GHz. The difference between the IBIS model results and the SPICE model results is less than 6 dB. For both figures, the envelopes of the three results are close and the difference between the IBIS model results and the SPICE results at the fundamental frequency is around 0.



(a)



(b)

Fig. 4.29: The radiated emission from the L-shaped interconnect on FR4 placed between two digital devices with AC termination technique.

According to the observations above, similar conclusions can be made for the L-shaped interconnect on FR4, which are:

1. The envelope of the IBIS model results is consistent with the envelope of the measurement results. The difference for most frequency points is around 3-6 dB and can reach 10 dB for the worst case. The envelope

agreement is also achieved by other papers [38][39], but they have worst case differences up to 20 dB in the same frequency range. As discussed before, the point to point difference may be caused by the inaccuracy of digital device models in frequency domain, as they are developed to provide accurate information in signal integrity analysis in time domain only.

2. The envelope of the IBIS model results agree well with the envelope of the SPICE model results. For the fundamental frequency, the two results are nearly the same.
3. The measurement results are a bit closer to the SPICE model results than the IBIS model results. However, the accuracy improvement obtained by using SPICE models can be a trade off with the time saving and complexity reduction.

We also measure the radiated emission from the L-shaped interconnect on RT5880, which is identical with the one defined in section 4.2, placed between two digital devices without any SI improvement techniques. By comparing the three kinds of results, similar conclusions can be made as the ones for the L-shaped interconnect on FR4.

From Fig. 4.15 to Fig. 4.29, we compare the radiated emission modeling results by IBIS models with the modeling results by SPICE models and the measurement results for different substrates and different passive SI improvement techniques. The envelope of the modeling results by IBIS models agree well with the envelopes of the other two results.

4.5 Conclusions and recommendations

In this chapter, the measurement results are obtained and compare with the modeling results for the straight and L-shaped interconnects under static and dynamic source and loading conditions. The envelope agreements between the measurement results and the modeling results further confirm the accuracy of the proposed analytical method. Furthermore, it is a good method for SI designers to estimate the radiated emission from the interconnects as soon as some SI improvement techniques are applied.

The modeling method adopted in the thesis is a combination of the analytical method based on dyadic Green's function and IBIS models. By comparing with the measurement results, the point to point difference can be up to 10 dB for worst case, although the envelopes agree well. The worst case difference has been reduced from the past papers' records which can be up to 20 dB, but for further improvement, we may need to modify IBIS models, to improve the accuracy of the digital device models in frequency domain.

Chapter 5

Conclusions and recommendations

Electromagnetic radiated emission from high speed interconnects are considered to be one of the most challenging topics in the field of EMI and electronic system reliability. Thus, the radiated emission from high speed interconnects should be considered in every stage of the design cycle. As we know, several full wave commercial simulators can be used to model the radiated emission, but the time and storage requirements increase the design cost. In order to solve the problem, the modeling of the electromagnetic radiated emission from high speed interconnects through a convenient and fast method is addressed in this thesis and the modeling results are validated through measurement.

The major contributions of the thesis are:

1. Modeling the electromagnetic radiated emission from high speed interconnects in digital circuits by IBIS models on the basis of an analytical method. In the past, IBIS models are only applied in SI analysis, but this thesis introduces IBIS models to the modeling of electromagnetic radiated emission. This modeling method enables the designers to determine the radiated emission from interconnects directly during the SI analysis.
2. This thesis considers the modeling of electromagnetic radiated emission from the interconnects placed between two non-linear dynamic digital devices, i.e., a dynamic source and a dynamic load,

while in the past investigations only focus on the interconnects with dynamic load so ignore the influence of the dynamic source on the radiated emission.

3. This thesis investigates the impact of four different passive SI improvement techniques on the electromagnetic radiated emission from interconnects in digital devices. This is very useful work for digital circuit design. According to the demonstration, the digital designers can quickly estimate the change in the radiated emission when doing SI improvements in the design phase.

5.1 Modeling the electromagnetic radiated emission from high speed interconnects in digital circuits with IBIS models

The modeling of the electromagnetic radiated emission from high speed interconnects in digital circuits is based on an analytical method. In this method, the radiated emission is derived from the distributed current along the target interconnects with dyadic Green's function. The distributed current is extracted from circuit simulation results by making use of IBIS models. The extraction process is on the basis of transmission line theory and ABCD parameters.

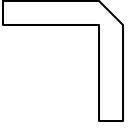
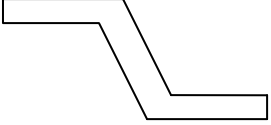
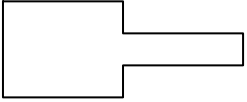
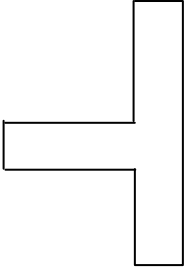
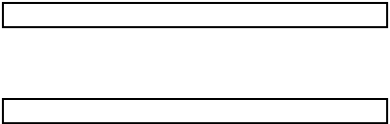
As introduced in chapter 1, the analytical method is implemented on the assumption of infinite ground plane. This assumption will limit the application of the method, i.e., for the interconnects above small ground plane, the method may not be used because of the ignorance of the finite ground

plane effect. Therefore, it is meaningful to improve the method for finite ground condition in future. The focus will be finding a simple expression to include the radiation effect of the finite ground plane to instead of the conventional full wave numerical method.

In chapter 4, it is found that the envelope of the IBIS model results is consistent with the envelope of the measurement results. However, the difference for most frequency points is around 3-6 dB and can reach 10 dB for the worst case. The envelope agreement is also achieved by other papers [38][39], while they have worst case differences up to 20 dB in the same frequency range. As discussed before, the point to point difference may be caused by the inaccuracy of digital device models in frequency domain, as they are developed to provide accurate information in signal integrity analysis in time domain only. Hence, it would be better if we can find a method to improve the accuracy of the modeling method based on IBIS models. In chapter 3, we have demonstrated how to improve the IBIS model performances in SSN simulations. The crucial point is to find out what is the missing information in IBIS models under such working condition. Then we can improve the IBIS model results by compensating the missing electrical information. For improving the accuracy of the modeling method based on IBIS models, we can implement the same methodology and adding the missing information through some external circuits or macro-models.

The investigated interconnects are made of different material and in different shapes. For further studies, the interconnects with more different shapes can be investigated. The proposed interconnects are listed in Table 5.1.

Table 5.1: Proposed interconnects for further studies.

Number	Interconnect Shape	Description
1		Compensated right angle bend
2		Double bend
3		Step junction
4		T-junction
5		Coupled straight line (side couple)

5.2 The impact of different passive SI improvement techniques on the electromagnetic radiated emission from high speed interconnects in digital circuits

The impact of different passive SI improvement techniques on the electromagnetic radiated emission from high speed interconnects in digital circuits is investigated using the modeling method proposed in the thesis. The SI improvement techniques investigated here include series termination technique, parallel termination technique, Thévenin termination technique and AC termination technique. Except these four commonly used passive SI improvement techniques, there is also a common used active SI improvement technique, called Schottky-diode termination [94] technique. In this technique, the termination comprises of two Schottky diodes as shown in Fig. 5.1. Any reflection at the end of the interconnect, which causes the voltage at the input of the receiver to rise above V_{CC} , plus the forward-bias voltage of the diode, forward-biases the diode that connects to V_{CC} . The diode turns on and clamps the overshoot to V_{CC} plus the threshold voltage. Similarly, the diode connected to ground limits undershoots to its forward-bias voltage. However, the diodes absorb no energy and merely divert it to either the power or ground plane. As a result, multiple reflections occur on the interconnect. The reflections gradually subside, principally because of the loss of energy via the diodes to V_{CC} or ground and the resistive losses of the interconnect. These losses limit the amplitude of the reflections to maintain signal integrity.

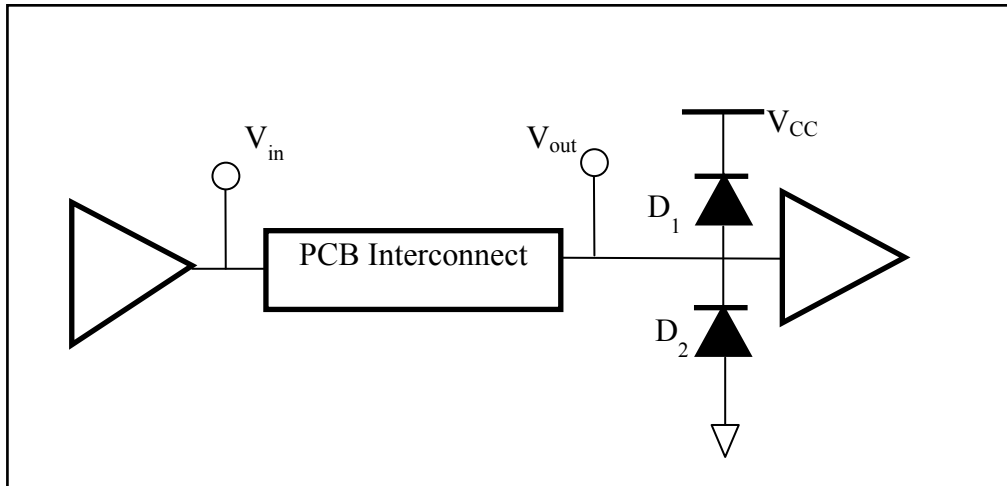


Fig 5.1: The schematic diagram for the circuit with Schottky-diode termination technique.

The impact of Schottky-diode termination technique on the electromagnetic radiated emission from high speed interconnects in digital circuits is proposed for further studies.

Bibliography

- [1] Code of Federal Regulations, Title 47(47CFR), Part 15, Subpart B, *Unintentional Radiators*. Available online: www.wireless.fcc.gov/rules.html, www.gpoaccess.gov/cfr/index.html, www.hotconsultants.com.
- [2] EN 55022:1995 (CISPR 22:1993) *Limits and Methods of Measurement of Radio Disturbance Characteristics of Information Technology Equipment*, EN 55022:1998 (CISPR 22:1997), *Information Technology Equipment-Radio Disturbance Characteristics-Limits and Methods of Measurement*. Available online: <http://europa.eu.int/comm/enterprise/newapproach/standardization/harmstds/reflist/emc.html>, and <http://www.cenelec.org>.
- [3] G. A. Jackson, “The Achievement of Electromagnetic Compatibility”, ERA report 90-0106, ERA Technology, Lcatherhead, Surrey, UK.
- [4] C. Paul, *Introduction to Electromagnetic Compatibility*, 2nded, John Wiley & Sons, Inc., US, 2006.
- [5] S. Caniggia, F. Maradei, *Signal Integrity and Radiated Emission of High-Speed Digital Systems*, 1sted, John Wiley & Sons Ltd, UK, 2008.
- [6] P. Fornberg, A. Byers, M. Picket-May, C. L. Holloway, “FDTD Modeling of Printed Circuit Board Signal Integrity and Radiation”,

- IEEE International Symposium on Electromagnetic Compatibility*, vol. 1, pp. 307-312, 2000.
- [7] M. J. Cryan, I. J. Craddock, R. V. Penty, C. J. Railton, I. H. Whilte, “Electromagnetic Compatibility Analysis of Multilayer PCBs Using a Hybrid Finite Difference Time Domain (FDTD)-Partial Element Equivalent Circuit (PEEC) Method”, *Microwave Conference*, pp.1-4, 2001.
- [8] C. J. Railton, K. M. Richardson, J. P. McGeehan and K. F. Elder, “The Prediction of Radiation Levels from Printed Circuit Boards by Means of the FDTD Method”, *International Conference on Computation in Electromagnetics*, pp. 339-343, 1991.
- [9] W. J. Buchanan, N. K. Gupta, J. M. Arnold, “Application of 3D Finite-Difference Time-Domain (FDTD) Method to Predict Radiation from a PCB with High Speed Pulse Propagation”, *Ninth International Conference on Electromagnetic Compatibility*, pp. 287-291, 1994.
- [10] A. C. Cangellaris, “Frequency-Domain Finite Element Methods for Electromagnetic Field Simulation: Fundamentals, States of the Art, and Applications to EMI/EMC Analysis”, *IEEE International Symposium on Electromagnetic Compatibility*, pp. 107-116, 1996.
- [11] R. Laroussi, G. I. Costache, “Finite-Element Method Applied to EMC Problems [PCB Environment]”, *IEEE Transactions on Electromagnetic Compatibility*, vol. 35, no. 3, May 1993.

- [12] T. H. Ooi, S. Y. Tan, and H. Li, "Study of Radiated Emissions from PCB with Narrow Ground Plane", *IEEE International Symposium on Electromagnetic Compatibility*, pp. 552-555, 1999.
- [13] H. Lee, J. Kimi, S. Ahn, J. Byun, D. Kang, C. Choi, H. Hwang, J. Kim, "Effect of Ground Guard Fence with Via and Ground Slot on Radiated Emission in Multi-layer Digital Printed", *IEEE International Symposium on Electromagnetic Compatibility*, pp. 653-656, 2001.
- [14] G. Cerri, R.D. Leo, V. M. Primiani, "A Rigorous Model for Radiated Emission Prediction in PCB Circuits", *IEEE Transactions on Electromagnetic Compatibility*, vol. 35, no. 1, pp. 102-109, 1993.
- [15] L. K. Yeung, K. L. Wu, "PEEC Modeling of Radiation Problems for Microstrip Structures", *IEEE Transactions on Antennas and Propagation*, vol. 61, no. 7, pp. 3648-3655, 2013.
- [16] L. K. Yeung, K. L. Wu, "Generalized Partial Element Equivalent Circuit (PEEC) Modeling with Radiation Effect", *IEEE Transactions on Microwave Theory and Techniques*, vol. 59, no. 10, pp. 2377-2384, 2011.
- [17] H. Heeb, A. E. Ruehli, "Three-Dimensional Interconnect Analysis Using Partial Element Equivalent Circuits", *IEEE Transactions on Circuits and Systems I: Fundamental Theory and Applications*, vol. 39, no. 11, pp. 974-982, 1992.
- [18] S. Ponnappalli, H. Heeb, "EMI Prediction Using a Full-Wave Analysis Method Based on a Surface Formulation", *Electrical Performance of Electronic Packaging*, pp. 193-195, 1992.

- [19] V. Vahrenholt, H. D. Brüns, H. Singer, “Fast EMC Analysis of Systems Consisting of PCBs and Metallic Antenna Structures by a Hybridization of PEEC and MoM”, *IEEE Transactions on Electromagnetic Compatibility*, vol. 52, no. 4, 2010.
- [20] J. Simpson, R. Goulette, G. Costache, “Radiation from Microstrip Transmission Lines”, *IEEE International Symposium on Electromagnetic Compatibility*, Seattle, WA, pp.340-343, 1988.
- [21] D. M. Sullivan, *Electromagnetic Simulation Using the FDTD Method*, John Wiley & Sons, Inc., 2000.
- [22] J. Jin, *The Finite Element Method in Electromagnetics*, John Wiley & Sons, New York, USA, 1993.
- [23] R. F. Harrington, *Field Computation by Moment Methods*, Robert E. Krieger, Malabar, FL, 1987.
- [24] J. Nitsch, F. Gronwald, G. Wollenberg, *Radiating Nonuniform Transmission-Line Systems and the Partial Element Equivalent Circuit Method*, John Wiley & Sons, UK, 2009.
- [25] J. Ekman, *Electromagnetic Modeling Using the Partial Element Equivalent Circuit Method*, Ph.D. Thesis, 2003.
- [26] K. S. Yee, “Numerical Solution of Initial Value Problems Involving Maxwell’s Equations in Isotropic Media”, *IEEE Transactions on Antennas and Propagation*, vol. 14, pp. 302-307, 1966.
- [27] M. N. O. Sadiku, *Numerical Techniques on Electromagnetics*, CRC Press, Inc. 1992.
- [28] D. K. Cheng, *Fundamentals of Engineering Electromagnetics*, Addison-Wesley Publishing Company, 1994.

- [29] S. Caniggia, L. Catello, V. Costa, G. Marano, N. O’Riordan, L. Viticci, “Controlling Radiated Emission from a Physically Large, Telecommunication System”, *IEEE Transactions on Electromagnetic Symposium on Electromagnetic Compatibility*, vol. 38, no.3, pp.290-299, 1996.
- [30] D. A. Hill, D. G. Camell, K. H. Cavcey, G. H. Koepke, “Radiated Emissions and Immunity of Microstrip Transmission Lines: Theory and Reverberation Chamber Measurements”, *IEEE Transactions on Electromagnetic Symposium on Electromagnetic Compatibility*, vol. 38, no. 2,pp. 165-171, 1996.
- [31] V, Costa, S. Caniggia, L.Catello, “On the Computation of Electromagnetic Field Components from a Transmission Line: Theory and Application”, *IEEE International Symposium on Electromagnetic Compatibility*, pp. 651-656, 1990.
- [32] R. S. Shi, A. Darcherif, J. C. Sabonnadière, “Computation of Transient Electromagnetic Fields Radiated by a Transmission Line: An Exact Model”, *IEEE Transactions on Magnetics*, vol. 31, no.4, 1995.
- [33] S. Daijavad, W. Pence, B. Rubin, H. Heeb, S. Ponnappalli, A. Ruehli, “Methodology for Evaluating Practical EMI Design Guidelines Using EM Analysis Program”, *IEEE International Symposium on Electromagnetic Compatibility*, Anaheim, CA, pp. 30-34, 1992.
- [34] S. Daijavad, J. Janak, H. Heeb, A. Ruehli and D. McBride, “A Fast Method for Computing Radiation from Printed Circuit Boards”,

- IEEE International Symposium on Electromagnetic Compatibility*, Washington, DC, pp. 300-304, 1990.
- [35] Y. S. Khee, M. Zara Mohamed Jenu, "Magnetic and Electric Field Radiation of Bent Microstrip Line Using Hertzian Dipole Method", *IEEE International RF and Microwave Conference Proceedings*, KL, Malaysia, pp. 31-35, 2008.
- [36] Y. S. Khee, M. Zara Mohamed Jenu, "Radiated Emission of Bent Microstrip Line Using Hertzian Dipole Method", *IEEE International Symposium on Electromagnetic Compatibility*, pp. 1-6, 2008.
- [37] M. Leone and H. Singer, "Efficient Computation of Radiated Fields from Finite-Size Printed Circuit Boards Including the Effect of Dielectric Layer", *IEEE International Symposium on Electromagnetic Compatibility*, Seattle, WA, pp. 85-90, 1999.
- [38] S. Caniggia, V. Costa, L. Vitucci, "Investigation of EMI on Multilayer Circuit Boards: Radiated Emission", *IEEE International Symposium on Electromagnetic Compatibility*, Santa Clara, CA, pp. 316-321, 1996.
- [39] S. Caniggia, V. Costa, L. Vitucci, "Printed Circuit Post-Layout Analysis: from Signal Integrity to Radiated Emission", *IEEE International Symposium on Electromagnetic Compatibility*, Denver, CO, pp. 975-980, 1998.
- [40] M. Leone, "Closed-Form Expressions for the Electromagnetic Radiation of Microstrip Signal Traces", *IEEE Transactions on Electromagnetic Compatibility*, vol. 49, no. 2, pp. 322-328, 2007.

- [41] B. Wong, A. Cantoni, “Modeling and Analysis of Radiated Emissions and Signal Integrity of Capacitively Loaded Printed Circuit Board Interconnections”, *IEEE Transactions on Electromagnetic Compatibility*, vol. 54, no. 5, pp. 1087-1096, 2012.
- [42] B. Wong, A. Cantoni, “Radiated Emissions and Signal Integrity of Printed Circuit Board Microstrips”, *Electromagnetic Compatibility Symposium-Melbourne (EMC Melbourne)*, pp. 1-6, 2010.
- [43] H. -C. Hsieh, C.-N. Chiu, C.-H. Wang, C. H. Chen, “A New Approach for Fast Analysis of Spurious Emissions from RF/Microwave Circuits”, *IEEE Transactions on Electromagnetic Compatibility*, vol. 51, no. 3, pp. 631-638, 2009.
- [44] N.-C. Kuo, C.-N. Chiu, H.-C. Hsieh, J.-S. Chen, “Radiation Minimization of Single-Stub Microstrip Impedance Transformers”, *IEEE Transactions on Microwave Theory and Techniques*, vol. 61, no. 3, pp. 1018-1029, 2013.
- [45] E. Rogard, B. Azanowsky and M. Ney, “Comparison of Radiation Modeling Techniques Up to 10 GHz-Application on a Microstrip PCB Trace”, *IEEE Transactions on Electromagnetic Compatibility*, vol. 52, no. 2, pp. 479-486, 2010.
- [46] J. A. Kong, *Electromagnetic Wave Theory*, New York: Wiley, 1990.
- [47] W. C. Chew, *Wave and Fields in Inhomogeneous Media*, New York: Reinhold, 1990.
- [48] J. R. Mosig, R. C. Hall, and F. E. Gardiol, “Numerical Analysis of Microstrip Patch Antennas”, *Handbook of Microstrip Antennas*, vol. 1, J. R. James and P. S. Hall, Eds. London, UK: Peregrinus, 1989.

- [49] G. D. Monteath, *Applications of the Electromagnetic Reciprocity Principle*, New York: Pergamon, 1973.
- [50] H. M. Fan, F. Schlagenhauser, “Far Field Approximation of Electrically Moderate-Sized Structures by Infinitesimal Electric and Magnetic Dipoles”, *IEEE Transactions on Electromagnetic Compatibility*, vol. 52, no. 1, pp. 82-88, 2010.
- [51] L. Beghou, B. Liu, L. Pichon, F. Costa, “Synthesis of Equivalent 3-D Models from Near Field Measurements-Application to the EMC Power Printed Circuit Boards”, *IEEE Transactions on Magnetics*, vol. 45, no. 3, pp. 1650-1653, 2009.
- [52] X. Tong, D. W. P. Thomas, A. Nothofer, P. Sewell, and C. Christopoulos, “Modeling Electromagnetic Emissions From Printed Circuit Boards in Closed Environments Using Equivalent Dipoles”, *IEEE Transactions on Electromagnetic Compatibility*, vol. 52, no. 2, pp. 462-470, 2010.
- [53] P. Petre, T. K. Sarkar, “Planar Near-Field to Far-Field Transformation Using an Array of Dipole Probes”, *IEEE Transactions on Antennas Propagation*, vol.42, no. 4, pp. 534-537, 1994.
- [54] Y. V. Gilabert, C. Arcambal, A. Louis, F. D. Daran, P. Eudeline, B. Mazari, “Modeling Magnetic Radiations of Electronic Circuits Using Near -Field Scanning Method”, *IEEE Transactions on Electromagnetic Compatibility*, vol.42, no.4, pp.391-400, 2006.
- [55] J. Regue, M. Ribo, J. Garrell, and A. Martin, “ A Genetic Algorithm Based Method for Source Identification and Far-Field Emission

- Prediction from Near-Field Measurements for PCB Characterization”, *IEEE Transactions on Electromagnetic Compatibility*, vol.43, no.4, pp.520-530, 2001.
- [56] H. Fan, F. Schlagenhauser, “Near Field-Far Field Conversion Based on Genetic Algorithm for Predicting Radiation from PCBs”, *IEEE International Symposium on Electromagnetic Compatibility*, pp. 1-6, 2007.
- [57] P. Petre, T. K. Sarkar, “Planar Near-Field to Far-Field Transformation Using an Equivalent Magnetic Current Approach”, *IEEE Transactions on Antennas Propagation*, vol.40, no. 11, pp. 1348-1356, 1992.
- [58] P. Petre, T. K. Sarkar, J. A. Kong, Ed., “Differences Between Modal Expansion and Integral Equation Methods for Planar Near-Field to Far-Field Transformation”, *Progress in Electromagnetic Research (PIER)*, vol.12, pp. 37-56, 1996.
- [59] F. Las-Heras, B. Galocha, and J. L. Besada, “Far-Field Performance of Linear Antennas Determined from Near-Field Data”, *IEEE Transactions on Antennas Propagation*, vol.50, no. 3, pp. 408-410, 2002.
- [60] Y. Alvarez, F. Las-Heras, M. R. Pino, “Reconstruction of Equivalent Currents Distribution over Arbitrary Three-Dimensional Surface Based on Integral Equation Algorithms” *IEEE Transactions on Antennas Propagation*, vol.49, no. 2, pp. 391-399, 2007.

- [61] P. Li, J. J. Li, "Source Reconstruction Method-Based Radiated Emission Characterization for PCBs", *IEEE Transactions on Electromagnetic Compatibility*, vol. 55, no. 5, pp. 933-940, 2013.
- [62] T. K. Sakar, A. Taaghool, "Near-Field to Near/Far-Field Transformation for Arbitrary Near-Field Geometry Utilizing an Equivalent Electric Current and MOM", *IEEE Transactions on Antennas Propagation*, vol. 47, no. 3, pp. 566-573, 1999.
- [63] J. L. A. Quijiano and G. Vecchi, "Improved-Accuracy Source Reconstruction on Arbitrary 3-D Surfaces", *IEEE Antenna Wireless Propagation Letter*, vol. 8, pp. 1046-1049, 2009.
- [64] J. L. A. Quijiano and G. Vecchi, "Near and Very Near-Field Accuracy in 3-D Source Reconstruction", *IEEE Antenna Wireless Propagation Letter*, vol. 9, pp. 634-637, 2010.
- [65] M. Serhir, P. Besnier, and M. Drissim, "An Accurate Equivalent Behavioral Model of Antenna Radiation Using a Mode-Matching Technique Based on Spherical Near Field Measurements", *IEEE Transactions on Antenna Propagation*, vol. 56, no. 1, pp. 48-57, 2008.
- [66] Microstrip (Patch) Antennas, available online: www.antenna-theory.com/antennas/patches/.
- [67] C. A. Balanis, *Antenna Theory: Analysis and Design*, 2nded, John Wiley & Sons, Inc., Hoboken, New Jersey, 2005.
- [68] D. M. Pozar, *Microwave Engineering*, 4thed, John Wiley & Sons, Inc., Hoboken, US, 2012.

- [69] T. Edwards, *Foundations for Microstrip Circuit Design*, 2nded, NewYork: Wiley, 1995.
- [70] Texas Instruments, Application Report, SZZA034, *TI IBIS File Creation, Validation, and Distribution Processes*, Sep. 2002.
- [71] the IBIS Open Forum, available online: <http://www.vhdl.org/ibis/>.
- [72] National Semiconductor, Application Note 1111, *An Introduction to IBIS (I/O Buffer Information Specification) Modeling*, Jun. 1998.
- [73] The IBIS Open Forum, IBIS (I/O Buffer Information Specification) Version 6.0, 2013.
- [74] The IBIS Open Forum, IBIS (I/O Buffer Information Specification) Version 3.2, 1999.
- [75] The IBIS Open Forum, *IBIS Modeling Cookbook for IBIS Version 4.0*, 2005.
- [76] National Semiconductor Corp., Interface Products Group, IBIS White Paper, *IBIS Model Process for High-Speed LVDS Interface Products*, Nov. 2002.
- [77] A. Varma, “S2IBIS Past, Present and Future”, *IBIS Summit*, Oct. 2013.
- [78] H. Shen, Z. Wang, W. Zheng, “PCB Level SI Simulation Based on IBIS Model for High-speed FPGA System”, *The Ninth International Conference on Electronic Measurement & Instruments*, 2009.
- [79] S. Mazzocchi, R. Giacometti, D. Sassaroli “Channel Analysis of High Speed Digital Module and Correlation between Simulations and Measurements”, *The 17th IEEE Workshop on Signal and Power Integrity*, 2013.

- [80] K. O. Petrosjanc, I. A. Kharitonov, “Account for Radiation Effects in Signal Integrity Analysis of PCB Digital Systems”, *The 16th Euromicro Conference on Digital System Design*, 2013.
- [81] Z. Yang, S. Huq, V. Arumugham, I. Park, “Enhancement of IBIS Modeling Capability in Simultaneous Switching Noise (SSN) and Other Power Integrity Related Simulations – Proposal, Implementation, and Validation”, *IEEE International Symposium on Electromagnetic Compatibility*, vol.2, pp. 672-677, 2005.
- [82] A. Varma, M. Steer, and P. Franzon, “Improving Behavioral IO Buffer Modeling Based on IBIS”, *IEEE Transaction on Advanced Packaging*, vol. 31, no. 4, pp. 711-721, 2008.
- [83] J. E. Schutt-Aine, P. Liu, J. Tan, A. Varma, “IBIS Simulation Using the Latency Insertion Method (LIM)”, *IEEE Transactions on Components, Packaging and Manufacturing Technology*, vol.3, no. 7, pp. 1228-1236, 2013.
- [84] Y. -S. Chang, S. K. Gupta, M. A. Breuer, “Analysis of Ground Bounce in Deep Sub-Micron Circuits”, *IEEE VLSI Test Symposium*, pp. 110-116, 1997.
- [85] R. Senthinathan, G. Tubbs, M. Schuelein, “Negative Feedback Influence on Simultaneously CMOS Outputs”, *Proceedings of IEEE Custom IC Conference*, pp. 5.4.1-5.4.5, 1988.
- [86] B. Zhou, L. Yu and J. Chu, “A Tool Independent Improvement of IBIS Simulation on SSN”, *Proceedings of the International Multi-Conference of Engineers and Computer Scientists*, vol.2, Mar. 17-19, 2010.

- [87] P. Pulici, A. Girardi, G. P. Vanalli, R. Izzi, G. Bernardi, A. G. M. Strollo, G. Campardo, “A Modified IBIS Model Aimed at Signal Integrity Analysis of Systems in Package”, *IEEE Transactions on Circuits and Systems*, vol. 55, no. 7, Aug. 2008.
- [88] W.-Y. Chang, K.-Y. See, W.-S. Soh, M. Oswal, L.-B. Wang, “High-Speed Signal Termination Analysis Using A Co-Simulation Approach”, *Proceedings of the 12th International Symposium on Integrated Circuits*, 2009.
- [89] N. Monnereau, F. Caignet, N. Nolhier, D. Trémouilles, M. Bafleur, “Behavioral-Modeling Methodology to Predict Electrostatic-Discharge Susceptibility Failures at System Level: an IBIS Improvement”, *Proceeding of the 10th International Symposium on Electromagnetic Compatibility (EMC Europe 2011)*, UK, 2011.
- [90] NXP SPICE model, available online:
<http://ics.nxp.com/support/models/SPICE/>
- [91] The IBIS Open Forum, *IBIS Version 5.0*, 2008, available online:
http://eda.org/pub/ibis/ver5.0/ver5_0.txt
- [92] The IBIS Open Forum, *Power Integrity Analysis Using IBIS*, BIRD95.6, 2005.
- [93] The IBIS Open Forum, *Gate Modulation Effect*, BIRD 98.3, 2007.
- [94] K. Ethirajan, J. Nemeč, *Termination Techniques for High-Speed Buses*, EDN 43.4, Feb 16, 1998.
- [95] D. Brooks, *Signal Integrity Issues and Printed Circuit Board Design*, New Jersey: Person Education, Inc., 2003.

- [96] B. Simonovich, *Driver's Output Impedance from IBIS*, online: <http://blog.lamsimenterprises.com/2010/12/22/drivers-output-impedance-from-ibis/>, Dec 22, 2010.
- [97] CISPR 16-2-3 (edition 2.0), *Specification for Radio Disturbance and Immunity Measuring Apparatus and Methods – Part 2-3: Methods of Measurement of Disturbances and Immunity - Radiated Disturbance Measurements*, July 2006.
- [98] N. Dijk, “Uncertainties in 3-m Radiated Emission Measurements Due to the Use of Different Types of Receive Antennas”, *IEEE Transactions on Electromagnetic Compatibility*, vol. 47, no. 1, pp. 77-85, 2005.